NOVEL NANOPOROUS COMPOSITE MATERIALS FOR LIGHT GAS ADSORPTION

by

Amanda Furtado

Dissertation

Submitted to the Faculty of the

Graduate School of Vanderbilt University

in partial fulfillment of the requirements

for the degree of

DOCTOR OF PHILOSOPHY

in

Chemical Engineering

May, 2012

Nashville, Tennessee

Approved:

M. Douglas LeVan

G. Kane Jennings

Bridget R. Rogers

Scott Guelcher

Eugene J. LeBoeuf

To Matthew,

with gratitude for your unconditional love and support.

ACKNOWLEDGEMENTS

I would first like to acknowledge my research advisor, Professor M. Douglas LeVan. His modesty and genuine interest in mentoring students has been an inspiration. His patience and attention to detail have molded me into a better researcher, and for that I will be forever grateful. I am thankful for the many opportunities he has given me and for the confidence he has had in my presentation abilities. It has been an honor to study under his guidance and to be a part of his research team.

I would also like to acknowledge the members of my Ph.D. committee, Professors Scott Guelcher, Kane Jennings, Gene LeBoeuf, and Bridget Rogers. Their critiques of my research have been extremely helpful at keeping me on track to complete my thesis. Several staff members within our department also deserve thanks, including Mary Gilleran and Rae Uson for their general assistance, and Mark Holmes for his invaluable help with my research. Rossane Delapp in the Department of Civil and Environmental Engineering has also been extremely helpful with the TGA.

The U.S. Army Edgewood Chemical and Biological Center, the Army Research Office, and the Defense Threat Reduction Agency are also graciously acknowledged for funding this research. It has been a privilege to present at annual working group meetings and DTRA conferences, and to network with other scientists and engineers at these events. I would specifically like to acknowledge Greg Peterson, Chris Karwacki, John Mahle, and Jared DeCoste for stimulating research disucssions and for general assistance with my research. Joe Rossin from Guild Associates has also been invaluable at helping me scale up the synthesis of my materials.

I wish to thank members of the LeVan research group for stimulating discussions during my time here. Specifically, I wish to thank Grant Glover for introducing me to the research and for continued assistance throughout my time at Vanderbilt. I am thankful to Yu Wang for assistance with the breakthrough apparatus and for her

general guidance during my time as a graduate student. I would also like to acknowledge Bryan Schindler, Jian Liu, Lucas Mitchell, Tim Giesy, and Dushyant Barpaga for stimulating research conversations.

Family is an important aspect of my life, and this section would be incomplete without acknowledging their contributions to my success. I am grateful to my father for sparking my early interest in science and for encouraging me in its pursuit. I am also grateful to my brother for his support throughout my life. I am thankful for the time I had with my mother. Her unwavering support and dedication helped me to develop the self-confidence necessary to achieve my dreams, and I owe much of my success to her. I wish she could see me now, even though I know that she is with me. I wish to extend a heartfelt thank you to my in-laws, Pat, George, and Mike, and to my extended family, Jimmy, Terri, Kathy, and Jimmy. Thank you all for your love and support.

Finally, I would not have accomplished this without the support and love of my husband, Matthew. No matter how far apart we were, he was always there to encourage me, to celebrate my successes with me, and to help me learn from my mistakes. He has been my motivation and my strength, and for that I am forever grateful.

TABLE OF CONTENTS

LIST OF TABLES

LIST OF FIGURES

CHAPTER I

INTRODUCTION

The ability to create breathable air by removing impurities is an integral technology in modern society. Adsorbent materials are currently used to accomplish this task; however, it is advantageous to develop next generation separations technologies to target extreme air purification.

Adsorbent materials design takes into account two distinct types of adsorption. Physical adsorption is a non-specific type of adsorption that occurs when the attractive forces between gas molecules and the adsorbent surface dominates over the repulsive forces. At ambient conditions, this occurs in pore sizes similar to the adsorbate molecular diameter.[1,2] Chemisorption results from active sites present on the adsorbent that chemically bond the adsorbate to the surface.[3]

The intent of this project is to develop next generation adsorbent materials for removing light gases from air. Applications of this project range from developing adsorbent materials for use in military and first responder protective masks to developing adsorbents for use in industrial filters. Both applications require materials that are effective against a broad range of compounds, including toxic industrial chemicals and chemical warfare agents. Light toxic gases at low concentrations are often the most difficult to target for removal because of their high volatility; thus, these types of gases will be targeted during development.

In this research, adsorbent materials are synthesized and characterized based on their ability to remove a representative basic gas, ammonia, and a representative acidic gas, sulfur dioxide. This project focuses on producing biphasic adsorbents so that each phase can be optimized for the removal of one type of light gas. In most chapters, a hexagonal ordered mesoporous silica, MCM-41, is used as the scaffold

phase for the composite materials. This ordered siliceous material has an inherent capacity for ammonia due to hydrogen bonding of ammonia with the hydroxyl groups on the silica material.[4–7]

In Chapter 2, various metal salts are impregnated into MCM-41. A statistical analysis is performed to determine the metal salt which best enhances the ammonia capacity of the siliceous support. A temperature study is also performed to determine the conditioning temperature that results in the highest ammonia capacities.

Chapter 3 also focuses solely on ammonia adsorption. In this chapter, MCM-41 is impregnated with copper nitrate and a metal organic phase is grown from the parent material. This mesoporous silica-metal organic composite (MSMO) is found to have a higher ammonia capacity than the parent MCM-41. The MSMO is also more stable than the corresponding metal organic framework material.[8]

Chapter 4 focuses on impregnating MCM-41 with a carbonaceous phase to enhance the sulfur dioxide capacity of the composite material. Two different carbonaceous phases are investigated, a furfuryl alcohol-based carbon phase and a sucrose-based phase. These carbon silica composite (CSC) materials are then impregnated with metal salts and tested for their sulfur dioxide and ammonia capacities. Both carbon phases are found to enhance the sulfur dioxide capacity of the parent silica support. However, impregnating either phase with metal salts does not enhance either the ammonia or sulfur dioxide capacities compared to the unimpregnated CSC materials.

In Chapter 5, various organoalkoxysilane molecules are grafted onto the MCM-41 siliceous support. These organoalkoxysilane molecules contain amine and carbonyl functional groups that are found to enhance the sulfur dioxide and ammonia capacities, respectively, of the composites. Grafting two molecules, one containing an amine and one containing a carbonyl group, onto the MCM-41 support produces a material with high capacity for both sulfur dioxide and ammonia.

A different support phase is investigated in Chapter 6. An organoalkoxysilane molecule containing a carbonyl group is grafted onto a zirconium hydroxide substrate. The base zirconium hydroxide has a high sulfur dioxide capacity,[9–12] and grafting with the carbonyl group enhances the ammonia capacity of the composite. A new method for analyzing these organoalkoxysilane grafted materials is also investigated; specifically, diffuse reflectance infrared spectroscopy is used in conjunction with a reaction chamber to analyze the changes in the composite after exposure to ammonia and sulfur dioxide.

Finally, Chapter 7 summarizes the major conclusions determined as a result of this research. It also makes recommendations for future work that have been identified as a result of this research.

References

[1] C. Petit, C. Karwacki, G. Peterson, T. J. Bandosz. Interactions of Ammonia with the Surface of Microporous Carbon Impregnated with Transition Metal Chlorides. *J. Phys. Chem. C*, 2007, **111**, 12705-12714.

[2] J. C. Thompson. Compressibility of metal-ammonia solutions. *Phys. Rev. A*, 1971, **4**, 802-804.

[3] R. P. H. Gasser. An Introduction to Chemisorption and Catalysis by Metals. Clarendon Press, Oxford, 1985.

[4] A. M. B. Furtado, Y. Wang, T. G. Glover, M. D. LeVan. MCM-41 impregnated with active metal sites: synthesis, characterization, and ammonia adsorption. *Microporous Mesoporous Mater.*, 2011, **142**, 730-739.

[5] B.A. Morrow, I.A. Cody, L.S.M. Lee. Infrared studies of reaction on oxide surfaces: structure of chemisorbed ammonia on silica. *J. Phys. Chem.*, 1975, **79**, 2405-2408.

[6] B.A. Morrow, I.A. Cody. Infrared studies of reaction on oxide surfaces: active-sites on dehydroxylated silica for chemisorption of ammonia and water. *J. Phys. Chem.*, 1976, **80**, 1998-2004.

[7] S. Kittaka, M. Morimura, S. Ishimaru, A. Morino, K. Ueda. Effect of confinement on the fluid properties of ammonia in mesopores of MCM-41 and SBA-15. *Langmuir*, 2009, **25**, 1718-1724.

[8] A. M. B. Furtado, J. Liu, Y. Wang, M. D. LeVan. Mesoporous silica-metal organic composite: synthesis, characterization, and ammonia adsorption. *J. Mater. Chem.*, 2011, **21**, 6698-6706.

[9] G. W. Peterson, C. J. Karwacki, W. B. Feaver, J. A. Rossin. Zirconium hydroxide as a reactive substrate for the removal of sulfur dioxide. *Ind. Eng. Chem. Res.*, 2009, **48**, 1694-1698.

[10] G. B. Han, N. Park, S. H. Yoon, T. J. Lee. Investigation of catalytic reduction of sulfur dioxide with carbon monoxide over zirconium dioxide catalyst for selective sulfur recovery. *Ind. Eng. Chem. Res.*, 2008, **47**, 1427-1434.

[11] S. N. R. Rao, E. Waddell, M. B. Mitchell, M. G. White. Selective sulfur dioxide adsorbents prepared from designed dispersions of groups IA and IIA metal oxides on alumina. *J. Cat.*, 1996, **163**, 176-185.

[12] A. R. Ramadan, N. Yacoub, S. Bahgat, J. Ragai. Surface and acidic properties of mixed titanium and zirconium sulfated oxides. *Colloids Surf. A: Physicochem. Eng. Aspects*, 2007, **302**, 36-43.

CHAPTER II

MCM-41 IMPREGNATED WITH ACTIVE METAL SITES: SYNTHESIS, CHARACTERIZATION, AND AMMONIA ADSORPTION

2.1 Introduction

Mesoporous materials with ordered pore structures and large surface areas have shown promise for use in industrial applications ranging from air to water purification. MCM-41,[1] which is a member of the M41S family of siliceous materials, is one popular example of this type of structured mesoporous material. MCM-41 has a hexagonal close-packed structure composed of unidirectional cylindrical channels arranged in a hexagonal manner.[2] This ordered mesoporous material has a high surface area and is an ideal backbone for a well characterized adsorbent.

Ammonia is widely used as an industrial chemical, yet at too high a concentration, it is also hazardous to human health.[3] When ammonia must be removed from waste streams in industrial settings, activated carbons are generally used.[4] These have a large pore size distribution that provides macropores and mesopores to enhance the transport properties throughout the adsorbents and micropores that provide capacity for physical adsorption due to their strong potential wells.[5] Siliceous materials have also been found to have an affinity for ammonia adsorption due to hydrogen bonding interactions between ammonia and hydroxyl groups on the silica surface.[6–8] Ordered mesoporous silicas such as MCM-41 are useful materials for ammonia adsorption due to their high adsorptive potential for ammonia, which is higher than that of unimpregnated carbons.[9] Ordered silicas have high adsorption potential for ammonia due to their polarity; since carbon is a nonpolar substrate, its ability to interact with polar molecules such as ammonia is limited. Similar to current activated carbon materials, ordered mesoporous materials can also be impregnated with active sites to provide

chemisorption potential within the adsorbent.[10–17] This would provide both a base structure and impregnants with affinity for ammonia adsorption.

Historically, metal salts have been impregnated within activated carbons to provide active sites for chemisorption.[18,19] Metal salts that have been studied specifically for ammonia removal include zinc chloride[20] and basic copper carbonate.[22] Sulfate containing compounds have also recently been studied for their effects on ammonia removal.[23] Transition metal ions such as copper and iron are reactive due to their unfilled 3d molecular orbitals.[24] Ammonia complexes with the reactive centers of the transition metal complexes, thereby forming weakly chemisorptive coordination compounds.[25] The incorporation of zinc reactive sites into MCM-41 for use as a catalyst has been studied extensively.[5,26] The literature in this area is unclear, however, regarding whether the ammonia complexation affinity stems from the metal cation, the salt anion, or from interactions with the entire compound.

Due to the importance of ammonia removal via coordination with metals and the relatively uncharted area of metal salt precursor optimization, the objective of this study is to identify material compositions and preparation techniques that lead to a high ammonia removal capability. To accomplish this, a designed experiment is conducted to measure the effects of metal type, anion type, metal oxidation state, sample pH, and drying temperature on the impregnated MCM-41 materials. The results are analyzed statistically to determine the most important factors yielding high ammonia capacities, and they are also related to the structural characteristics of the metal impregnated samples. After analyzing the ammonia capacities of these samples, the concentration of metal salt in the impregnated material with the highest ammonia capacity is optimized. The most promising samples are characterized via pH measurements, XRD, and N_2 adsorption isotherms.

2.2 Experimental Methods

Materials

Tetramethylammonium hydroxide pentahydrate, TMAOH,(97 %),tetramethylammonium silicate solution, TMASi, (99.99 %, 15-20 wt % in water), and sulfuric acid (95.0-98.0 %) were purchased from Sigma Aldrich. Hexadecyltrimethylammonium chloride, CTAC, (25 %) in water was purchased from Pfaltz and Bauer. A solution of ammonium hydroxide (29 wt %) in water, Cab-O-Sil M5, and anhydrous zinc chloride were purchased from Fisher Scientific. All metal salts were purchased from Fisher Scientific and were ACS grade chemicals.

MCM-41 synthesis

The base siliceous MCM-41 material with a 37 Å pore was synthesized based on the procedure outlined by Glover et al.[28] Briefly, a solution of 2.4 g of 29 wt % ammonium hydroxide and 21.2 g of 25 wt % CTAC was mixed with a solution of 3.04 g of TMAOH and 20 g of 10 wt % solution of TMASi. 4.5 g of Cab-O-Sil M5 fumed silica was added to the solution, forming a reaction gel with molar ratios SiO_2:0.2CTAC:0.4TMAOH:0.03NH_4OH:0.13TMASi:26.1H_2O. The reaction gel was stirred for 30 minutes and placed in a Teflon-lined autoclave and held at 80 °C in an oven for 24 hours. The autoclave was removed from the oven after 24 hours, cooled to room temperature, and titrated to a pH of 10.0 using concentrated sulfuric acid. It was then returned to the oven and this titration procedure was repeated every 24 hours for a total of 3 titrations. After the third titration, the reactor was returned to the oven and held at 80 °C for a final 24 hours. The product was filtered and washed with distilled water to remove the remaining surfactant and allowed to dry at room temperature for 48 hours. The calcination procedure used to burn the surfactant from the MCM-41 involved heating the as-synthesized MCM-41 in air from room temperature to 540 °C at a rate of 1 °C/min and holding the sample at 540 °C for 10 hours.

Metal impregnation

To produce the initial metal salt-impregnated MCM-41 samples, a wet impregnation[27] was performed. A predetermined weight of metal salt and 0.6 g of MCM-41 were stirred in an aqueous solution for 18 hours. Unless otherwise specified, the metal salt impregnation amount corresponded to a Si/metal atomic ratio of 5. After stirring, the aqueous solutions were evaporated in air at 120 °C for 2 hours and then half of the resulting dry, impregnated, MCM-41 was heated in air in a tube furnace from room temperature to 250 °C with a 5 °C/min increase and held at 250 °C for 2 additional hours. Thus, each metal salt impregnated material heated to two different temperatures was derived from the same batch of material. Previous work in our research group has focused on carbon silica composite materials, consequently the two conditioning temperatures were chosen to give some insight into the behavior of the metal salt impregnants at low carbonization temperatures in case these samples are used as the silica phase for future CSC materials.[28]

Three metals and four different anions were chosen for investigation in this work. The metals, which have the potential for interacting strongly with ammonia, were zinc, copper (I and II), and iron (II and III).[5,18–20,22,29–32] The anions include the sulfates, carbonates, nitrates, and chlorides of the metals. These pairs resulted in impregnating a total of 14 different metal salts into the MCM-41. Table 2.1 summarizes the samples investigated in this work, as well as the oxidation state of the metal in each material. Two batches of MCM-41 were used to make a replicate of each impregnated material at both conditioning temperatures.

Statistical analysis of data was performed using the software package JMP 8.0. The models used to describe the data represent standard least squares linear regression analyses. $P < 0.05$ was considered statistically significant. In all models, ammonia capacity was set as the dependent variable and the cations and anions were set as individual independent variables. Based on experimental data, linear combinations of

Table 2.1: Metal salts used for impregnation and oxidation state of the metals.

	Metal Ion				
Anion	Zn^{+2}	Cu^{+1}	Cu^{+2}	Fe^{+2}	Fe^{+3}
Cl^{-1}	√	√	√	√	√
NO_3^{-1}	√	-	√	-	√
SO_4^{-2}	√	-	√	√	√
CO_3^{-2}	√	-	√	-	-

each cation and anion were used to calculate coefficients for each independent variable within the model. The result is a predictive model equation that can be used to define the importance of each anion and cation at enhancing ammonia capacity.

Drying procedure

An initial study was performed to determine how the conditioning temperature of the metal salt impregnated materials affected the ammonia capacity. Five conditioning methods were tested on $ZnSO_4$-impregnated MCM-41 with a Si/Zn atomic ratio of 5. The conditioning methods were (1) drying under vacuum at room temperature, (2) heating in a convection oven at 60 °C until dry, (3) heating in a convection oven at 120 °C for 2 hours, (4) initial heating at 120 °C for 2 hours and additional heating using a tubular furnace at 250 °C for 2 hours, and (5) initial heating at 120 °C for 2 hours and additional heating using a tubular furnace at 540 °C for 10 hours. The latter conditioning method mirrors the calcination procedure of the parent MCM-41 material. In this case, the impregnated $ZnSO_4$ will experience thermal conditions that are the same as during MCM-41 synthesis; consequently, this heating step mimics the thermal decomposition of the metal salt that would occur if it were impregnated into the MCM-41 reaction gel during synthesis.

Materials characterization

Nitrogen isotherms

Adsorption isotherms were measured at -196 °C using a Micromeritics ASAP 2020 with UHP nitrogen as the analysis gas. Prior to measurement, approximately 0.1 g of each sample was degassed for 8 hours, with heating to 120 °C and vacuuming to 10 μbar. Density functional theory (DFT) provided in the ASAP 2020 software was used to calculate the pore size distribution.

X-ray diffraction

XRD was used to confirm the long range structure of the MCM-41 and to confirm that the metal-impregnated samples also maintained the native MCM-41 structure. The profiles were measured using a Scintag X1h/h automated powder diffractometer with Cu target, a Peltier-cooled solid-state detector, a zero background Si(5 1 0) support, and with a copper X-ray tube as the radiation source.

pH

The surface pH of the metal salt impregnated samples was measured using a Hanna Instruments 8242 pH meter with a gel-filled electrode. Determining the solution pH is useful to indicate the overall acidity of the sample once dry; higher sample acidity should correlate to higher ammonia capacity due to acid-base reactions during adsorption.[21] The pH was tested from a stirred solution of 0.1 g of the metal salt impregnated sample and 10 mL of distilled water. The pH of four initial samples was measured after 1, 2, 3, 4, 6, and 18 hours of stirring. As these exhibited minimal difference after 4 hours, the pH of the remaining samples was measured after 4 and 18 hours of equilibration.

X-ray photoelectron spectroscopy

XPS was performed with a PHI Versaprobe XPS Microprobe analysis system manufactured by Physical Electronics, Inc. The apparatus was equipped with a monochromatic Al K(α) X-ray source (E=1486.6 eV). Survey spectra were collected over binding

energies ranging from 1300 to 100 eV using a 1 eV energy step, 20 ms/step, with 10 cycles and 1 repeat/cycle. High resolution sulfur spectra collected over binding energies ranging from 175 to 160 eV using a 0.1 eV energy step, 50 ms/step, with 10 cycles and 3 repeats/cycle. Surface neutralization was accomplished using 1.1 eV electron neutralization and 10 eV argon ion neutralization. All spectra were analyzed using a take-off angle of 45°. The pass energy was set to 58.7 eV for determination of atomic ratios and binding energies were referenced to the silicon 2p peak. Deconvolution of peaks was accomplished using 70 % Gaussian-30 % Lorenzian curves with a linear background. All samples were analyzed twice; once with no additional treatment and once after being crushed to a fine powder using a mortar and pestle to expose the inner surface of MCM-41. Since the XPS yields information on the top 30-50 Å of the sample, the two analysis types allow for determination of the bulk amount of metal salt throughout the sample, as well as determination of the amount of metal salt clustered at the surface of the MCM-41 after impregnation.

Ammonia Adsorption

Equilibrium capacities for room temperature ammonia adsorption were measured for all samples using a breakthrough apparatus, a schematic of which is shown in Figure 2.1. The concentration of ammonia fed to the adsorbent bed was kept constant at 1133 mg/m^3 (1500 ppm$_v$) in helium. The capacity of the adsorbent material, n (mol ammonia/kg adsorbent), was calculated from

$$n = \frac{F}{m}\int_0^\infty (C_0 - C)dt \tag{2.1}$$

where C_0 is the feed concentration in units of mol/m^3, and C is the effluent concentration at time t. F, the volumetric flow rate of gas through the adsorbent bed, was adjusted from 10 to 50 sccm to give a breakthrough time of approximately one hour. The mass of the sample, m, was held constant at approximately 10 mg. The sample was housed in a small cylindrical adsorbent bed. The ammonia capacity calculated

using the breakthrough apparatus has a standard deviation on the order of 3%.

2.3 Results and Discussion

Materials characterization

Nitrogen isotherms

Two batches of parent MCM-41 used as the base material for impregnations were characterized using nitrogen isotherms. Figure 2.2 depicts the nitrogen adsorption isotherm at -196 °C for one batch. The isotherm is typical of a mesoporous MCM-41 material and is Type IV based on the IUPAC classification scheme. The isotherms exhibit an inflection point at relative pressure, P/P_0, of 0.3, which is characteristic of capillary condensation in the mesopores. Hysteresis due to capillary condensation is also evident in the desorption branch of the isotherm. Table 2.2 summarizes the physical properties gleaned from the nitrogen adsorption isotherm for both batches. The average pore size of the MCM-41 material was found to be similar for both batches when analyzed using DFT.

Table 2.2: Physical properties of the parent MCM-41 as derived from nitrogen adsorption isotherms.

Property	MCM-41 batch 1	MCM-41 batch 2
S_{BET}	930 m^2/g	916 m^2/g
V_{pore}	1.27 cm^3/g	1.20 cm^3/g
d_{DFT}	34.0 Å	37.9 Å

The three impregnated materials with the highest average ammonia capacities, MCM-41 impregnated with $Cu(NO_3)_2$ at 120 °C, $ZnCl_2$ at 250 °C, and $Zn(NO_3)_2$ at 120 °C, were isolated and analyzed in more detail. Table 2.3 summarizes the ammonia capacities and material characteristics derived from the nitrogen isotherms for these samples.

The addition of metal salts within the MCM-41 resulted in approximately

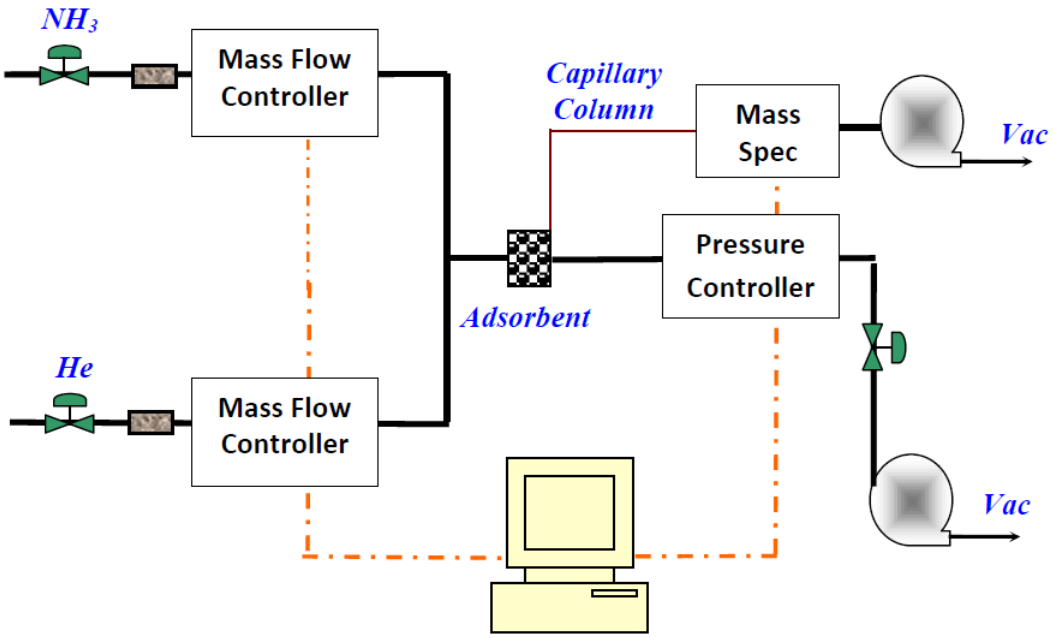

Figure 2.1 Schematic of breakthrough apparatus used to determine ammonia capacities.

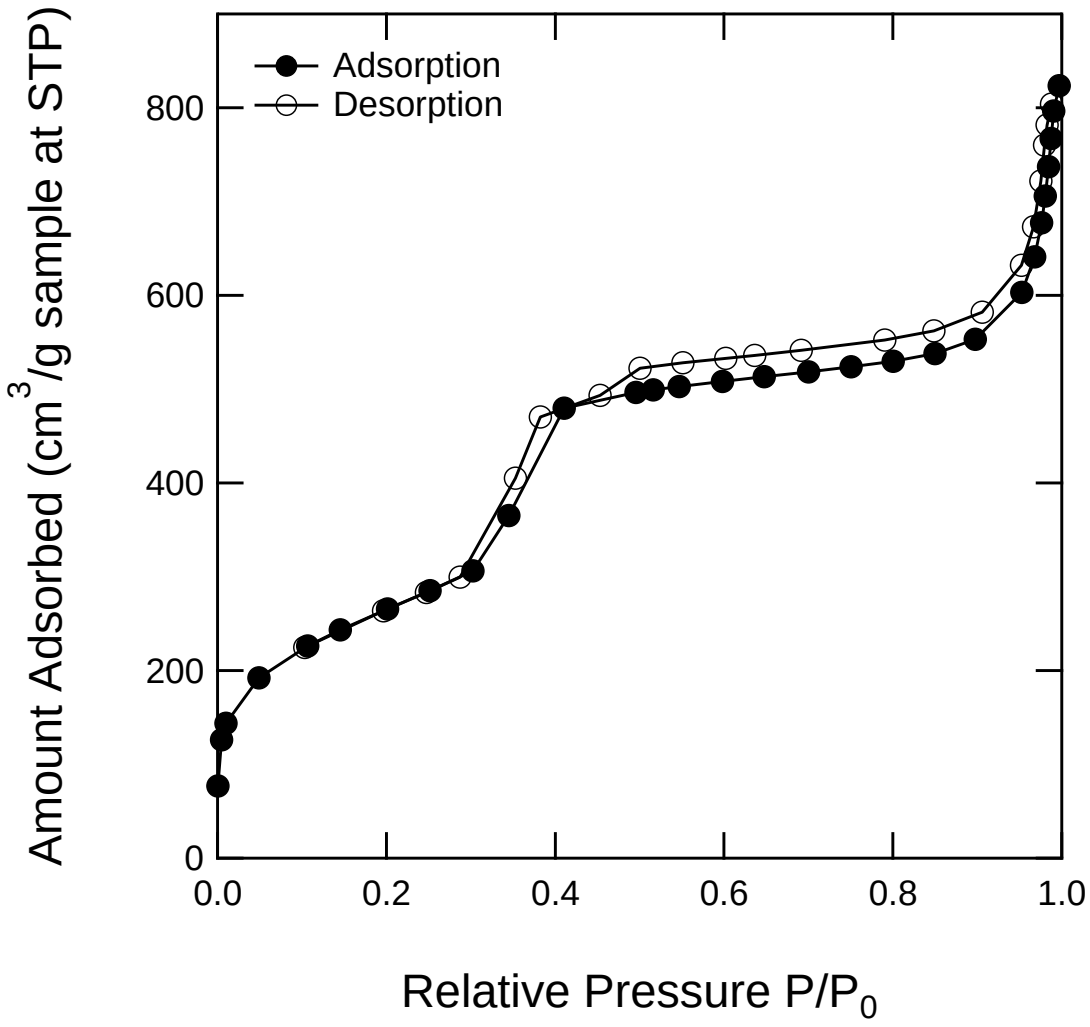

Figure 2.2 Nitrogen adsorption isotherm for the parent MCM-41 material

Table 2.3: Physical properties of the three most promising impregnated materials. Ammonia capacities measured using 1133 mg/m^3 ammonia in helium. All samples impregnated with a silicon to metal atomic ratio of 5.

Sample	Avg NH_3 Capacity (mol/kg)	S_{BET} (m^2/g)	V_{pore} (cm^3/g)	d_{DFT} (Å)
$Cu(NO_3)_2$-MCM-41 at 120 °C	6.85	614	0.80	30, 12
$ZnCl_2$-MCM-41 at 250 °C	6.70	400	0.49	31, 13
$Zn(NO_3)_2$-MCM-41 at 120 °C	6.60	568	0.76	32, 13

a 40% decrease in the calculated BET surface area for the impregnated samples compared to the parent material. According to the DFT analysis performed using the software included with the Micromeritics ASAP 2020 porosimeter, the average pore size of the samples decreased compared to the parent material. The decreases in surface area and pore size result from the metal salts lining the interior walls of the MCM-41[13] due to metal salt uptake into the MCM-41 pores.

Four $ZnSO_4$ impregnated MCM-41 samples were adjusted for pH using sulfuric acid to monitor the effects of pH on ammonia capacity within a sample. Zinc sulfate was chosen as the impregnant because it was previously studied in-depth at different conditioning temperatures. Nitrogen isotherms on these samples showed a decrease in surface area and pore volume after modification with sulfuric acid.

X-ray diffraction

In addition to the N_2 adsorption isotherm, X-ray diffraction was also used to characterize the parent MCM-41 material and is shown in Figure 2.3. A high degree of structural ordering is indicated by the four discrete sharp peaks in the low angle spectrum.[33]

As shown in Figure 2.4, X-ray diffraction analyses of the three metal-impregnated samples with the highest ammonia capacities confirmed that the zinc and copper salt impregnated materials maintained the long range MCM-41 order. This is indicated by the intense reflection between the low angles of 2.0 and 2.8° 2θ, which corresponds to the (1 0 0) basal plane. The materials also exhibit two peaks between 4.0 and 5.0° 2θ, which correspond to the distance between planes (1 1 0) and (2 0 0).

XRD was also used to characterize the structural change of four $ZnSO_4$ impregnated MCM-41 samples that were pH adjusted with sulfuric acid to monitor the effects of pH on ammonia capacity within a sample. Figure 2.5 depicts the XRD spectra for the four samples, and shows a decrease in the ordering of the MCM-41

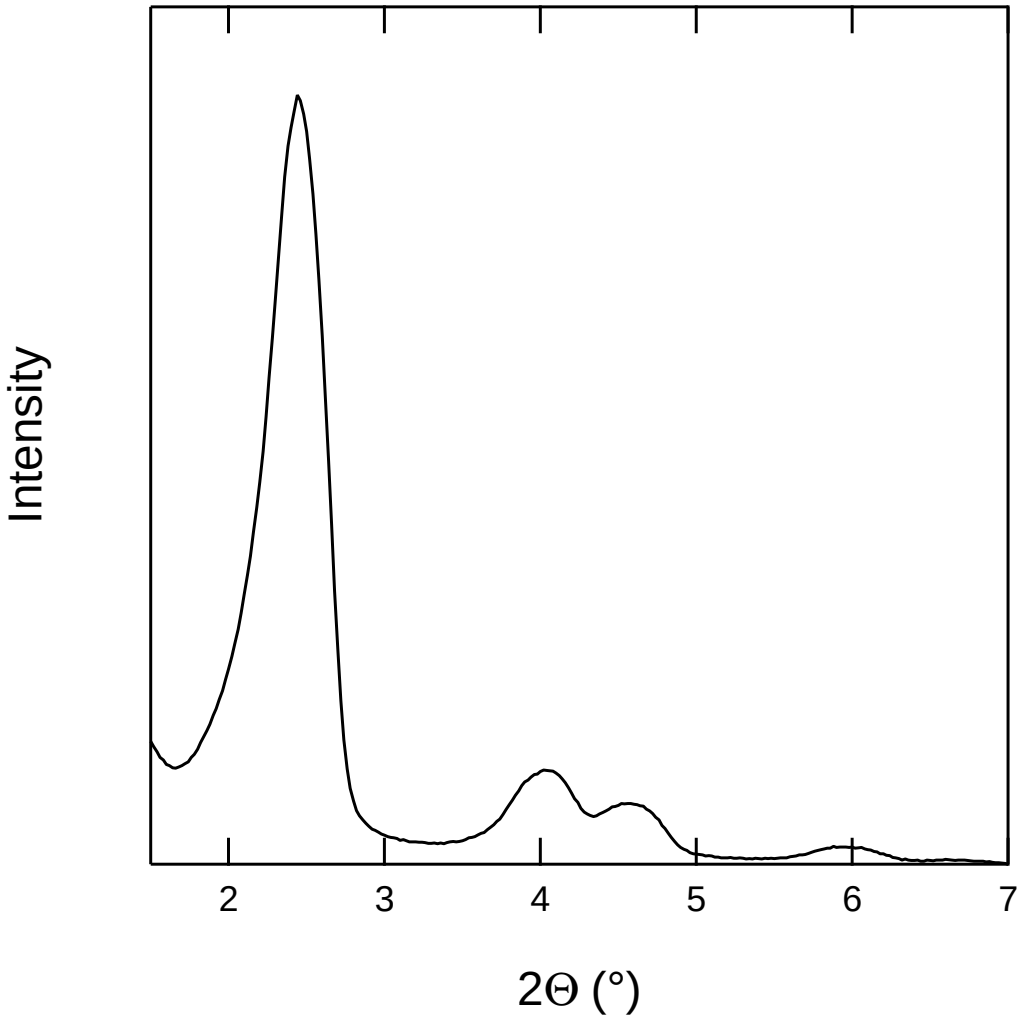

Figure 2.3 X-ray diffraction pattern for the parent MCM-41 material

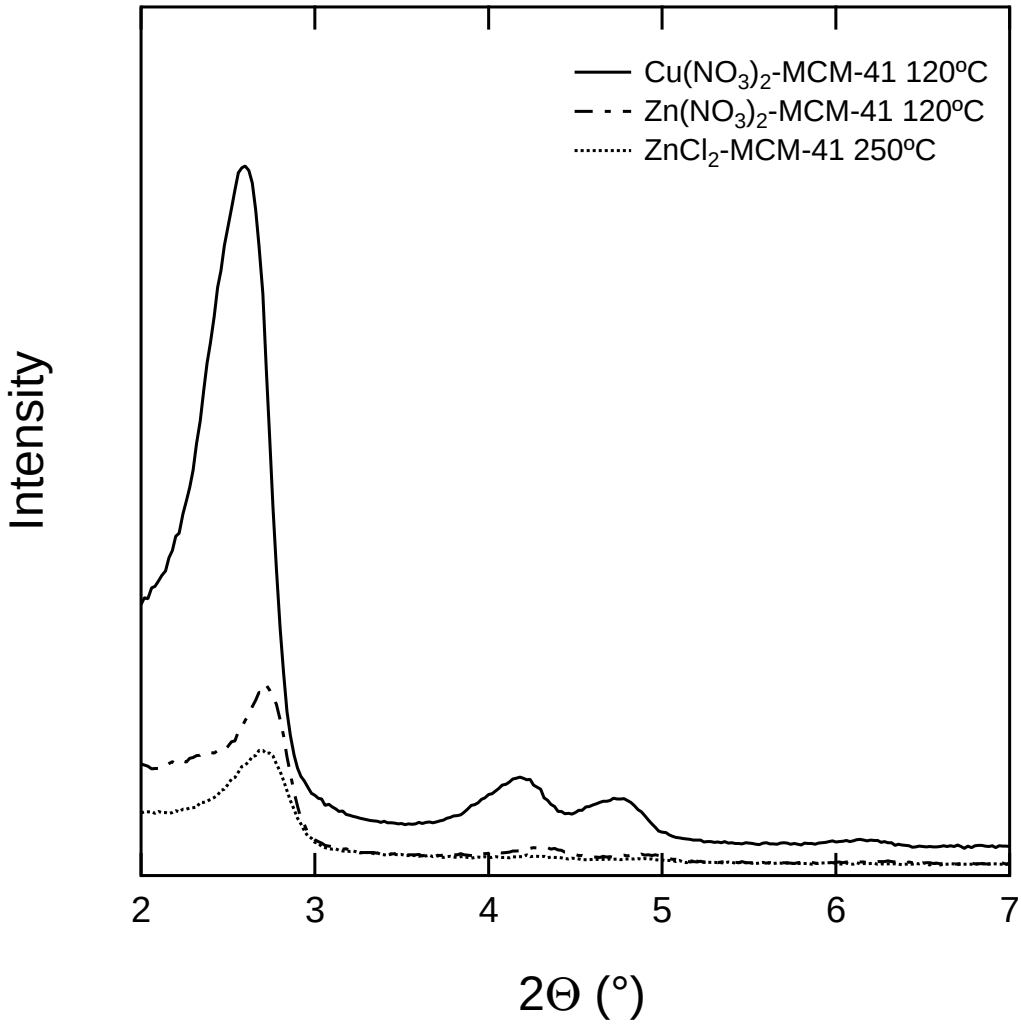

Figure 2.4 A representative small angle XRD scan for the $Cu(NO_3)_2$-MCM-41 sample conditioned at 120°C. When analyzed via XRD, all zinc and copper impregnated materials are similar to this spectrum

matrix with the addition of sulfuric acid. This is consistent with results from the nitrogen isotherms, which depict a decrease in surface area and pore volume after acid treatment.

XRD scans of the most effective metal salt-impregnated materials identified metal salt crystals in some samples. Specifically, the $Cu(NO_3)_2$-MCM-41 material conditioned at 120 °C showed evidence of copper nitrate hydroxide peaks. As shown in Figure 2.6, the spectrum acquired from this sample contains peaks at 12.7°, 25.5°, and 34° 2-theta, which correspond to the presence of copper nitrate hydroxide crystals.[34] Similar scans of $ZnCl_2$-MCM-41 conditioned at 250 °C and $Zn(NO_3)_2$-MCM-41 conditioned at 120 °C did not exhibit the respective metal salt peaks. This is attributed to the formation of small zinc salt crystals that are finely dispersed throughout the MCM-41 material.[35]

X-ray photoelectron spectroscopy

XPS was used to determine the quantity of zinc and sulfur in the $ZnSO_4$ impregnated samples that were used to determine the most effective conditioning method. These are summarized in Table 2.4. It is evident that the ratio of zinc to sulfur in the 540 °C sample is higher than that found in the other samples. The samples conditioned at 120 °C and 250 °C have Zn/S ratios of approximately 1, whereas the sample conditioned at 540 °C has a ratio of 1.9. This difference in Zn/S ratio between the high and low temperature samples is consistent with sulfurous compounds being liberated during the high temperature conditioning step and the zinc sulfate converting to zinc oxide, with the zinc migrating within the walls of MCM-41.[36,37] For additional verification of the rate process occuring at the high conditioning temperature, another sample of MCM-41 impregnated with $ZnSO_4$ was heated to 540 °C for three days. A comparison of the XPS spectra for the two 540 °C samples and the control sample conditioned at 120 °C is located in Figure 2.7. As shown in the figure, there is no sulfur peak present in the XPS scan after heating at 540 °C for three days. There

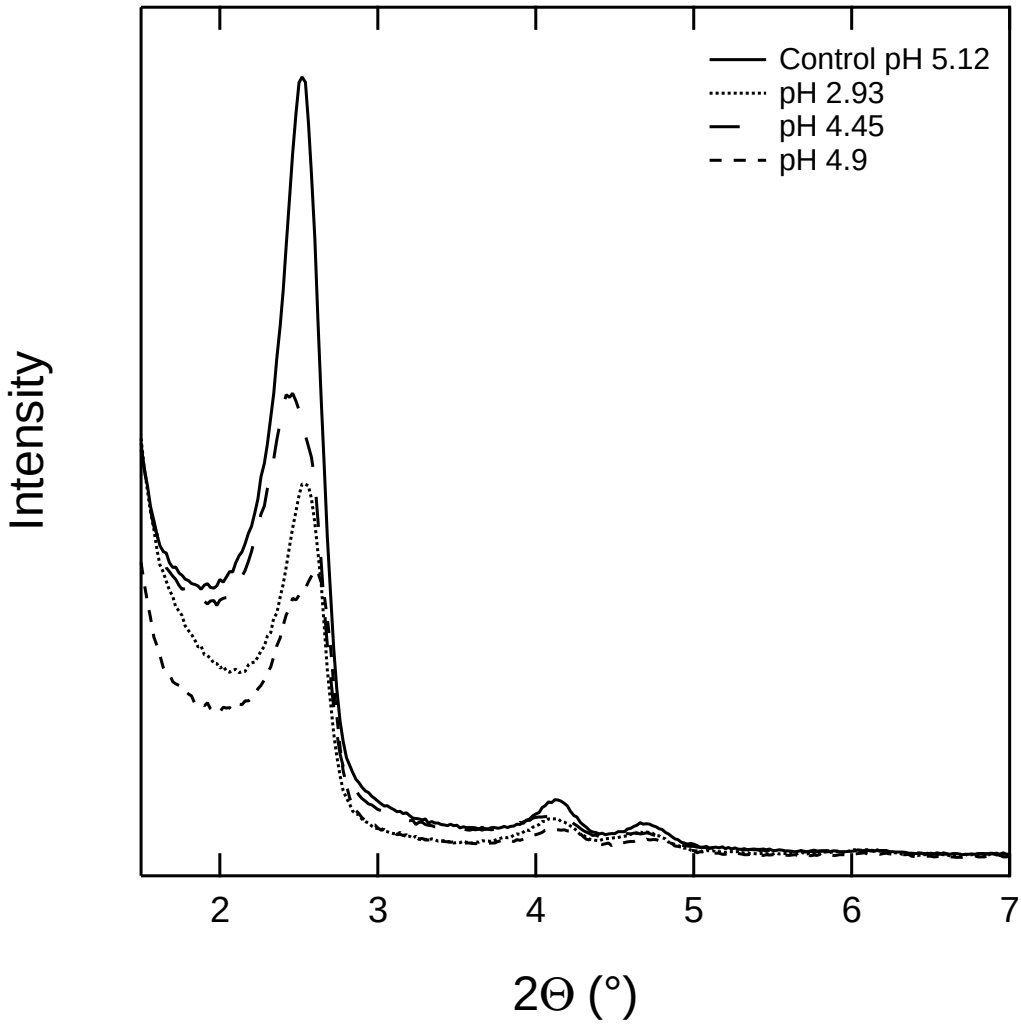

Figure 2.5 XRD spectra for the pH-adjusted $ZnSO_4$-MCM-41 impregnated samples. The control sample maintains higher order than the acidic samples.

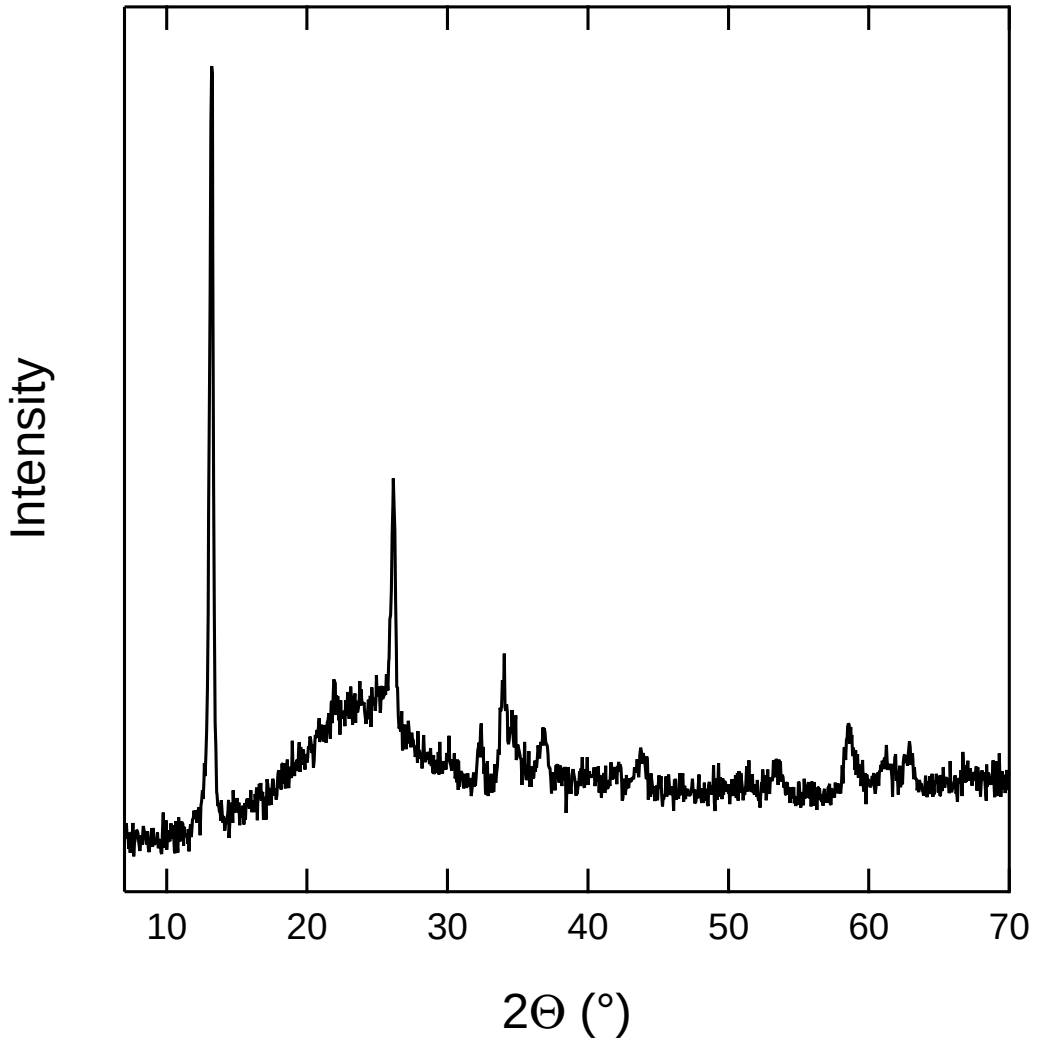

Figure 2.6 Large angle XRD scan of the $Cu(NO_3)_2$-MCM-41 sample conditioned at 120°C. The sample exhibits peaks at 12.7°, 25.5°, and 34°, which correspond to the presence of copper nitrate hydroxide

Table 2.4: Atomic percentages of species that comprise the $ZnSO_4$ impregnated material. All samples impregnated with a silicon to metal atomic ratio of 5.

Sample	Atomic % Oxygen	Atomic % Si	Atomic % Zn	Atomic % S	Zn/S Ratio
MCM-41	71.8	28.2	-	-	-
$ZnSO_4$-MCM-41 120 °C	71.2	27.0	0.8	0.8	1.0
$ZnSO_4$-MCM-41 250 °C	70.7	25.5	2.2	1.6	1.4
$ZnSO_4$-MCM-41 540 °C	69.6	25.6	3.1	1.6	1.9

is a slight broad increase associated with this spectrum; however, this is not likely a sulfur peak, but rather a Si 2s transition plasmon resonance peak. Consequently, high temperature conditioning decomposes the $ZnSO_4$ into Zn/ZnO and SO_2/SO_3, and the sulfurous compounds are liberated from these samples while the Zn remains.

A similar analysis of the uncrushed samples resulted in Zn/Si and Zn/S ratios similar to that of the ground samples. If the metal salt did not successfully migrate within the MCM-41 pores and remained outside of the MCM-41 matrix during impregnation, the Zn/Si ratio of the uncrushed sample would be larger than that of the crushed sample. Consequently, it is evident from this analysis that the impregnated $ZnSO_4$ was uniformly distributed throughout the MCM-41 matrix via impregnation.

Ammonia adsorption

The standard deviation of the average ammonia capacities, listed in Table 2.5, is higher than 3% because each average capacity was calculated from samples that were impregnated using two synthesis batches of MCM-41. Consequently, the standard deviations reflected in the table are representative of differences between samples rather than deviation in ammonia capacity measurement.

After varying the conditioning temperature, the $ZnSO_4$-MCM-41 samples were tested for their ammonia capacity. This information is summarized in Figure 2.8. It is evident from this figure that the sample held at 540 °C resulted in the lowest ammonia capacity of all $ZnSO_4$ impregnated samples. From this information, coupled with the XPS data for these samples, it is evident that more zinc and zinc oxide forms in the higher temperature sample versus the sample conditioned at 120 °C because the zinc sulfate decomposes during the high temperature heating. The depletion of zinc sulfate in the sample decreases the effectiveness of ammonia chemisorption. Because industrial applications of these materials often require high temperatures for synthesis and regeneration, the conditioning steps at 120 °C and 250 °C were chosen for investigation in the remaining samples.

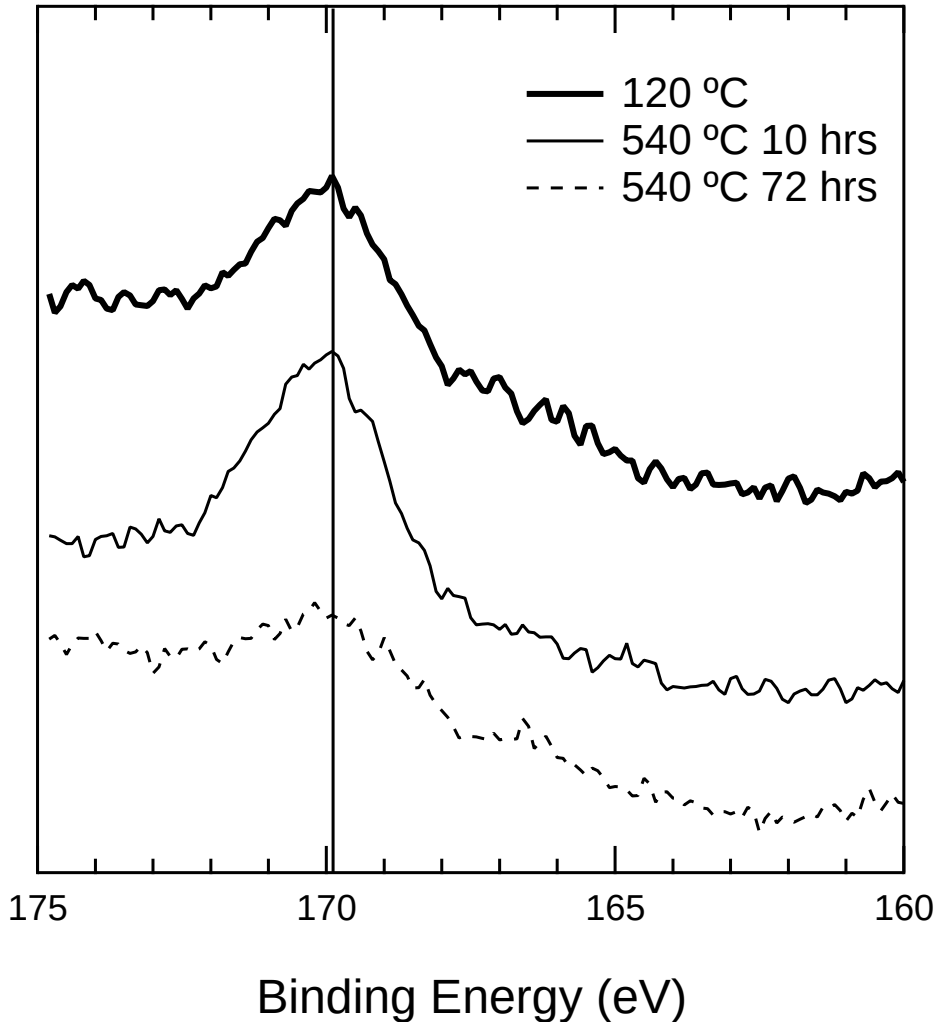

Figure 2.7 High resolution XPS spectra of sulfur peaks in the $ZnSO_4$-MCM-41 impregnated samples conditioned at 120 °C, 540 °C for 10 hours, and 540 °C for 72 hours.

Table 2.5: Ammonia capacities for all metal salt impregnated MCM-41 materials for 1133 mg/m^3 ammonia in helium. All samples impregnated with a silicon to metal atomic ratio of 5.

Sample	NH_3 Capacity (mol/kg) 120 °C			Avg NH_3 Capacity (mol/kg) 120 °C	NH_3 Capacity (mol/kg) 250 °C			Avg NH_3 Capacity (mol/kg) 250 °C
	batch 1	batch 2	batch 3		batch 1	batch 2	batch 3	
$ZnSO_4$-MCM-41	4.86	7.8	6.47	6.38 ±1.47	3.02	5.69		4.36 ±1.88
$CuSO_4$-MCM-41	4.5	6.8	4.71	5.65 ±1.62	4.79	5.04		4.92 ±0.17
$FeSO_4$-MCM-41	4.68	5.17		4.93 ±0.34	3.5	4.84		4.17 ±0.94
$Fe_2(SO_4)_3$-MCM-41	6.26	6.24		6.25 ±0.01	6.02	5.39		5.71 ±0.44
$Zn(NO_3)_2$-MCM-41	6.71	6.50		6.61 ±0.15	5.0	4.44		4.72 ±0.39
$Cu(NO_3)_2$-MCM-41	7.22	6.47		6.85 ±0.53	3.17	3.65		3.41 ±0.34
$Fe(NO_3)_3$-MCM-41	3.82	4.10		3.96 ±0.19	3.57	5.10		4.34 ±1.08
$ZnCO_3$-MCM-41	3.10	3.17		3.14 ±0.05	2.95	2.90		2.93 ±0.03
$CuCO_3$-MCM-41	2.30	2.64		2.47 ±0.24	2.54	2.52		2.53 ±0.01
$ZnCl_2$-MCM-41	6.68	6.15	5.85	6.23 ±0.42	7.5	5.95	6.66	6.70 ±0.77
CuCl-MCM-41	3.94	4.54		4.24 ±0.42	4.21	4.43		4.32 ±0.15
$CuCl_2$-MCM-41	5.46	4.82		5.14 ±0.45	4.66	4.17		4.42 ±0.35
$FeCl_2$-MCM-41	4.12	4.43		4.28 ±0.22	3.01	3.14		3.08 ±0.09
$FeCl_3$-MCM-41	3.68	4.40		4.04 ±0.51	3.72	3.72		3.72 ±0.00

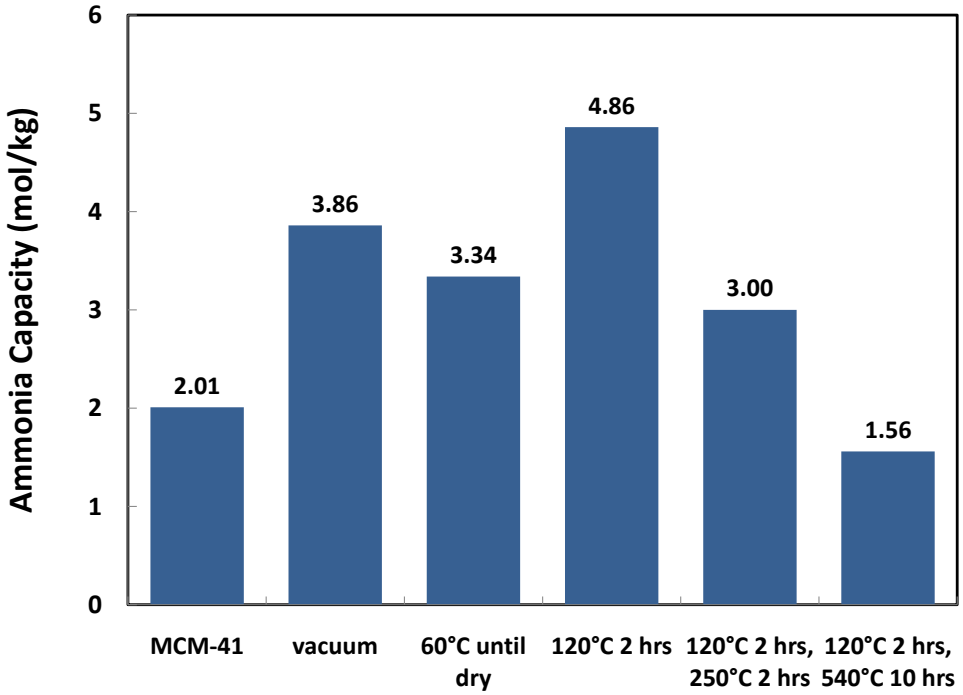

Figure 2.8 The effect of drying temperature on the ammonia capacity for the $ZnSO_4$-MCM-41 impregnated material.

Figure 2.9 depicts a lack of correlation between the ammonia capacity and the metal oxidation state of the impregnated samples conditioned at 120 °C. A similar trend is evident for the samples conditioned at 250 °C. For the metal salts tested, zinc always remains in the +2 oxidation state, copper varies from +1 to +2, and iron varies from +2 to +3. Based on this analysis, the metal type was determined to be more important in determination of ammonia capacity than the cation oxidation state at both conditioning temperatures. The lack of statistical significance can be expected because the chemisorption reactions occur based on the metal salt type rather than just on the oxidation state of the cation or anion.[3] As an example, the +2 oxidation states of copper, iron, and zinc compounds differ drastically in their reactivity towards ammonia, with average ammonia capacities ranging from 2.47 to 6.38 mol/kg. These can be compared to the ammonia capacity of the base, unimpregnated MCM-41, which is 2.0 mol/kg. Consequently, analyzing the impregnated materials based on their cationic oxidation states would combine the effects of the +2 oxidation states of zinc, copper, and iron, and negate the important differences in ammonia capacity that are inherent in the metal type used as the impregnant.

The pH was also expected to play an important role in ammonia capacity because ammonia is a basic gas that can participate in acid-base reactions. The intrinsic pH was measured during the aqueous impregnation step, when the same amount of water and MCM-41 was present in all samples. The pH measurement provides an indication of the acidity of the dry samples and may be used to predict the sample's affinity for participating in acid-base reactions.[21] The only difference affecting the pH of the samples is the presence of different metal salt impregnants. As shown in Figure 2.10, a lack of statistical correlation was found between the ammonia capacity and the pH of the MCM-41 samples impregnated with different metals. This figure compares the ammonia capacity of metal salt impregnated samples with different intrinsic pH values based on the acidic properties of the metal salt

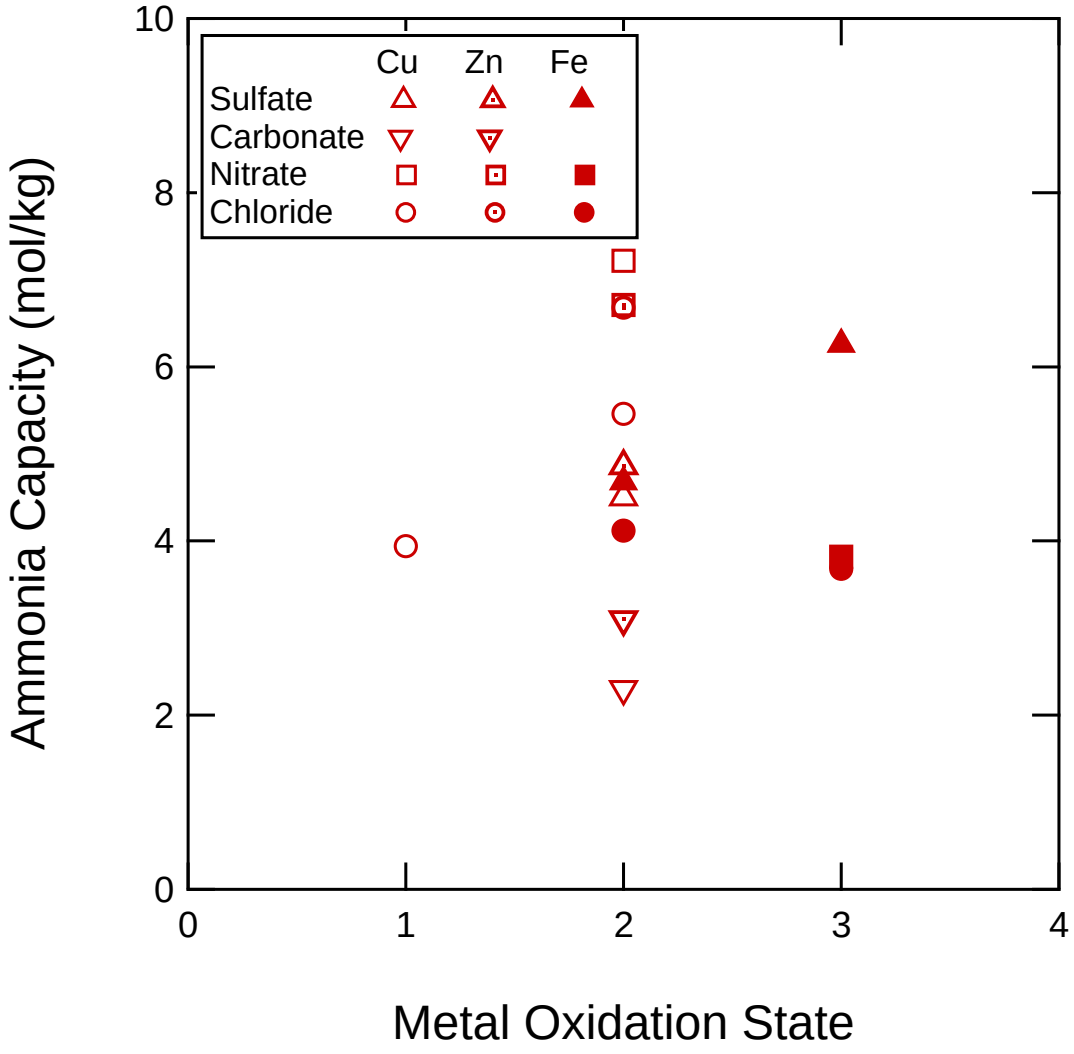

Figure 2.9 Ammonia capacity dependence on metal oxidation state for the impregnated materials.

impregnants.

An additional study was performed to determine the effect of varying pH on one of the metal salt impregnated samples. During synthesis of $ZnSO_4$-MCM-41, the pH of the mixture of water, $ZnSO_4$, and MCM-41 was adjusted using H_2SO_4 so as not to introduce new anions into the solution. The pH of these mixtures and the ammonia capacity of the final samples were compared. Based on the standard deviation associated with the ammonia capacity of the $ZnSO_4$ impregnated samples, this study showed no significant difference among the ammonia capacities of the pH-adjusted samples. As shown in Figure 2.11, the ammonia capacity was highest for the control sample due to it remaining the most ordered material, which was shown via XRD in Figure 2.5. However, taking into account the standard deviation associated with each sample, a more acidic solution pH did not correspond to a statistically significant increase in ammonia capacity. The next parameter investigated was the aqueous solubility of the metal salt. Because the impregnation of MCM-41 was performed in an aqueous solution, Figure 2.12 shows that the most insoluble metal salts, CuCl, $ZnCO_3$, and $CuCO_3$, also correspond to the lowest ammonia capacities at the 120 °C conditioning temperature. Figure 2.13 depicts a similar result for the samples conditioned at 250 °C. The decrease in ammonia capacity with respect to solubility is a result of low dispersion of the nearly insoluble metal salt within the MCM-41 matrix. Low solubility allows for aggregation of the metal salt and thereby decreases the surface area available for chemisorption with ammonia.

Statistical analysis of all samples conditioned at 120 °C shows that the metal type and anion type have the greatest effect on ammonia capacity. The analysis shows that both of these variables have low enough p-values, a common probability in statistical analysis, that they are statistically significant predictors of ammonia capacity.

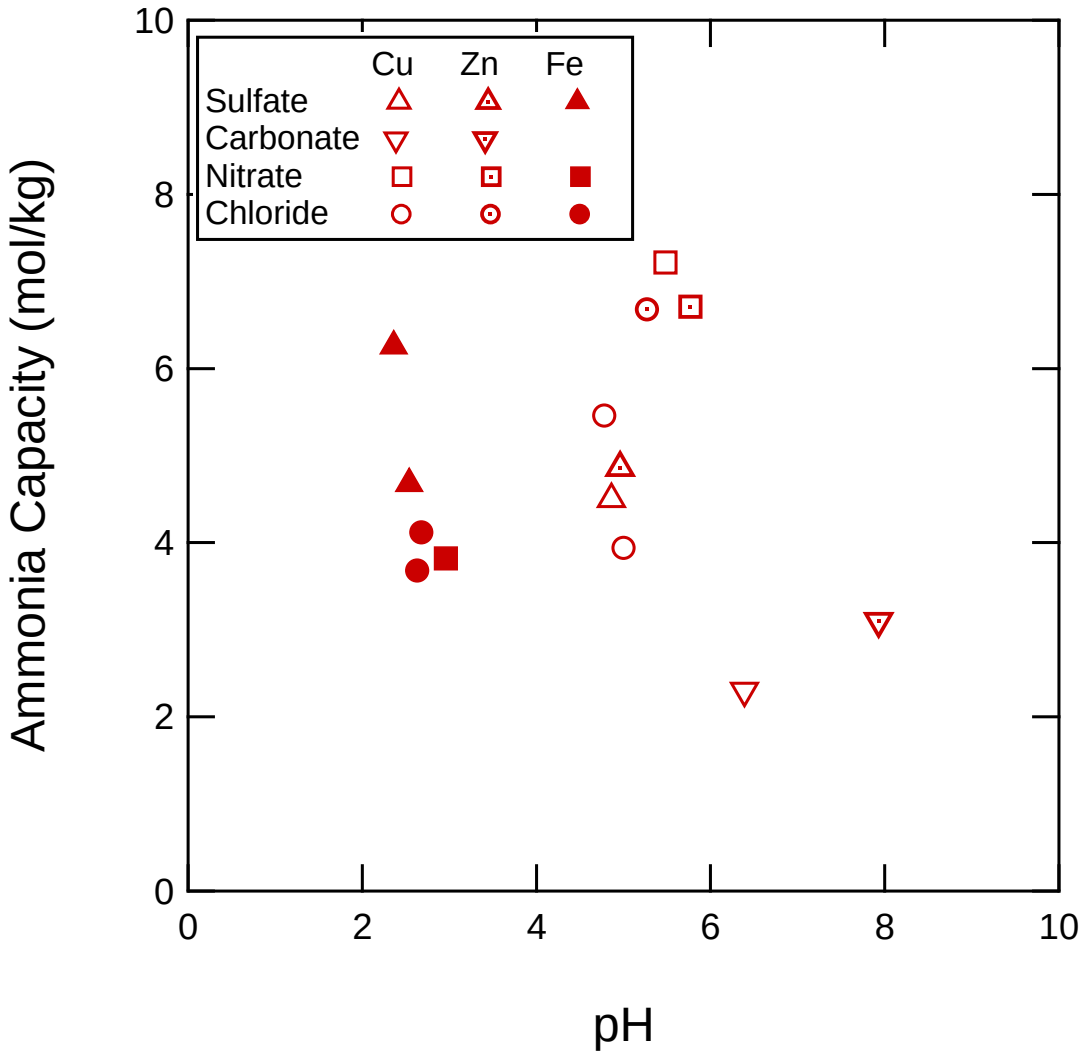

Figure 2.10 Ammonia capacity dependence on pH for the impregnated materials.

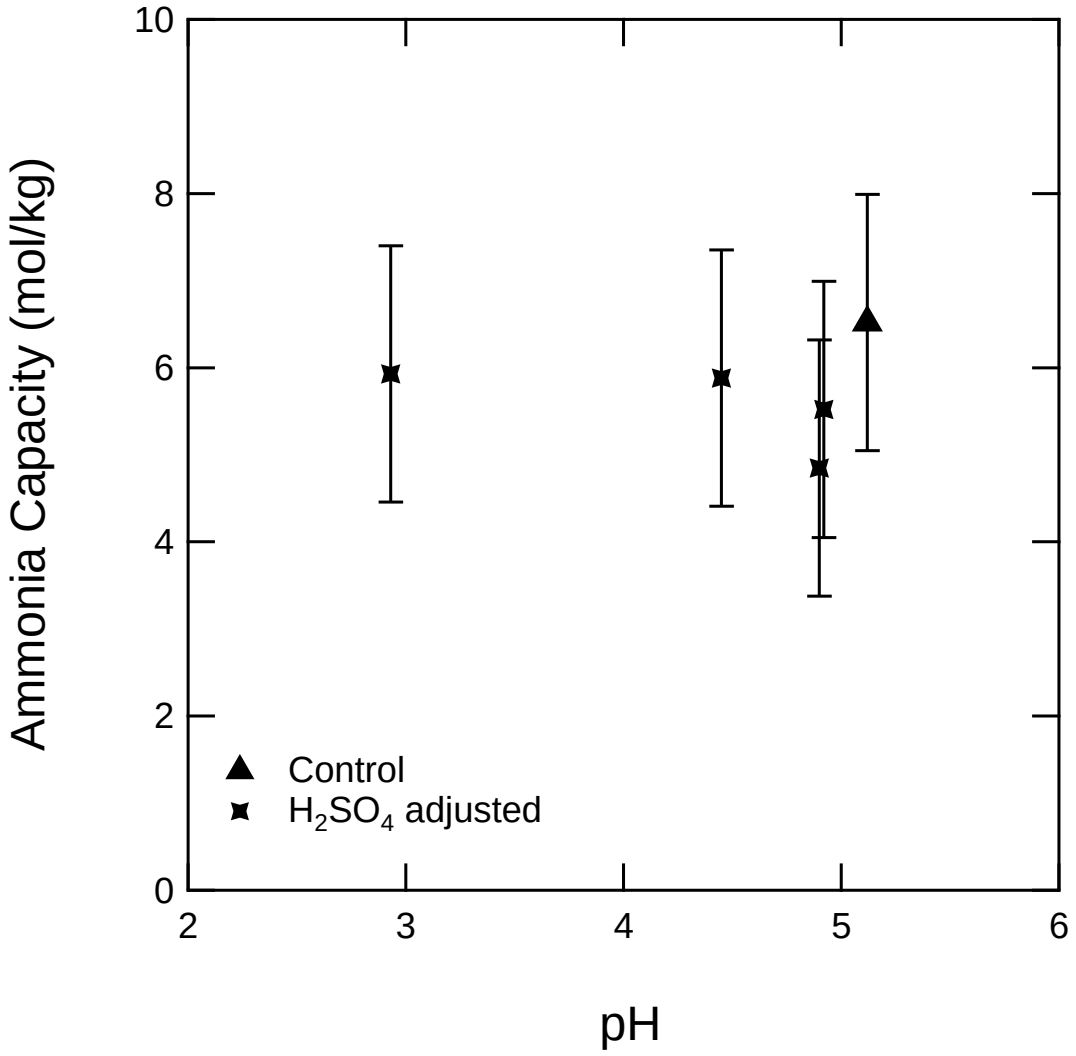

Figure 2.11 Ammonia capacity compared to pH of $ZnSO_4$-MCM-41 with pH adjusted by H_2SO_4

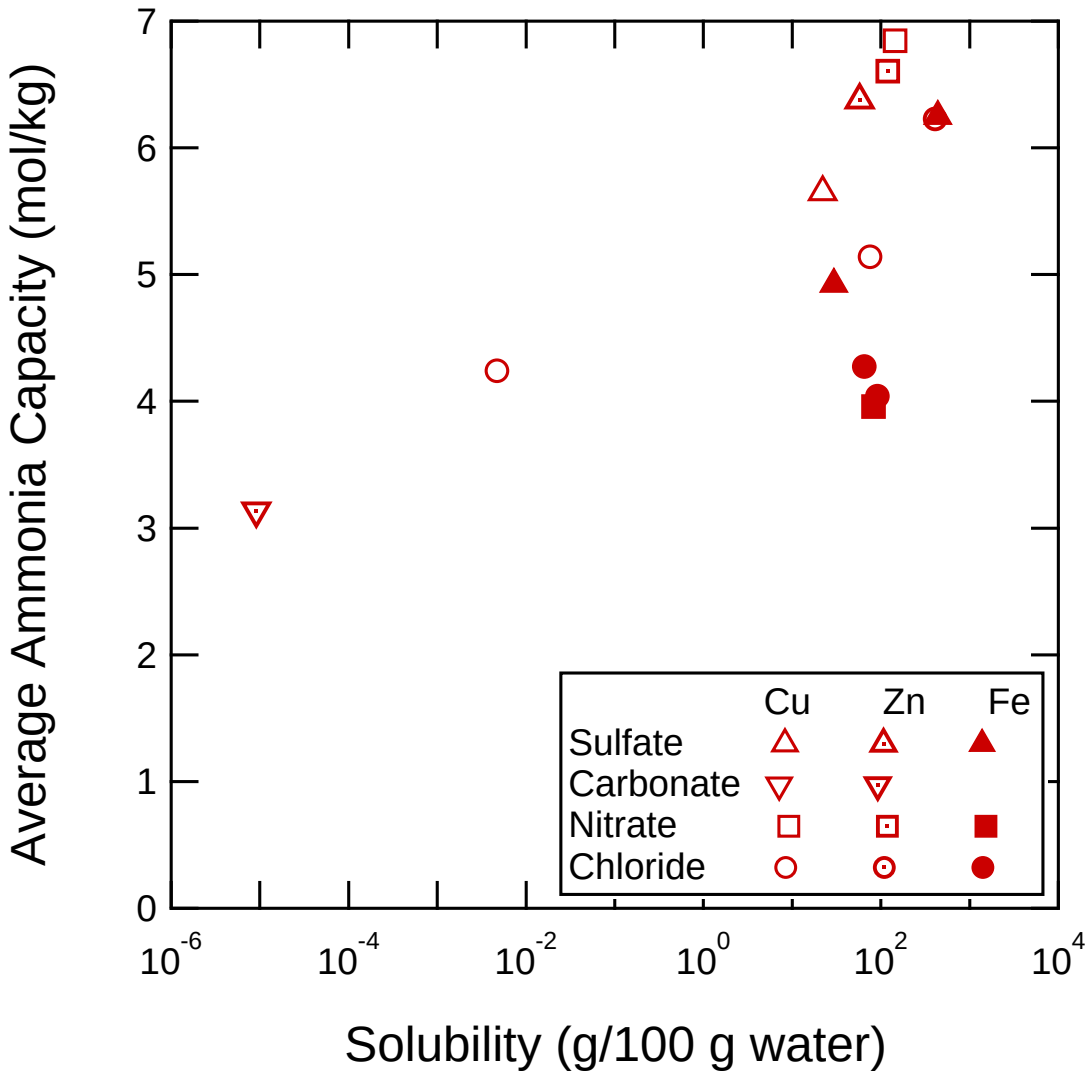

Figure 2.12 Ammonia capacity for samples conditioned at 120 °C compared to metal salt solubility

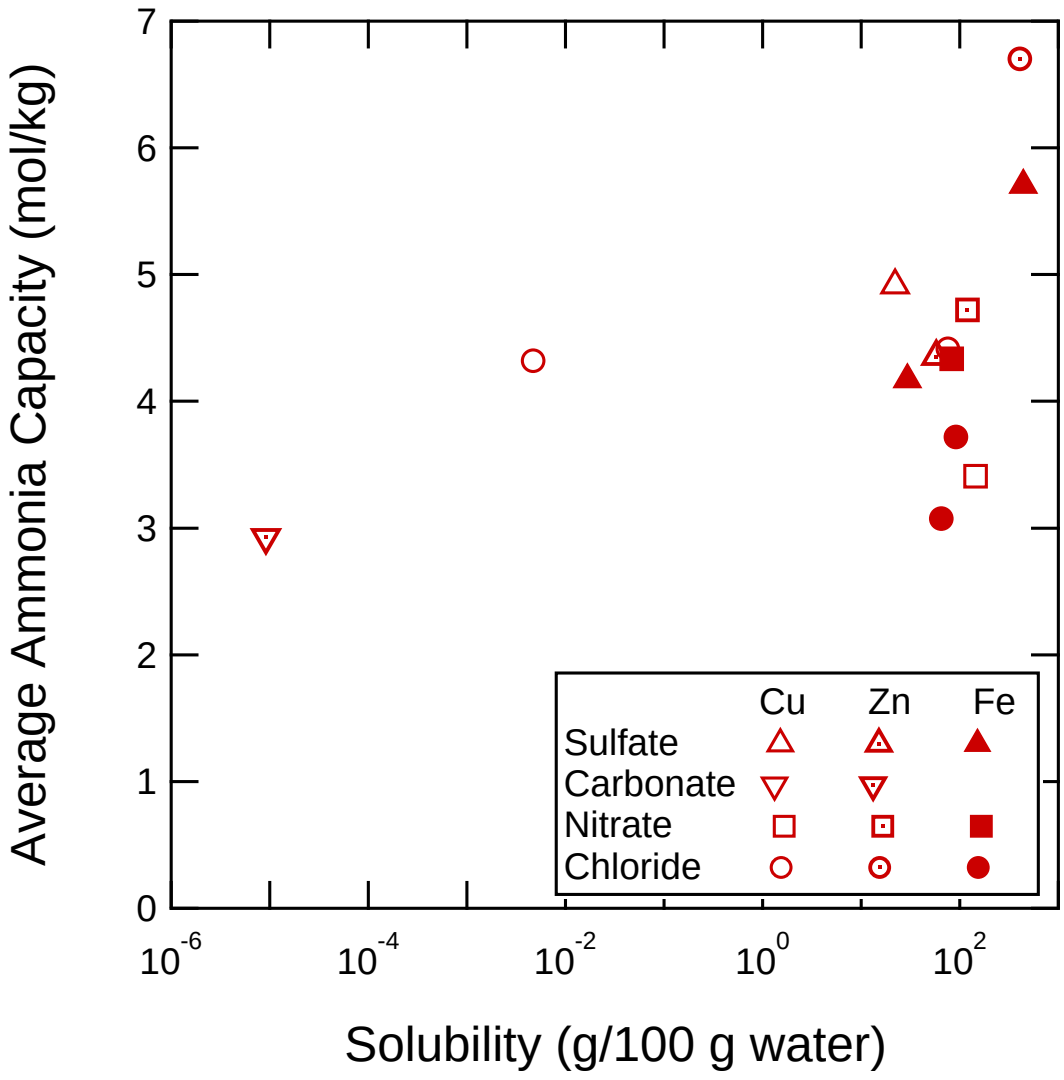

Figure 2.13 Ammonia capacity for samples conditioned at 250 °C compared to metal salt solubility

$$\text{Ammonia Capacity} = 4.43 + \begin{pmatrix} \text{-0.58 } Cu^{+1} \\ \text{0.45 } Cu^{+2} \\ \text{-0.55 } Fe^{+2} \\ \text{-0.49 } Fe^{+3} \\ \text{1.17 } Zn^{+2} \end{pmatrix} + \begin{pmatrix} \text{-2.43 } CO_3^{-2} \\ \text{0.39 } Cl^{-1} \\ \text{0.99 } NO_3^{-1} \\ \text{1.04 } SO_4^{-2} \end{pmatrix}$$

This model equation represents the statistics associated with the observed ammonia capacities and the metals and anions impregnated within the samples. The more positive or negative the coefficient, the larger the significance of that variable on the ammonia capacity. Consequently, zinc is the most effective metal at enhancing the ammonia capacity of the impregnated materials and Cu^{+1} is the least effective. At this temperature, the sulfates and nitrates show the most effectiveness at enhancing ammonia capacity, and carbonates are the least effective. From this analysis, it is evident that $ZnSO_4$ and $Zn(NO_3)_2$ impregnated into MCM-41 result in the highest ammonia capacities at the 120 °C conditioning temperature.

A similar analysis was carried out using the samples conditioned at 250 °C. As in the previous analysis, the metal and anion type were found to be the most statistically significant predictors of ammonia capacity. Analysis of these data produced the model equation

$$\text{Ammonia Capacity} = 3.83 + \begin{pmatrix} \text{-0.13 } Cu^{+1} \\ \text{-0.02 } Cu^{+2} \\ \text{-1.03 } Fe^{+2} \\ \text{-0.23 } Fe^{+3} \\ \text{0.95 } Zn^{+2} \end{pmatrix} + \begin{pmatrix} \text{-1.57 } CO_3^{-2} \\ \text{0.62 } Cl^{-1} \\ \text{-0.06 } NO_3^{-1} \\ \text{1.02 } SO_4^{-2} \end{pmatrix}$$

At 250 °C zinc is the most effective metal at enhancing ammonia capacity and iron is the least effective. For the anions, the sulfates and chlorides provide the most ammonia capacity enhancement and the carbonates provide the least. The sample in this group with the highest ammonia capacity was the $ZnCl_2$ impregnated MCM-41

sample, with an average ammonia capacity of 6.70 mol/kg. Table 2.5 summarizes the ammonia capacities for the metal impregnated samples at both conditioning temperatures, their average values, and the standard deviations associated with the averages for the metal salt impregnated samples. Figure 2.14 summarizes the data in a parity plot comparing the actual average ammonia capacities at both conditioning temperatures to the predicted capacities.

Analysis of variance using all data shows that the conditioning temperature plays a significant role in the ammonia capacity of the final samples. This is evident in the models derived for both conditioning temperatures, where the intercept in each equation represents the average ammonia capacity across all samples. The intercept at the 120 °C conditioning temperature is larger than that of the model constructed from the samples conditioned at 250 °C. Thus, the ammonia capacities tend to be higher for the samples conditioned at the lower temperature.

At both conditioning temperatures, the metal carbonate impregnants resulted in low ammonia capacities. One explanation for this is their minimal solubility in water, which inhibits a fine dispersion of these metal salts throughout the silica matrix, and decreases the surface area available for chemisorption when compared to more soluble metal salts. Another explanation can be gleaned from an analysis of the melting points of these materials. Carbonates generally have low melting points; $ZnCO_3$ has a melting point of 140 °C and $CuCO_3$ has a melting point of 200 °C, after which the carbonates decompose to their corresponding metals and metal oxides.[39] As shown in the temperature study of the $ZnSO_4$ impregnated samples, the decomposition of the metal salt decreases the ammonia capacity of the impregnated samples. Consequently, due to their low melting points and low solubilities, the metal carbonate impregnated samples exhibit the lowest ammonia capacities compared to all other materials.

The most effective impregnant at both conditioning temperatures was deter-

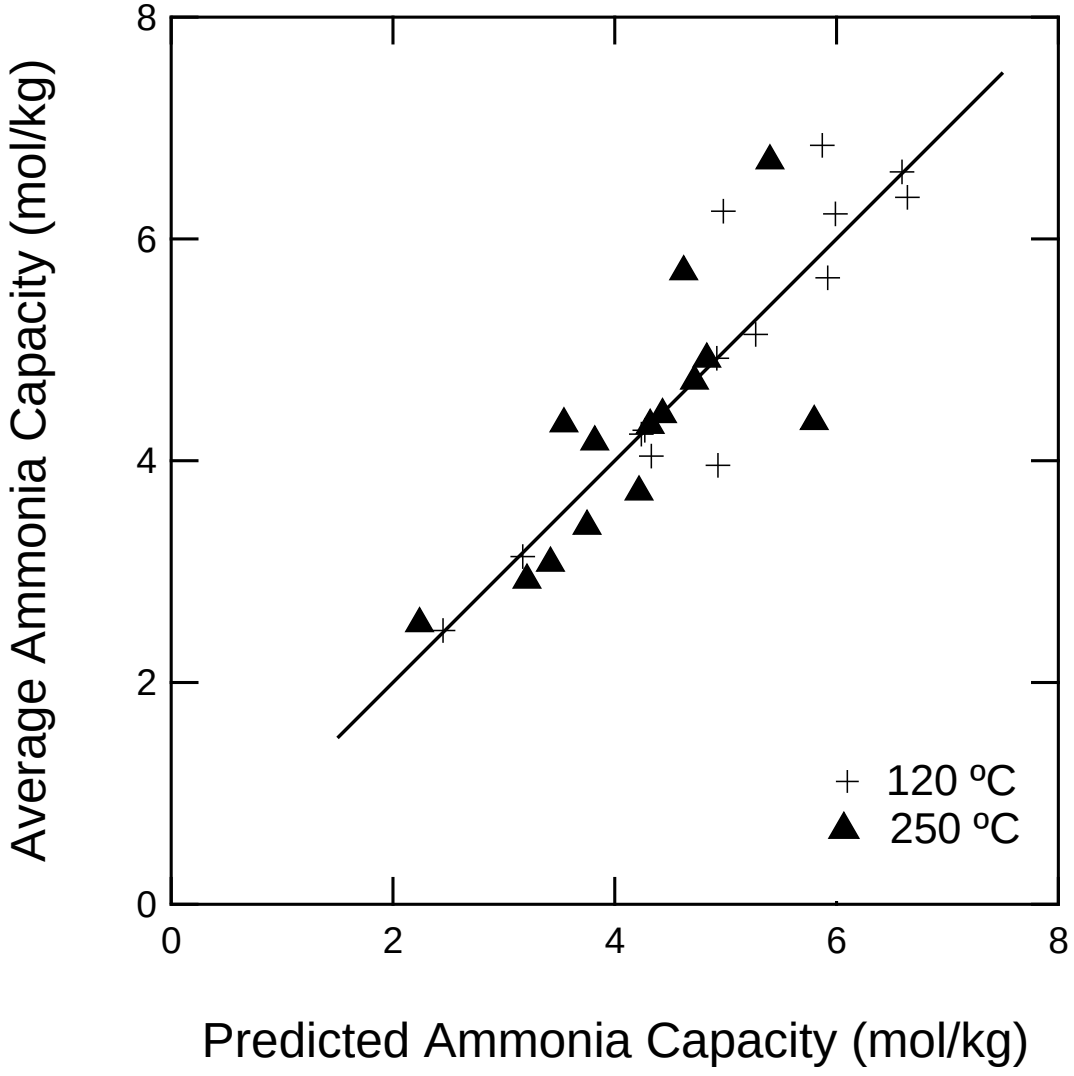

Figure 2.14 Parity plot comparing the actual average and predicted values of the ammonia capacities at both conditioning temperatures.

mined to be $ZnCl_2$. When conditioned at 120 °C, this sample exhibited an average ammonia capacity of 6.2 mol/kg. After conditioning at 250 °C, the average capacity rose to 6.7 mol/kg. $ZnCl_2$ as an impregnant resulted in samples with high ammonia capacities at both conditioning temperatures, compared to other metal salts that promoted high ammonia capacities at 120 °C but resulted in lower ammonia capacities after conditioning at the higher temperature. Consequently, $ZnCl_2$ was identified as the most robust metal salt impregnant.

This research into different metal salts has shown that both the cation and anion play an important role in complexing with the adsorbate molecule. Two coordination compounds between $ZnCl_2$ and NH_3 are proposed in the literature. Fortier et al.[5] proposed the formation of $ZnCl_2(NH_3)_x$ after impregnating activated carbon with varying concentrations of the metal salt and monitoring the reaction with ammonia. They initially proposed two for the value of x, as seen in the reaction below.

$$2NH_3(g) + ZnCl_2(ads) \rightarrow Zn(NH_3)_2Cl_2(ads)$$

This reaction has been reported by other sources as the reaction occuring when gaseous ammonia reacts with aqueous suspensions of $ZnCl_2$.[40,41] Fortier et al. concluded that under adsorption conditions, the value of x depends on the partial pressure of ammonia above the coordination compound. In the presence of water, Petit et al.[20] confirmed the formation of $ZnCl_2(NH_4)Cl$ using XRD, XRF, and FTIR analytical techniques. Because the equilibrium capacities in this study were determined under dry conditions, it is evident that $ZnCl_2(NH_3)_x$ is formed during adsorption.

The $ZnCl_2$-MCM-41 sample conditioned at the higher temperature was used as the basis for optimizing the amount of zinc chloride loaded within the MCM-41 support. Figure 2.15 shows the dependence of the ammonia capacity on the weight percent of zinc chloride impregnated into MCM-41. The 0 wt % sample consists only of MCM-41 and the 100 wt % sample consists of only zinc chloride. Table 2.6 gives the weight percentage of zinc chloride as the silicon to zinc atomic ratio. It is evident

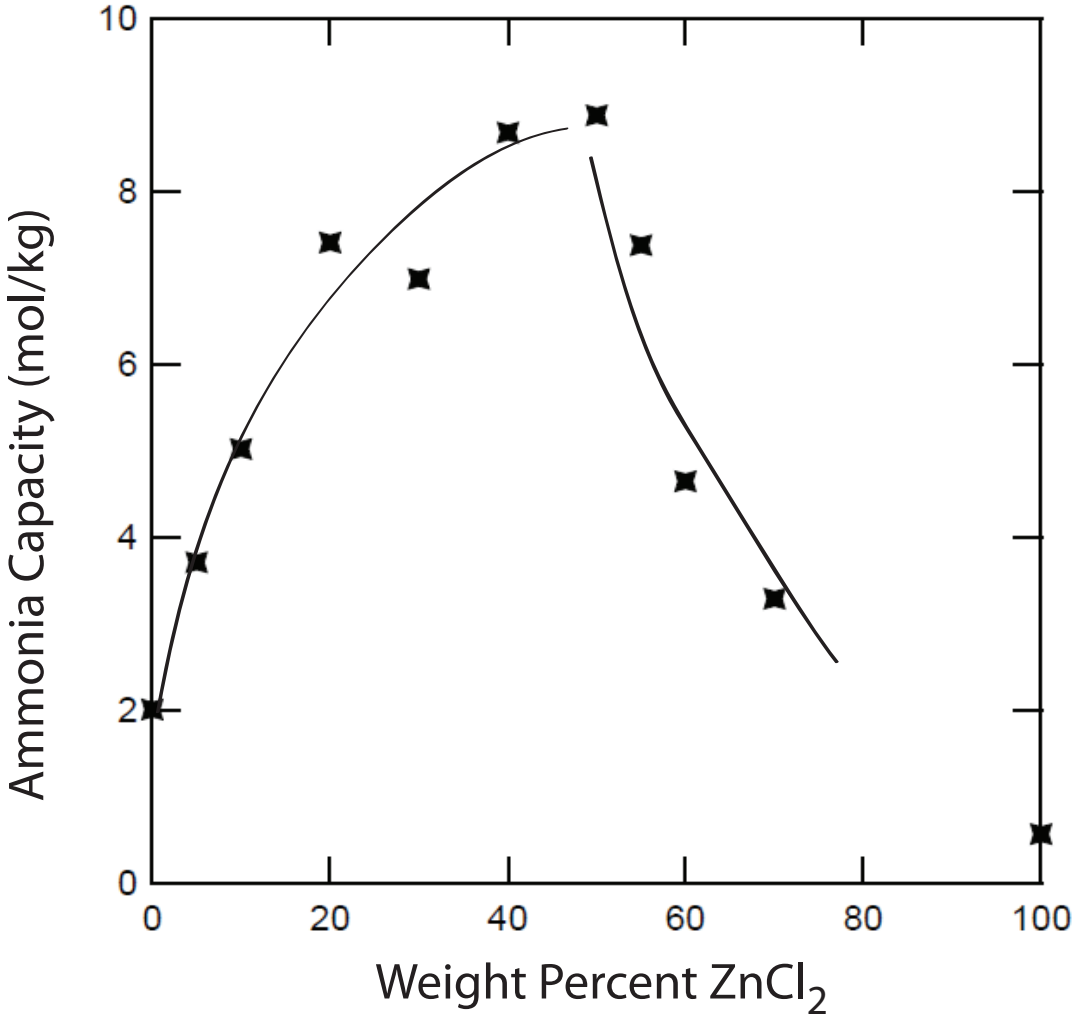

Figure 2.15 Comparison of different amounts of $ZnCl_2$ impregnated into MCM-41 and conditioned at 250 °C.

Table 2.6: Ammonia capacities and Si/Zn molar ratios of the $ZnCl_2$ impregnated MCM-41 samples. Capacities measured using 1133 mg/m^3 ammonia in helium.

wt % $ZnCl_2$	Si/Zn molar ratio	NH_3 Capacity (mol/kg)
0 wt %		2.01
5 wt %	43.2	3.71
10 wt %	20.4	5.02
20 wt %	9.1	7.41
30 wt %	5.3	6.99
40 wt %	3.4	8.68
50 wt %	2.3	8.88
60 wt %	1.5	4.65
70 wt %	0.97	3.29
100 wt %		0.57

Table 2.7: BET surface areas and pore volumes for MCM-41 impregnated with increasing amounts of $ZnCl_2$.

wt % $ZnCl_2$	S_{BET} (m^2/g)	V_{pore} (cm^3/g)
0 wt %	930	1.3
10 wt %	816	1.0
30 wt %	582	0.7
50 wt %	396	0.4
70 wt %	170	0.2

from Figure 2.15 that the ammonia capacity reaches a maximum at 50 wt % zinc, corresponding to a Si/Zn atomic ratio of 2.3. After this maximum, the zinc chloride can no longer effectively disperse throughout the silica matrix, which causes clumping of the zinc chloride and a decreased zinc chloride surface area for chemisorption. This corresponds to a decrease in ammonia capacity for the samples impregnated with higher concentrations of $ZnCl_2$. Nitrogen isotherms for select samples, summarized in Table 2.7, confirm a decrease in surface area and pore volume after impregnation with $ZnCl_2$. When considering industrial applications of these materials, impregnant amounts ranging from 20 to 50 wt % $ZnCl_2$ all yield high ammonia capacities.

2.4 Conclusions

MCM-41 samples impregnated with metal salts have been prepared via an aqueous impregnation method and conditioned at different temperatures. These samples were tested for material characteristics and ammonia capacity.

The initial $ZnSO_4$ impregnation study determined that the conditioning temperature has an effect on the ammonia capacity of the impregnated samples. A high temperature conditioning step resulted in the formation of Zn and ZnO from decomposition of $ZnSO_4$. A corresponding decrease in ammonia capacity was observed for the high temperature sample compared to those conditioned at lower temperatures.

At both 120 °C and 250 °C conditioning temperatures, the intrinsic metal salt pH and metal oxidation state were determined not to be statistically significant ammonia capacity predictors. Insoluble metal salts, specifically the metal carbonates, were found to have lower ammonia capacities at both conditioning temperatures due to the aqueous impregnation method used.

The metal type and anion type were found to be the most statistically significant predictors of ammonia capacity for the impregnated samples. For samples at both conditioning temperatures, zinc was identified as the metal yielding the highest ammonia capacity. At 120 °C, the anions yielding the highest ammonia capacities were the sulfates and nitrates, whereas at 250 °C, the sulfates and chlorides were the most effective. At both conditioning temperatures, impregnating with the carbonates resulted in the lowest ammonia capacities.

Across all samples and conditioning temperatures, the MCM-41 sample impregnated with $ZnCl_2$ and conditioned at 250 °C resulted in the highest average ammonia capacity. Consequently, the concentration of $ZnCl_2$ impregnated into MCM-41 was optimized for this condition. The ammonia capacity is the highest for MCM-41 impregnated with 50 wt % $ZnCl_2$, which corresponds to a Si/Zn molar ratio of 2.27. The ammonia capacity remains high between 20 wt % $ZnCl_2$ and 50 wt % $ZnCl_2$;

there is less than a 25% change between the ammonia capacities in this range of impregnated samples. After 50 wt % $ZnCl_2$ loading, the ammonia capacity decreases because the metal salt is present at too high a concentration to be well dispersed throughout the MCM-41 matrix.

References

[1] C.T. Kresge, M.E. Leonowicz, W.J. Roth, J.C. Vartuli, J.S. Beck. Ordered mesoporous molecular sieves synthesized by a liquid crystal template mechanism. *Nature*, 1992, **359**, 710-712.

[2] B. Marler, U. Oberhagemann, S. Vortmann, H. Gies. Influence of the sorbate type on the XRD peak intensities of loaded MCM-41. *Microporous Mater.*, 1996, **6**, 375-383.

[3] W.A. Noyes, Military problems with aerosols and nonpersistent gases, summary technical report of division 10, National Defense Research Committee, Washington, D.C., 1946.

[4] Department of Health and Human Services,, National Institutes of Occupational Safety and Health, 2003.

[5] H. Fortier, P. Westreich, S. Selig, C. Zelenietz, J.R. Dahn. Ammonia, cyclohexane, nitrogen and water adsorption capacities of an activated carbon impregnated with increasing amounts of ZnCl2, and designed to chemisorb gaseous NH3 from an air stream. *J. Colloid Interface Sci.*,2008, **320**, 423-435.

[6] B.A. Morrow, I.A. Cody, L.S.M. Lee. Infrared studies of reaction on oxide surfaces: structure of chemisorbed ammonia on silica. *J. Phys. Chem.*, 1975, **79**, 2405-2408.

[7] B.A. Morrow, I.A. Cody. Infrared studies of reaction on oxide surfaces: active-sites on dehydroxylated silica for chemisorption of ammonia and water. *J. Phys. Chem.*, 1976, **80**, 1998-2004.

[8] S. Kittaka, M. Morimura, S. Ishimaru, A. Morino, K. Ueda. Effect of confinement on the fluid properties of ammonia in mesopores of MCM-41 and SBA-15. *Langmuir*, 2009, **25**, 1718-1724.

[9] N. Chino, T. Okubo. Nitridation mechanism of mesoporous silica: SBA-15. *Microporous Mesoporous Mater.*,2005 **87**, 15-22.

[10] V. Ravat, D.B. Mantri, P. Selvam, P. Aghalayam. Platinum group metals substituted MCM-41 molecular sieves: Synthesis, characterization and application as novel catalysts for the reduction of NO by CO. *J. Mol. Catal. A: Chem.*, 2009, **314**, 49-54.

[11] C. Chanquia, K. Sapag, E. Rodriguez-Castellon, E. Herrero, G. Eimer. Nature and location of copper nanospecies in mesoporous molecular sieves. *J. Phys. Chem. C*, 2010, **114**, 1481-1490.

[12] D. Lensveld, J. Mesu, A. van Dillen, K. de Jong. Synthesis and characterisation of MCM-41 supported nickel oxide catalysts. *Microporous Mesoporous Mater.*, 2001, **44-45**, 401-407.

[13] R. Savidha, A. Pandurangan. Vapour phase isopropylation of phenol over zinc- and iron-containing Al-MCM-41 molecular sieves. *Appl. Catal., A*, 2004, **262**, 1-11.

[14] D.A. Sheppard, C.E. Buckley. Hydrogen adsorption on porous silica. *Int. J. Hydrogen Energy*, 2008, **33**, 1688-1692.

[15] A. Vinu, K. Nandhini, V. Murugesan, W. Bohlmann, V. Umamaheswarl, A. Poppl, M. Hartmann. Mesoporous FeAlMCM-41: an improved catalyst for the vapor phase tert-butylation of phenol. *Appl. Catal., A*, 2004, **265**, 1-10.

[16] C. Wu, Q. Gao, J. Hu, Z. Chen, W. Shi. Rapid preparation, characterization and hydrogen storage properties of pure and metal ions doped mesoporous MCM-41. *Microporous Mesoporous Mater.*, 2009, **117**, 165-169.

[17] A. Gervasini, C. Messi, P. Carniti, A. Ponti, N. Ravasio, F. Zaccheria. Insight into the properties of Fe oxide present in high concentrations on mesoporous silica. *J. Catal.*, 2009, **262**, 224-234.

[18] L.M. LeLeuch, T.J. Bandosz. The role of water and surface acidity on the reactive adsorption of ammonia on modified activated carbons. *Carbon*, 2007, **45**, 568-578.

[19] C. Canals-Batile, A. Ros, M.A. Lillo-Rodenas, E. Fuente, M.A. Montes-Moran, M.J. Martin, A. Linares-Solano. Carbonaceous adsorbents for NH3 removal at room temperature. *Carbon*, 2008, **46**, 176-178.

[20] C. Petit, C. Karwacki, G. Peterson, T.J. Bandosz. Interactions of ammonia with the surface of microporous carbon impregnated with transition metal chlorides. *J. Phys. Chem. C*, 2007, **111**, 12705-12714.

[21] M. Seredych, T.J. Bandosz. Effects of surface features on adsorption of SO(2) on graphite oxide/Zr(OH)(4) composites. *J. Phys. Chem. C*, 2010, **114**, 14552-14560.

[22] J.W.H. Smith, P. Westreich, L.M. Croll, J.H. Reynolds, J.R. Dahn. Understanding the role of each ingredient in a basic copper carbonate based impregnation recipe for respirator carbons. *J. Colloid Interface Sci.*, 2009, **337**, 313-321.

[23] C. Petit, K. Kante, T.J. Bandosz. The role of sulfur-containing groups in ammonia retention on activated carbons. *Carbon*, 2010, **48**, 654-667.

[24] C.J. Jones, d-and f-Block Chemistry, Royal Society of Chemistry, Cambridge, 2001.

[25] M.R.A. Blomberg, P.E.M. Siegbahn, M. Svensson. Theoretical study of the activation of the N-H bond in ammonia by 2nd row transition metal atoms. *Inorg. Chem.*, 1993, **32**, 4218-4225.

[26] S.K. Bhargava, D.B. Akolekar. Adsorption of NO and CO over transition-metal-incorporated mesoporous catalytic materials. *J. Colloid Interface Sci.*, 2005, **281**, 171-178.

[27] The International Union of Pure and Applied Chemistry, Pure and Applied Chemistry 67 (1995) 1257-1306.

[28] T.G. Glover, K.I. Dunne, R.J. Davis, M.D. LeVan. Carbon-silica composite adsorbent: Characterization and adsorption of light gases. *Microporous Mesoporous Mater.*, 2008, **111**, 1-11.

[29] J. Silvestre-Albero, A. Sepulveda-Escribano, F. Rodriguez Reinoso. Preparation and characterization of zinc containing MCM-41 spheres. *Microporous Mesoporous Mater.*, 2008, **113**, 362-369.

[30] M. Naderi, J.L. Pickett, M.J. Chinn, D.R. Brown. Modified mesoporous silicates for the adsorption and decomposition of toxic gases. *J. Mater. Chem.*, 2002, **12**, 1086-1089.

[31] T. Hasegawa, Y. Shirotori, K. Ozawa, K. Edamoto, K. Takahashi. Room temperature adsorption of NH3 on Zn-terminated ZnO(0001). *Appl. Surf. Sci.*, 2004, **237**, 352-357.

[32] C.-M. Hung. Catalytic decomposition of ammonia over bimetallic CuO/CeO(2) nanoparticle. *Aerosol and Air Quality Research*, 2008, **8**, 447-458.

[33] D. Trong On, S.M.J. Zaidi, S. Kaliaguine. Stability of mesoporous aluminosilicate MCM-41 under vapor treatment, acidic and basic conditions. *Microporous Mesoporous Mater.*, 1998, **22**, 211-224.

[34] International Centre for Diffraction Data, Powder Diffraction File: Alphabetical Indexes: Sets 1-46, Newtown Square, PA, 1996.

[35] T. Tsoncheva, J. Rosenholm, M. Linden, F. Kleitz, M. Tiemann, L. Ivanova, M. Dimitrov, D. Paneva, I. Mitov, C. Minchev. Critical evaluation of the state of iron oxide nanoparticles on different mesoporous silicas prepared by an impregnation method. *Microporous Mesoporous Mater.*, 2008, **112**, 327-337.

[36] R. Narayah, A. Tabatabaie-Raissi, M.J. Antal. A study of zinc sulfate decomposition at low heating rates. *Ind. Eng. Chem. Res.*, 1988, **27**, 1050-1058.

[37] W. Suchanek. Systematic study of hydrothermal crystallization of zinc oxide (ZnO) nano-sized powders with superior UV attenuation. *J. Cryst. Growth*, 2009, **312**, 100-108.

[38] J.F. Moulder, W.F. Stickle, P.E. Sobol, K.D. Bomben, Handbook of X-ray Photoelectron Spectroscopy: A Reference of Standard Spectra for Identification and Interpretation of XPS Data, Chigasaki City, Japan, 2007.

[39] D.R. Lide, W.M. Haynes, CRC Handbook of Chemistry and Physics, CRC Press, Boca Raton, 2009.

[40] C. Perchard, A. Novak. Low frequency infrared and raman spectra of ammonia and imidazole complexes of zinc(II) halides. *Spectrochim. Acta*, 1970, **26A**, 871-881.

[41] P.J. Gardner, P. Pang, S. Preston. Thermodynamics of the dissociation of ZnCl2(NH3)2 by modified entrainment. *Thermochim. Acta*, 1989, **138**, 371-374.

CHAPTER III

MESOPOROUS SILICA-METAL ORGANIC COMPOSITE: SYNTHESIS, CHARACTERIZATION, AND AMMONIA ADSORPTION

3.1 Introduction

Air purification is an integral technology in today's society. With the advent of air quality concerns ranging from pollution to terrorism, the ability to remove light gases such as toxic industrial chemicals from air or other gases is a necessity. In order to have high capacities for contaminant removal, adsorbent materials with high surface areas and small pore sizes are preferred. The introduction of metal active sites into adsorbent materials for chemisorption is also desired for air purification using single pass filters.[1–8]

Research into next generation adsorbent materials is ongoing. Some of the top candidates in this field among new materials are metal organic frameworks (MOFs), which exhibit large surface areas and open structures and can have high capacities for light gases.[9] MOFs consist of metal ions coordinated with organic linkers to form porous materials with extremely high surface areas and low densities.[10] The surface areas and pore sizes of these materials vary based on the size and type of the organic linkers, which are coordinated to metal oxide clusters to provide inorganic reactive sites that enhance the chemisorptive ability of the materials.[11] Variation in the type of metal oxide clusters allows these adsorbent materials to be designed for removal of targeted gases.

One major hurdle to wide-spread utilization of MOFs is their poor hydrothermal stability. The structure and porosity of some MOFs collapse upon exposure to water and high temperatures, thereby reducing their effectiveness for many air purification applications.[12,13] One such MOF, CuBTC, has unsaturated metal centers in

its crystal structure, and water molecules have been found to bond quite strongly to these.[14] Kusgens et al.[15] reported that CuBTC can adsorb 35 mol/kg water and not all of the molecules can be desorbed because of the chemisorption of free water on the unsaturated metal centers. According to the steam stability map generated by Low et al.,[12] CuBTC is a MOF that exhibits moderate hydrothermal stability. Liu et al.[13] reported that CuBTC is prone to lose carbon dioxide capacity after repeated water/carbon dioxide mixture isotherm measurements. In order for adsorption processes to be used with variable gas stream conditions in purification applications, adsorbents with better hydrothermal stabilities and high gas capacities are desirable.

Ordered mesoporous silicate (OMS) materials are a family of siliceous materials that are popular adsorbents due to their large surface areas and ordered porous structures. OMSs are formed via a liquid crystal templating mechanism using ionic surfactants as structure directing agents.[16] The mesoporous materials can be synthesized by condensing silica onto surfactant liquid crystals and then removing the surfactant from the final product.[17] These silica materials tend to have high adsorption capacities for some basic gases, such as ammonia,[18–20] and extensive modifications of OMS materials have been performed to enhance their adsorptive ability for other light gases. OMS materials are often used as structure directing agents to form carbonaceous materials with smaller pore sizes. They also can be used as the base material for composite materials.[21] Some OMS materials, such as highly ordered MCM-41, have been found to be stable at high temperature and relative humidities.[22–24]

Research on metal organic-containing composites has focused on incorporating carbonaceous materials into the composites. Petit and Bandosz[25–27] have reported a composite material made of MOF-5 and graphite oxide. It showed improvement in ammonia capacity in a dry environment when compared to a mixture of the two solids. However, the material was found to be unstable when tested at higher relative humidity. The group also reported a composite of CuBTC and graphite oxide which

showed better hydrothermal stability.[28] Yang et al.[29] have reported the synthesis of a MOF-carbon nanotube composite. It was found to have higher surface area, enhanced thermal stability, and higher hydrogen storage capacity when compared to the base MOF material. Liu et al.[30] used MOF-5 as a template for a high surface area furfuryl alcohol-based carbonaceous material. After synthesis of the composite, the MOF was removed and the carbonaceous material was found to have an ultra-high surface area, on the order of 3000 m^2/g. Finally, Hundal et al.[31] successfully incorporated polyoxometalate anions into CuBTC and produced a thermally stable, microporous adsorbent material. Based on N_2 isotherm analysis, the composite material had a lower surface area than the initial CuBTC.

Ammonia is a toxic industrial chemical that has been widely studied for air filtration applications. According to guidelines set by the U. S. Occupational Safety and Health Administration,[32] ammonia is unsafe for human exposure above 35 ppm_v for fifteen minutes or 25 ppm_v for eight hours. Several studies have considered the adsorption of pure ammonia at equilibrium conditions. Helminen et al.[33] reported ammonia adsorption in traditional adsorbents, including activated carbon, alumina, polymer resin, silica gel, and several Type A and X zeolites. At room temperature and with pure ammonia at 1 atmosphere pressure, alumina, silica gel, and activated carbon have capacities ranging from 2.2 mol/kg to 5.3 mol/kg, while 13X zeolite and polymer resin have values of 9.0 mol/kg and 11.3 mol/kg, respectively. In a more recent study, Doonan et al.[34] showed that a covalent organic framework, COF-10, has a large equilibrium pure ammonia capacity at STP of approximately 15 mol/kg. To gather information closer to adsorbent operating conditions, other studies have investigated ammonia capacities at lower ammonia concentrations and under dynamic conditions. Britt et al.[11] studied harmful gas adsorption in different MOFs and obtained a dynamic ammonia capacity of 5.1 mol/kg for CuBTC with 1% NH_3 in a mixed gas. Petit et al.[28] reported a dynamic ammonia capacity of 8.8 mol/kg for

a CuBTC/graphene composite using 1000 ppm NH_3 in dry air. For air filtration applications, the concentration of ammonia in product air is generally in the parts per million range and closer to the testing conditions by Britt et al. and Petit et al. rather than those reported using pure ammonia. Because this research focuses on air filtration, the following study includes the measurement of ammonia equilibrium capacities at a reduced ammonia concentration (1500 ppm_v), which is orders of magnitude more dilute than pure ammonia, and generally yields lower ammonia capacity values for common adsorbents.

To date, there have been no published accounts of composite materials composed of an ordered mesoporous silica phase modified with a metal organic molecule. This paper reports the synthesis and characterization of an ordered mesoporous silica-metal organic (MSMO) composite material that has a high capacity for ammonia adsorption and enhanced hydrothermal stability over the metal organic framework alone. The silica phase of the composite material provides an engineered phase to enhance the hydrothermal stability of the composite, and the metal organic phase provides active sites for chemisorption. Characterization methods for the composite include N_2 adsorption isotherms, X-ray diffraction, X-ray photoelectron spectroscopy, thermogravimetric analysis, and scanning electron microscopy.

3.2 Experimental Methods

Materials

Tetramethylammonium hydroxide pentahydrate, (TMAOH, 97 %),tetramethylammonium silicate solution, (TMASi, 99.99 %, 15-20 wt % in water), sulfuric acid (95.0-98.0 %), and toluene (99 %) were purchased from Sigma Aldrich. Hexadecyltrimethylammonium chloride (CTAC, 25 % in water) was purchased from Pfaltz and Bauer. A solution of ammonium hydroxide (29 wt % in water), fumed silica (Cab-O-Sil M5), and ACS grade copper nitrate were purchased from Fisher Scientific. Benzene-1,3,5-tricarboxylic acid (BTC) and ACS grade ethanol were purchased

from Acros Organics.

MCM-41 synthesis

MCM-41 with a 37 Å pore was synthesized based on the procedure outlined by Glover et al.[21] The reaction gel was formed by mixing a solution of 2.4 g of 29 wt % ammonium hydroxide and 21.2 g of 29 wt % CTAC with a solution of 3.04 g of TMAOH and 20 g of 10 wt % solution of TMASi and then adding 4.5 g of Cab-O-Sil M5 fumed silica to the solution. After stirring for 30 minutes, the reaction gel was placed in a Teflon-lined autoclave and held at 80 °C in an oven for four days. Every 24 hours, the autoclave was removed from the oven and titrated to a pH of 10.0 using concentrated sulfuric acid, for a total of three titrations. At 24 hours after the third titration, the product was filtered and washed with distilled water to remove the remaining surfactant and allowed to dry at room temperature for 48 hours. The calcination procedure used to burn the surfactant from the MCM-41 involved heating the as-synthesized MCM-41 in air from room temperature to 540 °C at a rate of 1 °C/min and holding the sample at 540 °C for 10 hours.

Composite synthesis

To produce the copper nitrate-impregnated MCM-41 sample, 0.5 g MCM-41 and 0.16 g copper nitrate (corresponding to one Cu atom per 10 Si atoms) was stirred in an aqueous solution for 3 hours. After stirring, the sample was dried at 80 °C until dry. The sample was then heated in a tube furnace following the temperature schedule of the MCM-41 calcination procedure.

To incorporate the MOF phase, 0.21 g (1.0 mmol) of benzene-1,3,5-tricarboxylic acid was reacted with 0.1 g of copper-impregnated MCM-41 in a 60 ml mixed solution composed of equal parts by volume of water and ethanol. The mixture was placed in a Teflon-lined autoclave, and the reaction was held at 120 °C for 12 hours. Light green crystals were collected after decanting the mother liquid

and filtering the remaining mixture. The as-synthesized composite material was first dried in air and then placed in an oven at 120 °C overnight to obtain the final purple composite material. This same procedure was followed to synthesize a control sample, in which BTC was impregnated on base MCM-41 without copper impregnation.

Materials characterization

Textural characterization

Adsorption isotherms were measured at -196.1 °C using a Micromeritics ASAP 2020 with UHP nitrogen as the analysis gas. Prior to measurement, approximately 0.1 g of each sample was degassed for 8 hours with heating to 120 °C and vacuum to 10 μbar.

X-ray diffraction (XRD)

XRD spectra were used to confirm the long range structure of the MCM-41 and to confirm that the metal-impregnated samples also maintained the native MCM-41 structure. In addition, XRD was used to study the change of crystal structure before and after the samples were conditioned. The spectra were measured using a Scintag X1h/h automated powder diffractometer with Cu target, a Peltier-cooled solid-state detector, a zero background Si(5 1 0) support, and with a copper X-ray tube as the radiation source.

Thermogravimetric analysis (TGA)

TGA was used to determine the amount of organic phase impregnated within the MCM-41 material. The material was heated in a stream of zero air flowing at 10 mL/min at a ramp rate of 5 °C per minute to 700 °C and held at 700 °C for 2.5 hours.

Scanning electron microscopy (SEM)

SEM was used to visualize the microscopic properties of the materials. The images were collected using a Hitachi S4200 high resolution SEM equipped with a cold field

emission electron gun, digital imaging, and a thin-window energy dispersive X-ray spectrometer (EDS). Spectra were collected at 2 kV.

X-ray photoelectron spectroscopy

XPS was performed with a PHI Versaprobe XPS Microprobe analysis system manufactured by Physical Electronics, Inc. The apparatus was equipped with a monochromatic Al K(α) X-ray source (E=1486.6 eV). Survey spectra were collected over binding energies ranging from 1300 to 100 eV using a 1 eV energy step, 20 ms/step, with 10 cycles and 1 repeat/cycle. High resolution carbon spectra collected over binding energies ranging from 298 to 280 eV, and high resolution copper spectra collected between 957 and 927 eV. All high resolution spectra were analyzed using a 0.1 eV energy step, 50 ms/step, with 10 cycles and 3 repeats/cycle. Surface neutralization was accomplished using 1.1 eV electron neutralization and 10 eV argon ion neutralization. All spectra were analyzed using a take-off angle of 45°. The pass energy was set to 23.5 eV for determination of atomic ratios and binding energies were referenced to the oxygen 1s peak.[35] Deconvolution of peaks was accomplished using 70 % Gaussian-30 % Lorenzian curves with a linear background. All samples were analyzed after being crushed to a fine powder to expose the inner surface of MCM-41.

Hydrothermal conditioning

Hydrothermal stability for gas phase adsorbents is the simultaneous resistance to degradation at high temperatures and humidities. Various methods have been reported in the literature to study this property. The materials are often heated to a specified temperature while simultaneously passing steam over the sample.[12,22] Another accepted procedure is to place the sample in boiling water for a specified time period.[36,37] MOFs and other adsorbents are often tested for stability using the former technique, which allows for analysis of the crystallinity and porosity of the sample before its structure has fully degraded. In this way, it is possible to compare the hydrothermal stabilities of different materials under conditions that are just harsh

enough to show differences in the samples without fully degrading the structure.

Samples were conditioned at high temperature and humidity using the first conditioning method to test their hydrothermal stability. A hot plate was used to heat an Erlenmeyer flask filled with 150 mL of water to boiling. The samples were placed on filter paper and suspended above the boiling water. The samples were held at 85 °C in saturated water vapor for five hours to complete their conditioning. After conditioning, they were allowed to dry in air.

Ammonia capacity measurement

Equilibrium capacities for room temperature ammonia adsorption were measured for all samples using a breakthrough apparatus, a schematic of which is shown in Figure 3.1. The concentration of ammonia in dry helium fed to the adsorbent bed was kept constant at 1133 mg/m^3 (1500 ppm$_v$). Prior to analysis, all samples were regenerated under 10 μbar vacuum at 120 °C for 8 hours. The capacity of the adsorbent material, n (mol ammonia/kg adsorbent), was calculated from

$$n = \frac{F}{m} \int_0^\infty (c_0 - c)\, dt \tag{3.1}$$

where c_0 is the feed concentration in units of mol/m^3, and c is the effluent concentration at time t. The volumetric flow rate of gas through the adsorbent bed, F, was adjusted to yield a breakthrough time of approximately one hour. The mass of the sample, m, was approximately 10 mg and was contained in a small cylindrical adsorbent bed with an internal diameter of 4 mm.

Full breakthrough curves at low flow rates were measured using this apparatus, and the resulting capacities are equilibrium capacities. The accuracy of this method has been verified using a non-corrosive system. Capacities obtained by the full breakthrough method agree well with results obtained by standard gravimetric measurement using a Cahn balance.

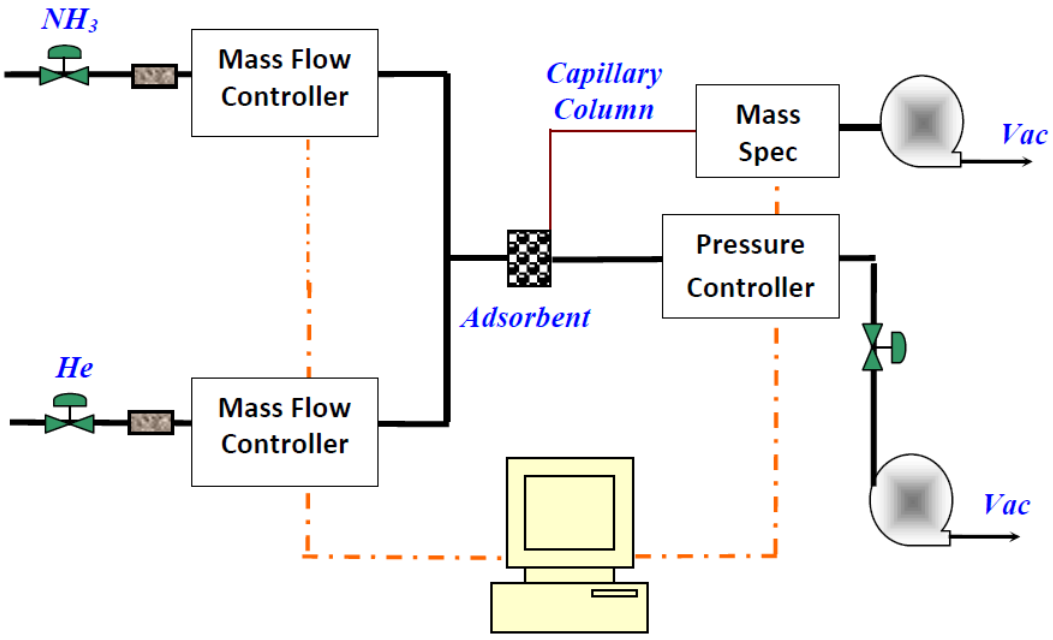

Figure 3.1 Schematic of breakthrough apparatus used to determine ammonia capacities.

3.3 Results and Discussion

Composite material characterization

Scanning electron microscope images, shown in Figure 3.2, provide detailed information about the morphology of the composite material. The composite contains amorphous structures that are similar in appearance to the MCM-41 SEM images and do not possess large amounts of the octahedral crystals commonly seen for CuBTC. As discussed below for other analytical techniques, the SEM images are consistent with the formation of a composite material that has copper sites dispersed throughout the ordered MCM-41 phase with BTC molecules bound to these copper sites. BTC is not largely associated with a crystalline CuBTC phase formed in bulk; rather, the composite material consists of an ordered MCM-41 phase with BTC bound to copper sites dispersed throughout the silica matrix. Figure 2(b) shows the presence of a crystalline impurity in the sample. As discussed below, only a small amount of this impurity is present, about 3 wt %, and it is CuBTC.

Figure 3.3 depicts the nitrogen adsorption isotherm at -196.1°C for the impregnated material. The isotherm is Type IV based on the IUPAC classification scheme and is typical of a mesoporous MCM-41 material. Hysteresis due to capillary condensation in the mesopores is evident in the desorption branch of the isotherm. Based on the isotherm, the addition of copper active sites and BTC linkages throughout the MCM-41 does not decrease the mesoporosity of the material. A comparison of the composite with the MCM-41 sample indicates that the composite material is similar in mesoporosity to the base MCM-41. Table 3.1 summarizes the physical properties of the composite, the base MCM-41, and CuBTC. The addition of the BTC bound to the Cu active sites throughout the material yields a slight decrease in pore volume and increase in surface area when compared to the base MCM-41. When compared to CuBTC, the composite material is 16 % lower in surface area. The surface areas of the MCM-41 and the composite material are more similar than that of CuBTC

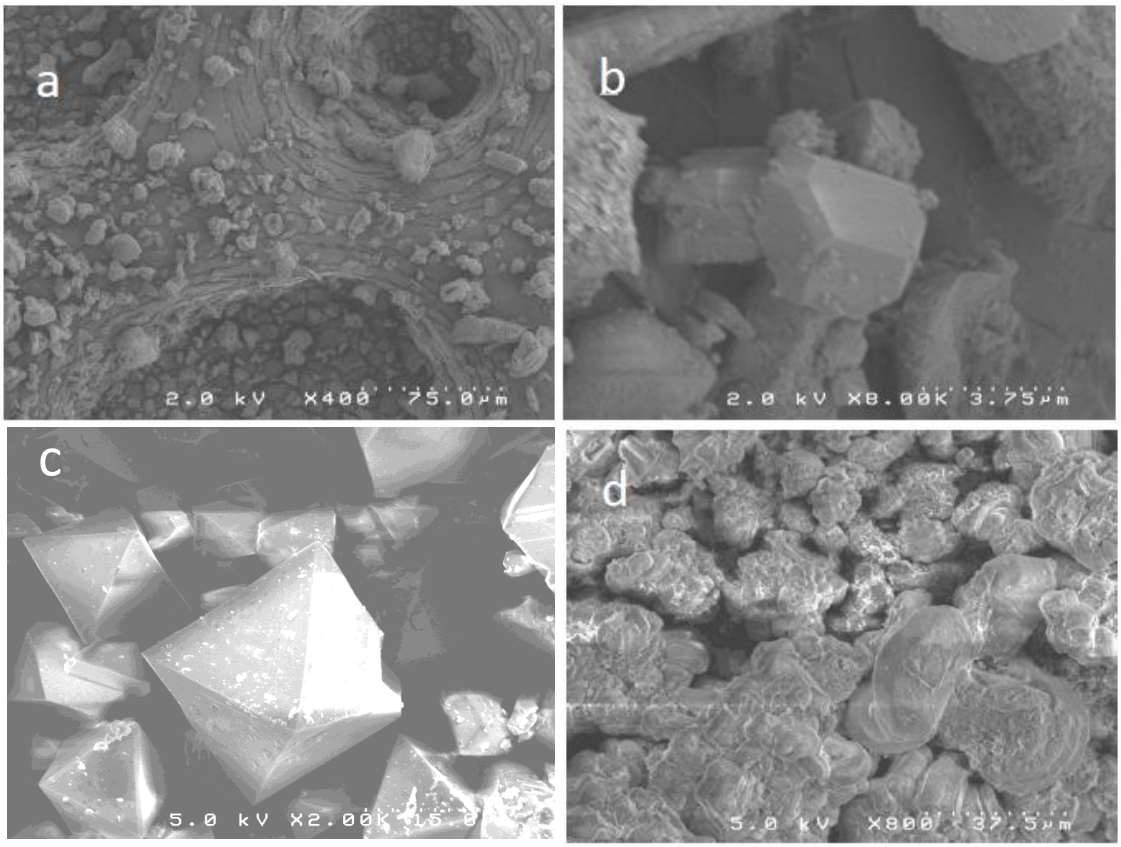

Figure 3.2 SEM images of (a) and (b) Cu-MCM-BTC, (c) CuBTC, and (d) MCM-41.

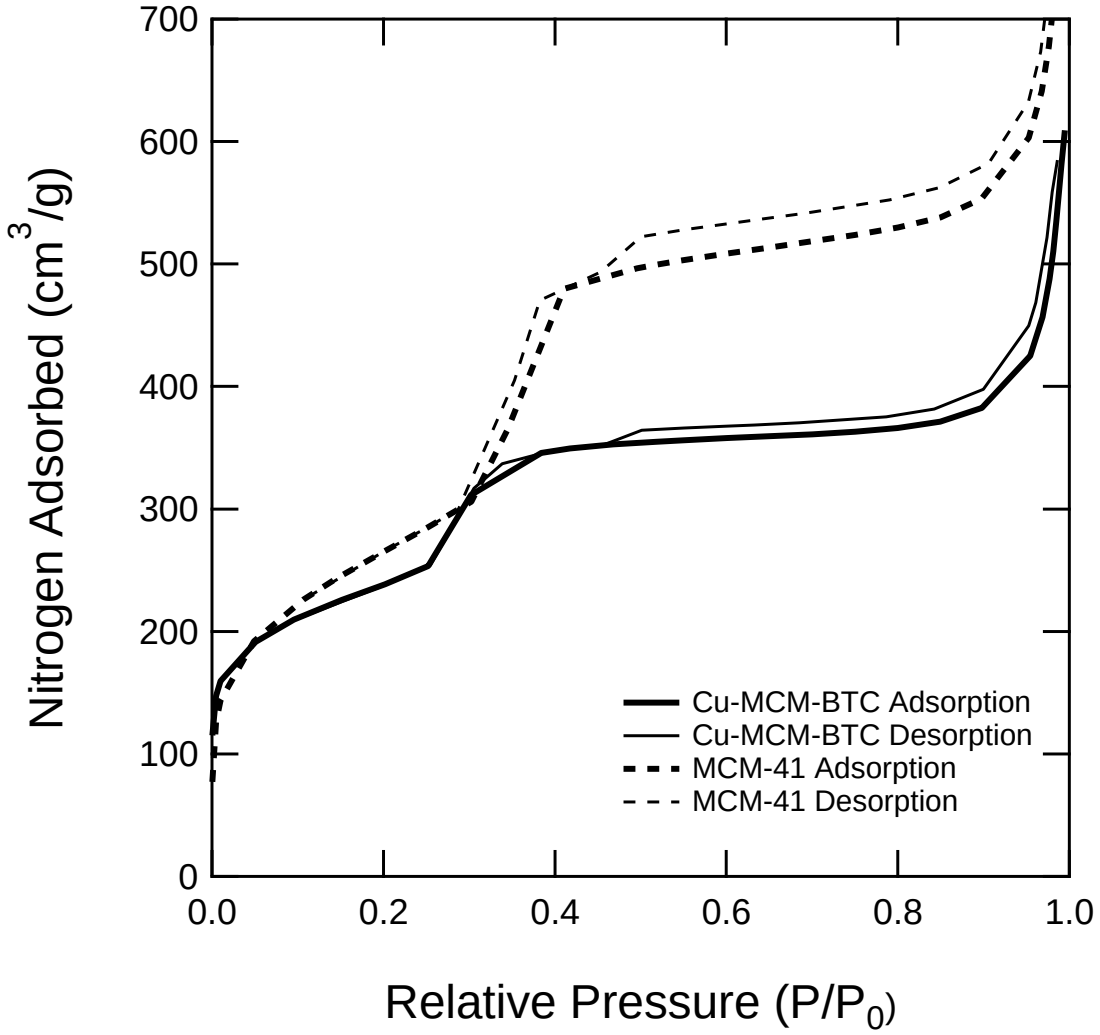

Figure 3.3 Comparison of the MCM-41 and 10 mol % Cu-MCM-BTC composite nitrogen isotherms at 77 K.

and the composite, which is consistent with the BTC molecule attaching to the Cu active sites on the MCM-41 with minimal formation of crystalline CuBTC.

Table 3.1: BET surface areas and pore volumes of MCM-41, CuBTC, and Cu-MCM-BTC.

Sample	BET Surface Area (m^2/g)	Total Pore Volume (cm^3/g)
CuBTC	1004	0.49
MCM-41	809	1.09
Cu-MCM-BTC	836	0.94

Figure 3.4 plots the heating profile and the weight loss of the composite material during heating using the TGA. The first step in the mass loss represents the removal of adsorbed water from the sample, and the second step represents loss of the organic BTC. Thermogravimetric analysis of the material shows a 12 % loading of the organic BTC within the copper-impregnated matrix. No copper or silica is lost during this heating step because the vapor pressures of these substances are low.[38] The base MCM-41 was impregnated with copper nitrate at a ratio of 1 Cu atom to 10 Si atoms. With the MCM-41 considered to be SiO_2, this translates to 7.6 wt % copper being distributed throughout the silica matrix. This corresponds to a 2:1 Cu to BTC ratio, which is different from that of the CuBTC MOF, which has a 3:2 Cu to BTC ratio. Thus BTC binds to copper sites distributed throughout the silica matrix and does not form large quantities of crystalline CuBTC.

TGA was also performed on a control sample synthesized using BTC and MCM-41 without impregnated copper sites. This material was synthesized to verify that copper active sites are necessary to retain the BTC by bonding with the carboxylic acid groups on the organic molecule. TGA of this control sample showed only water loss and no removal of BTC from the sample, indicating that no BTC remained on the silica support after synthesis. Thus, it is evident that copper sites distributed throughout the MCM-41 matrix are necessary to retain the BTC in the composite

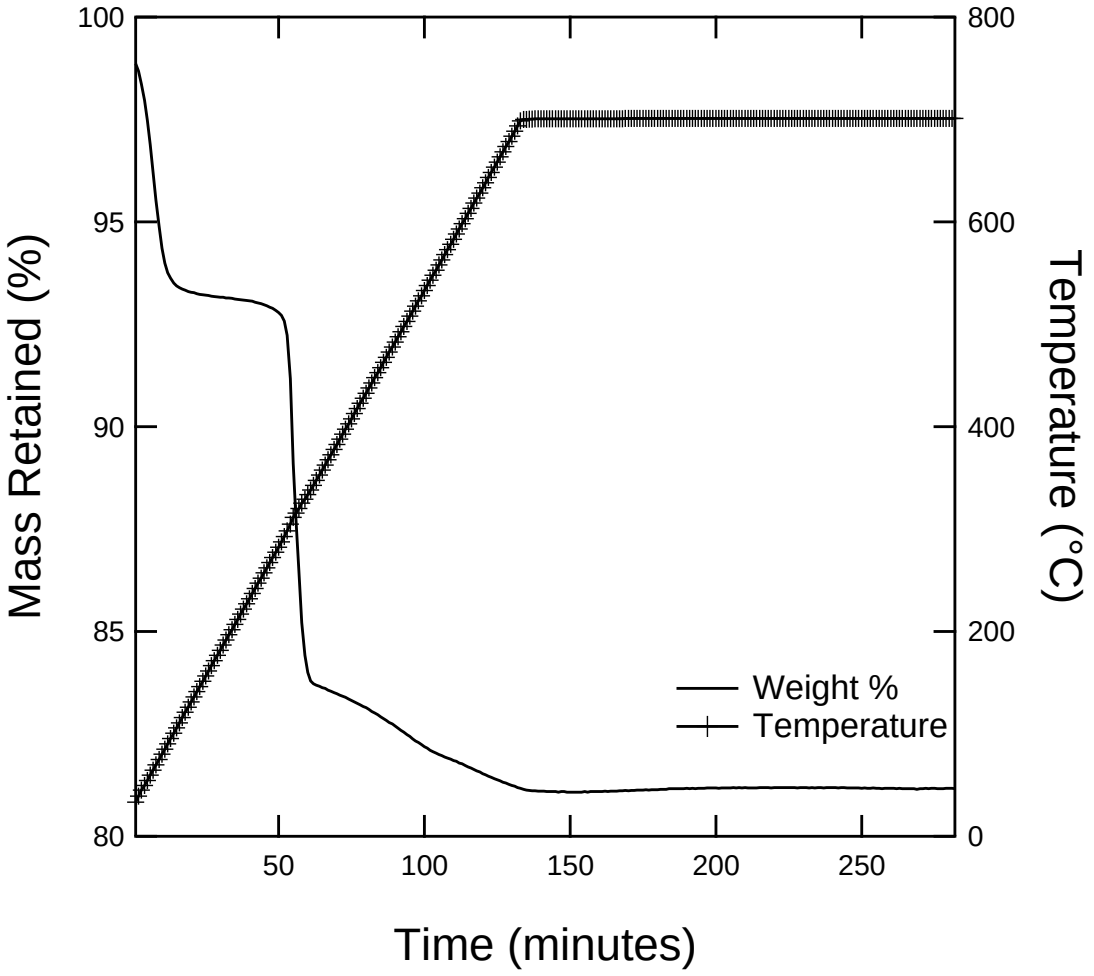

Figure 3.4 TGA heating procedure and mass loss of the Cu-MCM-BTC composite.

because the copper sites bond with oxygen atoms available on BTC. Because the composite material has well dispersed copper sites and does not form large amounts of crystalline CuBTC, not all carboxylic acid groups on each BTC are bound to copper sites; consequently, in addition to having copper sites available for chemisorption, the composite material contains free carboxylic acid groups that are available for coordination.[39]

Powder X-ray diffraction was used to characterize the effect of the copper and BTC impregnation on the structure of the MCM-41 matrix. Figure 3.5 compares the XRD spectra of the base MCM-41 material, the copper impregnated MCM-41, and the composite material. A high degree of MCM-41 structural ordering is indicated by the four discrete sharp peaks in the low angle spectrum for all three samples.[40] The decrease in intensity of peaks in the spectrum of the composite material can be attributed to scattering by the BTC.[41–43] The d_{100} peak is shifted to a lower angle and broadened slightly in the spectrum of the composite material. This shift represents an expansion of the MCM-41 lattice after incorporation of BTC into the pores of the Cu-MCM-41, as has been shown previously.[44]

XRD scans in the higher 2θ range were also performed to characterize the structure of the composite material. As shown in Figure 3.6, the XRD spectrum of the composite exhibits peaks representing a crystalline material similar to that of the CuBTC crystals. The peaks present in the composite scan have lower intensities than those of CuBTC. Some of the peaks in the higher 2θ region are eclipsed by background noise. The peaks of the composite scan that correspond to CuBTC peaks are a result of the formation of CuBTC impurities formed during synthesis of the composite material. Because there is a small concentration of CuBTC within the amorphous BTC-impregnated composite, the CuBTC peaks are of lower intensity, but still visible, on the long range XRD scan. The composite spectrum also shows a broad MCM-41 peak located between 20 and 30°. Coupled with the SEM information,

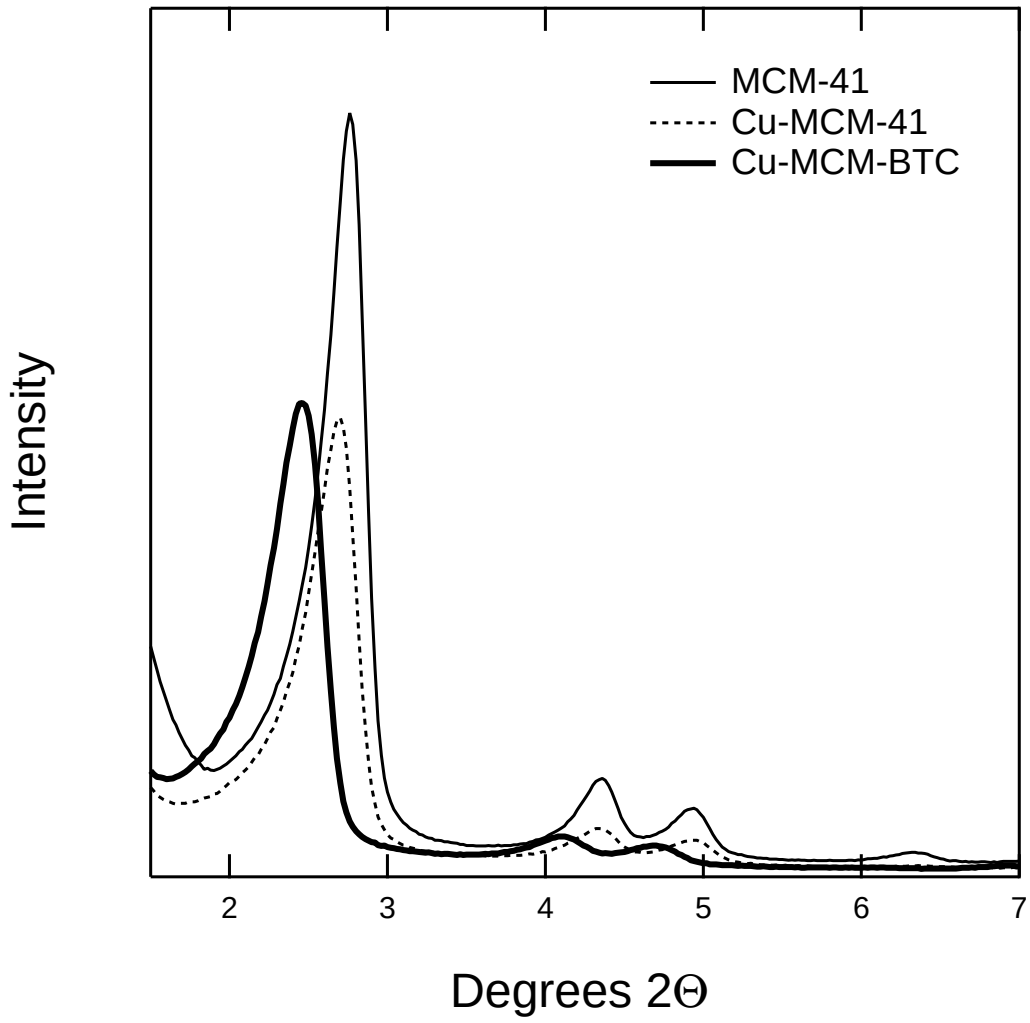

Figure 3.5 Small angle XRD scans of MCM-41, Cu-MCM-41, and Cu-MCM-BTC.

which depicted the formation of CuBTC impurities within the composite, XRD shows that there are some CuBTC crystals formed from only a small mass fraction of the material. However, this CuBTC formation is not representative of the entire material and is an impurity.

Mixtures of CuBTC and 10 mol % Cu-MCM-41 were analyzed via XRD to estimate the amount of CuBTC impurity present in the composite material following the procedure of Kontoyannis and Vagenas.[45] For all standards, the ratio of the peak intensities at 2.8 and 9.9° 2θ was examined, which correspond to the MCM-41 100 peak and a CuBTC peak. The ratio of three standards were plotted versus the weight percentage of one compound in the mixture, as seen in Figure 3.7. In the resulting equation of best fit,

$$y = 0.538x - 18.8 \tag{3.2}$$

the parameter y represents the ratio of the peak intensities and x is the weight percentage of Cu-MCM-41 present in the mixture. From this calibration curve, the composite material was determined to have 3.3 wt % CuBTC impurity.

XPS was used to investigate the bonding of the organic phase in the composite material. Copper has been shown to fully disperse throughout the silica matrix using an impregnation technique similar to the one used in this research.[46] High resolution XPS scans were used to investigate the bonds occurring between the well dispersed copper sites and BTC. Figure 3.8 shows high resolution XPS scans in the carbon region, which show that carbon exists in two forms in CuBTC. The peak at 284.7 eV could represent carbons in the benzene ring of BTC or interstitial carbon from -CH_2 groups. An interstitial carbon peak would be present in XPS analysis of other samples analyzed via XPS, including MCM-41. Since this carbon peak is not present in the base MCM-41 material, it is evident that the peak at 284.7 eV represents carbons in the benzene ring of BTC. The separate 1s peak at 289.3 eV represents carbons in the carboxylic acid groups of BTC.[35] Analysis of the carbon region in the

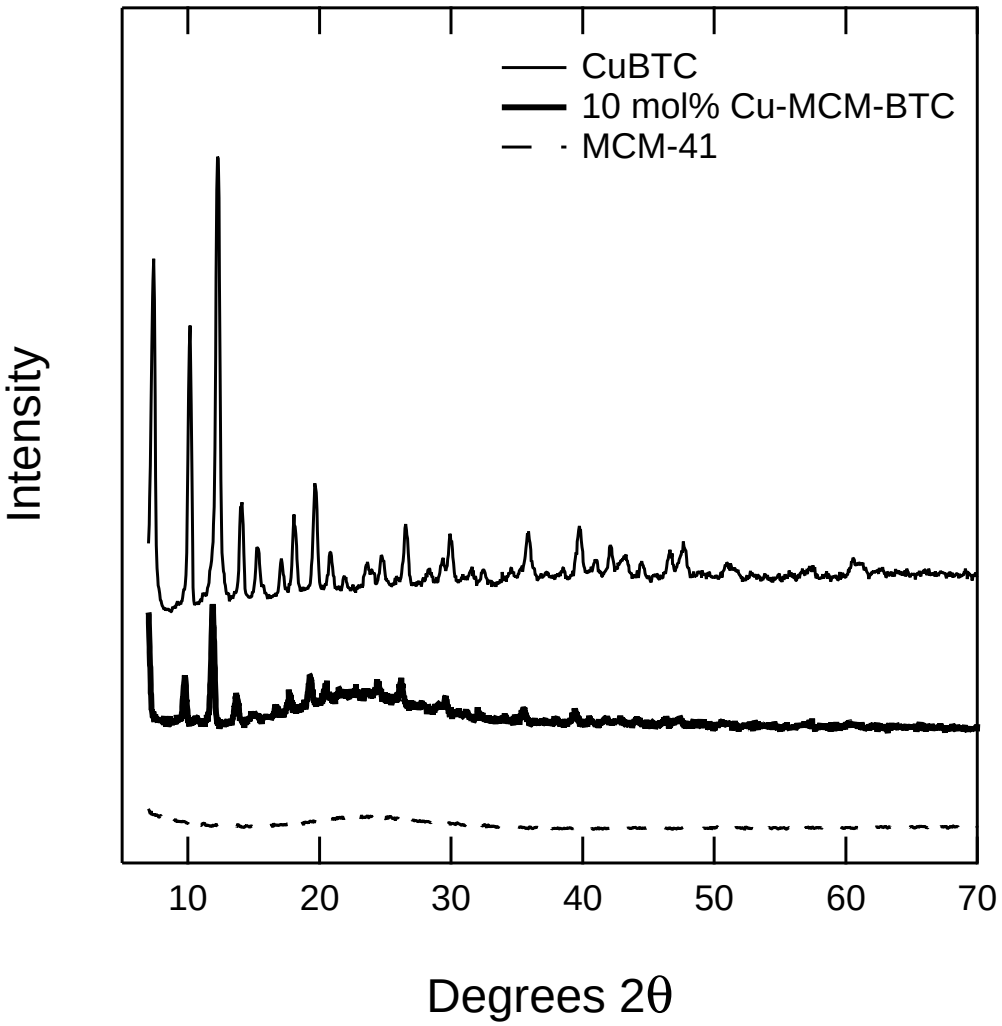

Figure 3.6 Powder XRD results for MCM-41, CuBTC, and the Cu-MCM-BTC composite. Curves are offset.

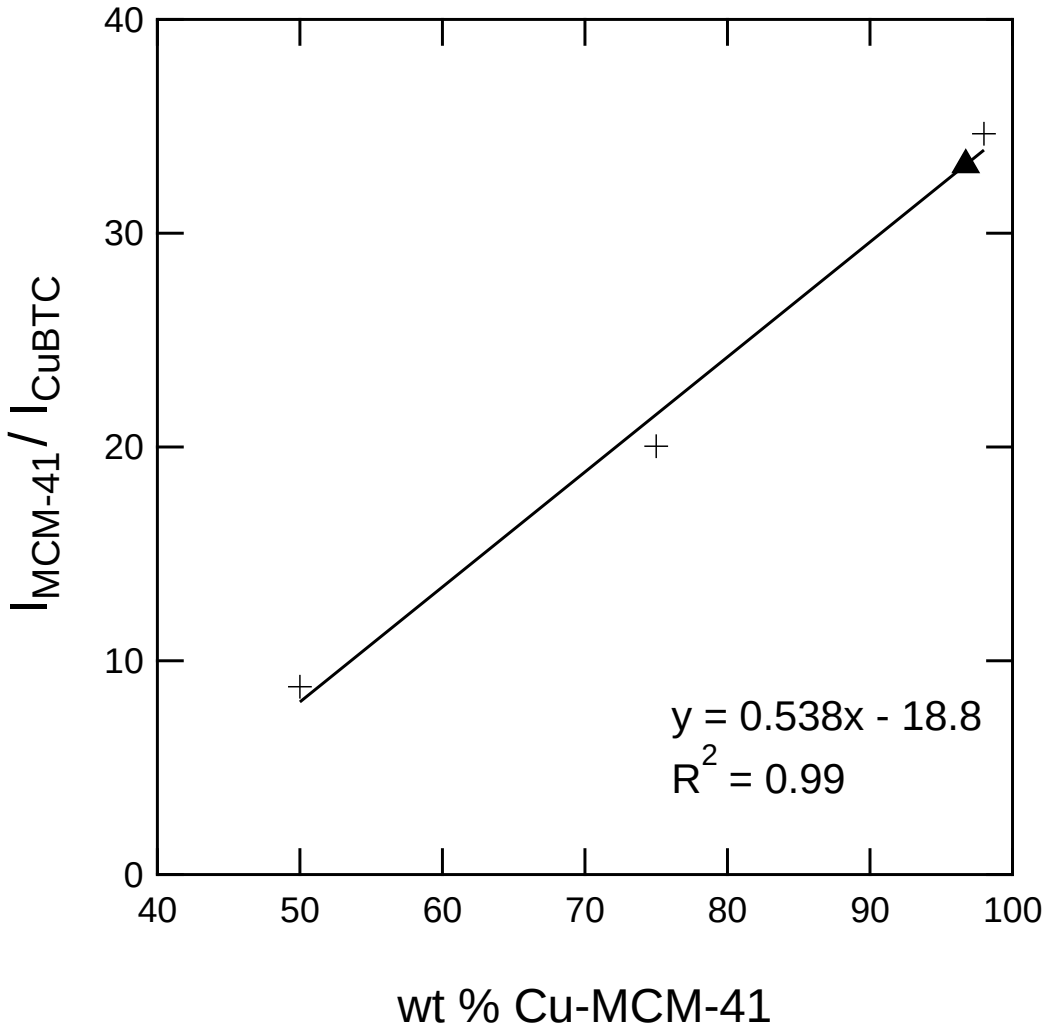

Figure 3.7 Ratio of XRD peak intensities for mixtures of CuBTC and 10 mol % Cu-MCM-41.

composite's spectrum shows a similar occurrence of the two peaks. Since all carbon atoms in the composite material are derived from the BTC and the carbon peaks in the spectra of both materials occur at the same binding energies, it is evident that the BTC molecule remains intact after synthesis of the composite. High resolution scans of the copper peaks in both samples also yield peaks that occur at the same binding energies as shown in Figure 3.9. From this, we can conclude that copper in the composite material is bound to oxygen atoms from BTC in a similar way to the complexation of copper that occurs in CuBTC. However, according to the XRD and TGA results, the Cu to BTC ratio in the composite is different from that in the CuBTC. Consequently, except for BTC in the 3 wt % CuBTC impurity, the BTC molecules are bound to copper sites distributed throughout the ordered silica phase.

Hydrothermal conditioning

From the SEM images in Figure 3.10, it is clear that the Cu-MCM-BTC sample did not change its morphology after conditioning, whereas the CuBTC degraded from octahedral crystals with sharp edges to irregularly-shaped masses. The change in morphology of CuBTC indicates that the pore structure collapsed during conditioning. There are no visible differences between SEM images for the composite material and the MCM-41 base material before and after conditioning.

This explanation can be verified using X-ray diffraction, profiles of which are shown in Figure 3.11. In the XRD patterns for CuBTC, the spectrum of the conditioned material shows a decrease in peak intensity and a slight shift in the larger peaks when compared to the spectrum of virgin CuBTC. Coupled with the SEM images, the shift in the spectrum and its degradation is indicative of decomposition of the CuBTC structure. The conditioned Cu-MCM-BTC spectrum is similar to that of the conditioned CuBTC, suggesting that the small amount of CuBTC impurity located within the Cu-MCM-BTC composite material degraded during the conditioning procedure.

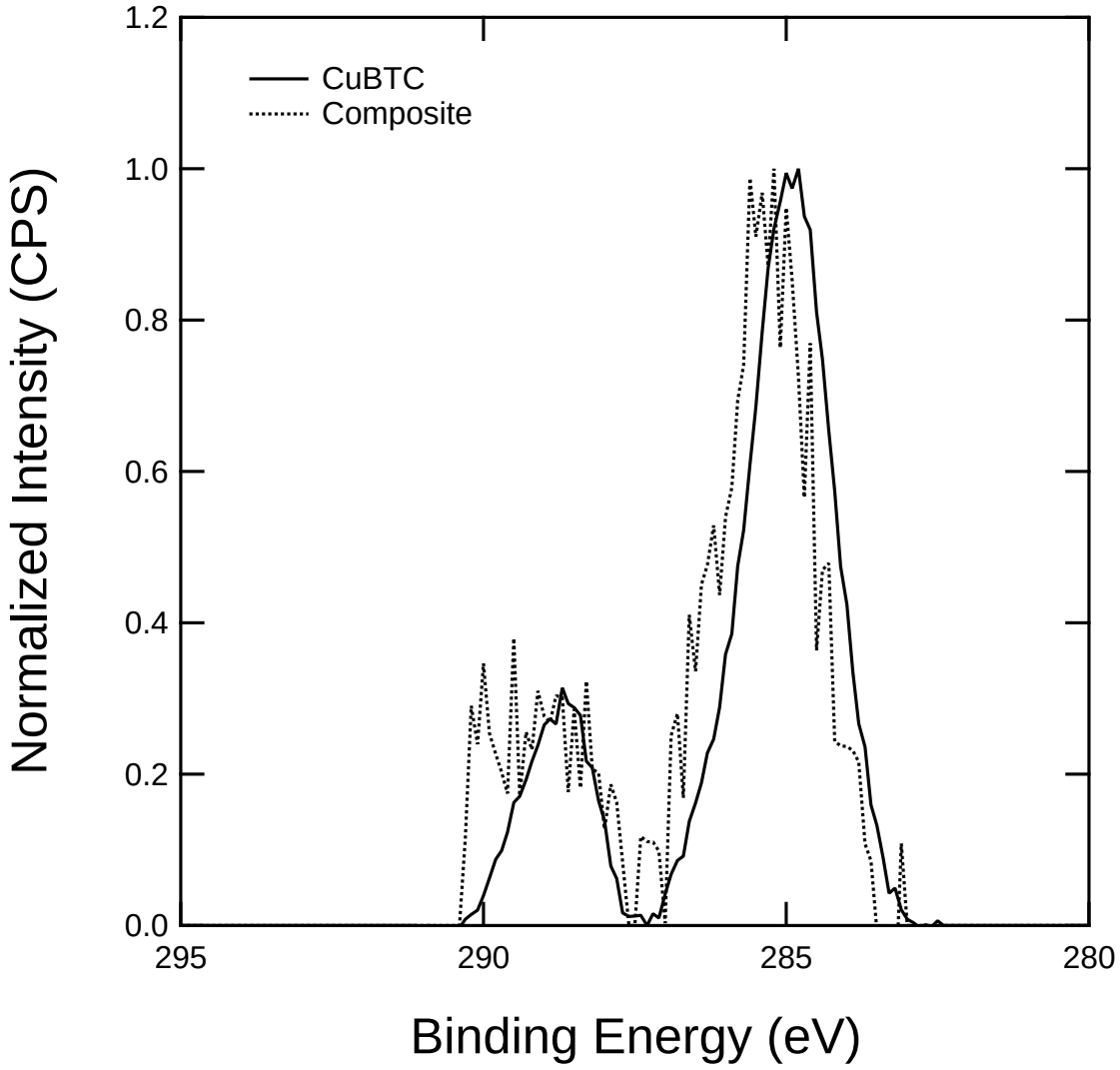

Figure 3.8 High resolution XPS spectra in the carbon region for CuBTC and the composite.

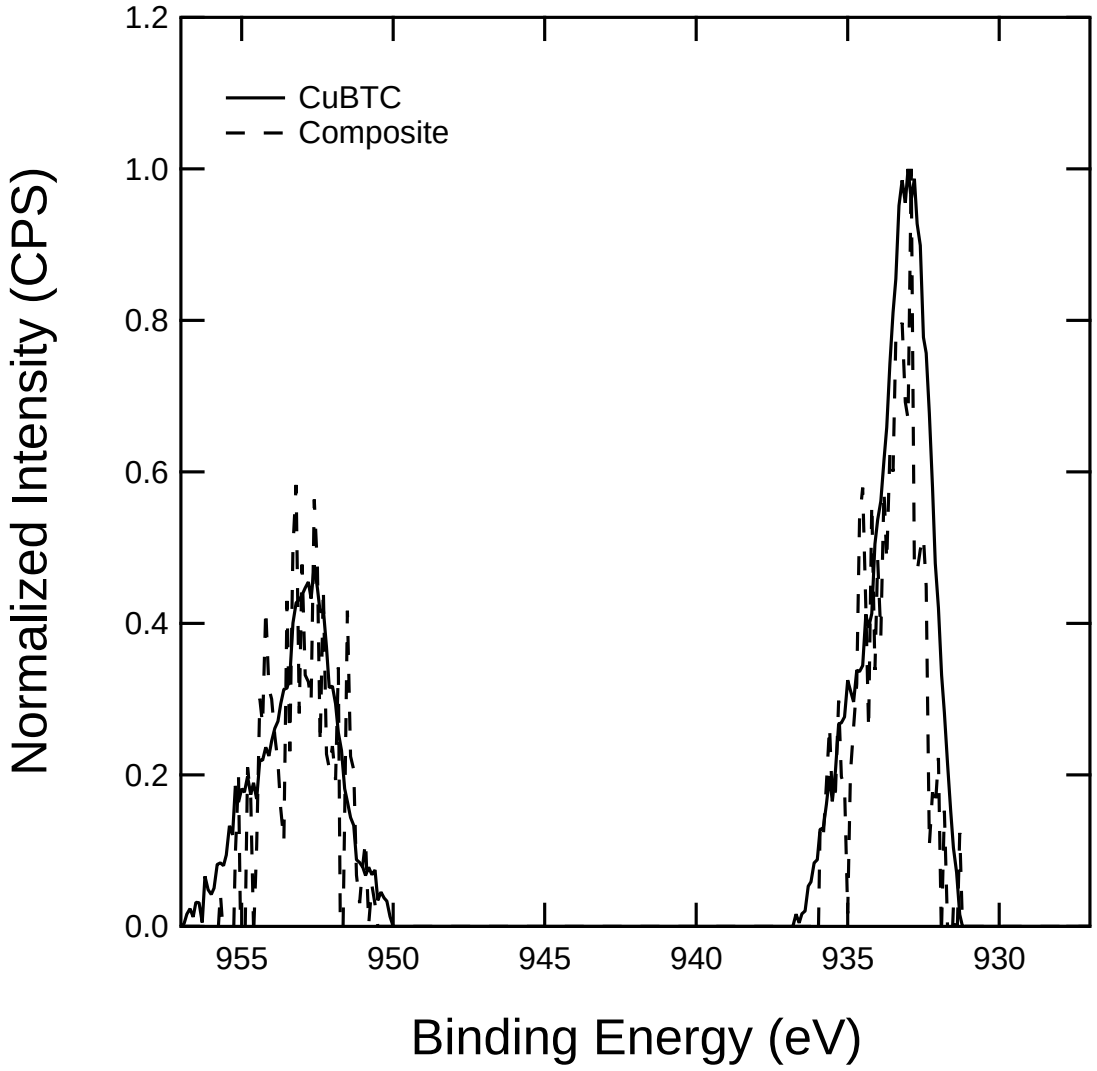

Figure 3.9 High resolution XPS spectra in the copper region for CuBTC and the composite.

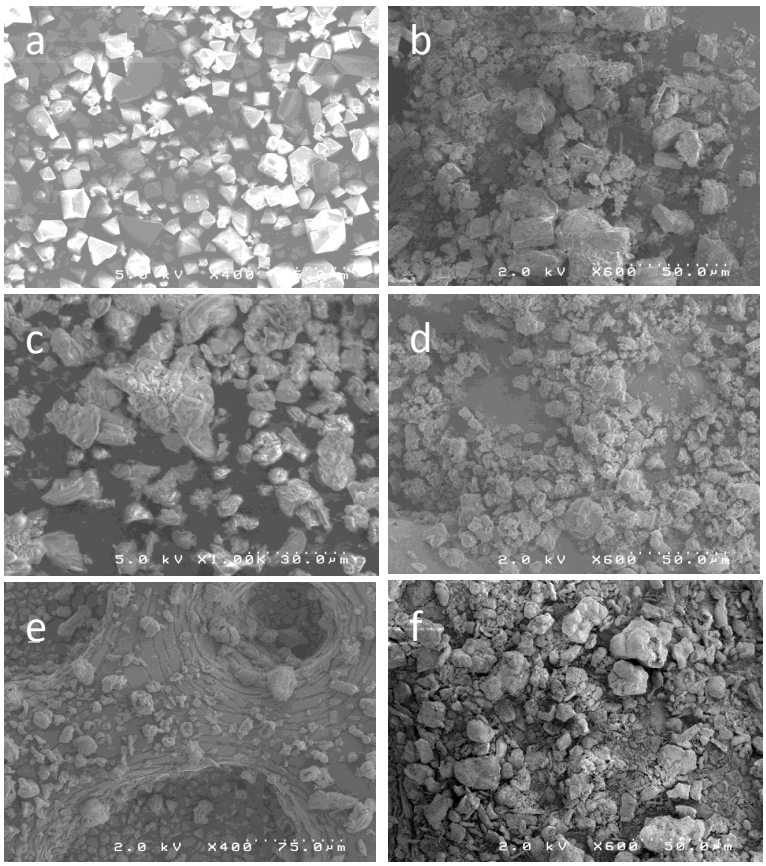

Figure 3.10 SEM images of the samples before and after conditioning for 5 hours (a) CuBTC, (b) conditioned CuBTC, (c) MCM-41, (d) conditioned MCM-41, (e) Cu-MCM-BTC, (f) conditioned Cu-MCM-BTC.

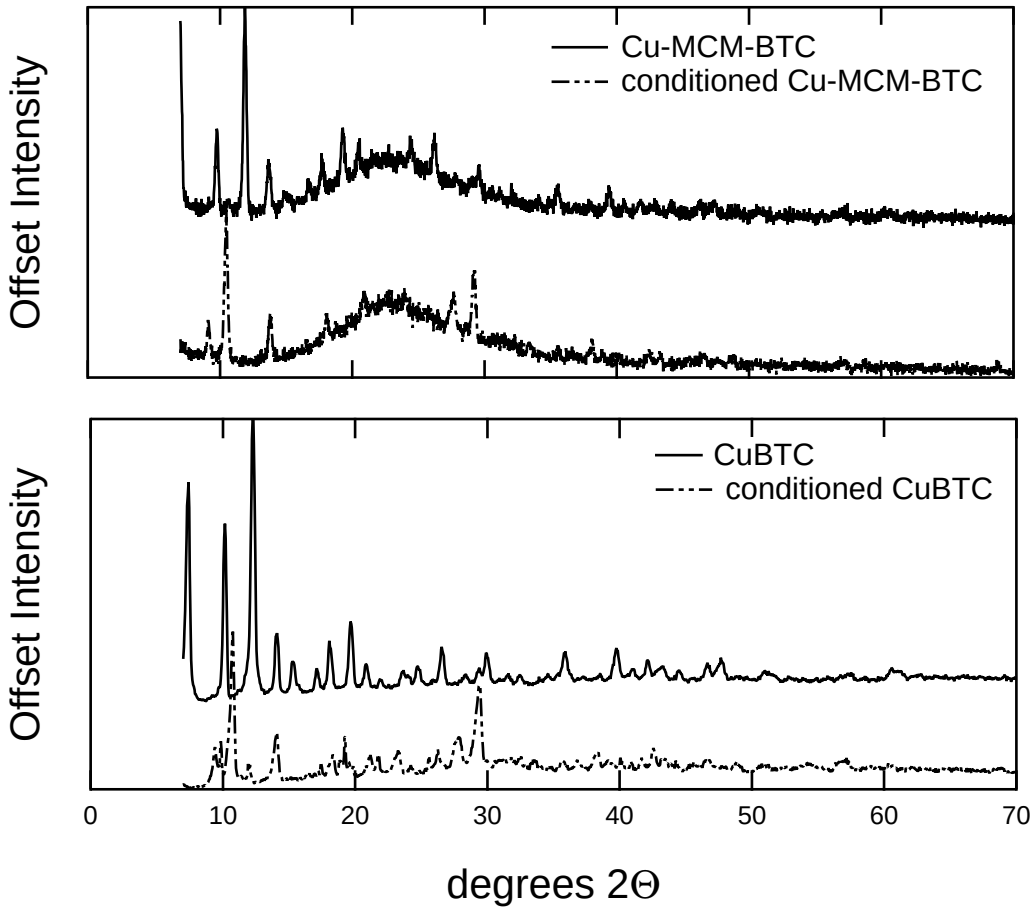

Figure 3.11 Comparison of XRD spectra before and after conditioning for CuBTC and Cu-MCM-BTC.

The small angle X-ray diffraction spectra of the conditioned Cu-MCM-BTC composite and conditioned MCM-41 samples, shown in Figure 3.12, indicate that both the composite and the base MCM-41 materials do not lose their hexagonal MCM-41 order during the conditioning process. Consequently, the powder XRD profiles show that the composite remains structurally ordered after conditioning, similar to the base MCM-41 material.

High resolution XPS spectra of the carbon atoms in the conditioned sample confirm the presence of BTC after conditioning. The same carbon peaks are present in the composite spectrum before and after conditioning. The peaks at 284 and 289 eV represent carbons in the benzene ring and the carboxylic acid groups of the organic molecule. The presence of these peaks in the spectrum indicates that BTC remains intact after conditioning.

Ammonia adsorption

The Cu-MCM-BTC composite is a novel adsorbent material with a high ammonia capacity, as shown in Table 3.2. The ammonia capacities measured using the breakthrough apparatus have standard deviations on the order of 3 %. The initial ammonia capacity for the composite is 61 % higher than that of MCM-41 and 46 % lower than that of CuBTC. The adsorbents show a step-wise increase in ammonia capacity upon addition of the BTC impregnant within the MCM-41. Base MCM-41 begins with an ammonia capacity of 2.0 mol/kg and increases to 5.2 mol/kg after functionalization with copper and BTC. The ammonia capacity of the composite material is approximately 30 times that of a common commercial carbon, BPL activated carbon (0.16 mol/kg) and more than three times that of a common zeolite, 13X molecular sieve (1.5 mol/kg), under comparable breakthrough test conditions.

As shown in the table, the ammonia capacity of the base MCM-41 increased 41 % after conditioning. As part of its synthesis procedure, MCM-41 is calcined at a high temperature to remove excess surfactant from its pores. This calcination

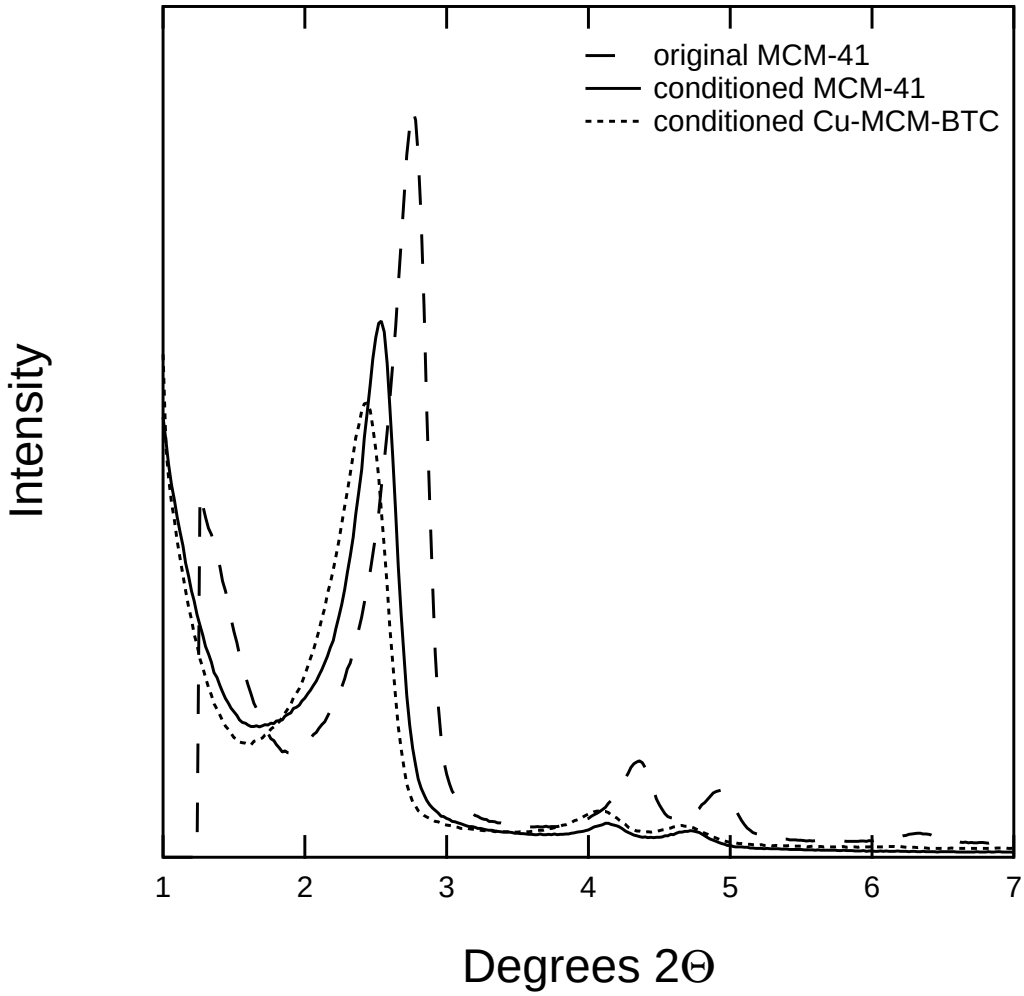

Figure 3.12 XRD spectra for conditioned MCM-41 and conditioned Cu-MCM-BTC.

Table 3.2: Ammonia capacities before and after conditioning for MCM-41, CuBTC, and Cu-MCM-BTC.

	Ammonia Capacity (mol/kg)	
Sample	Initial	Conditioned
CuBTC	9.6	1.5
MCM-41	2.0	3.4
Cu-MCM-BTC	5.2	4.3

process also strips the silica matrix of hydroxyl groups on the walls of the MCM-41. The conditioning process allows hydroxyl groups to re-form at these sites and remain after the sample is regenerated.[24] These additional hydroxyl groups increase the acidity of the MCM-41, which results in an increase in ammonia capacity for the conditioned sample. Consequently, the base MCM-41 shows an increase in ammonia capacity after conditioning, which is believed to be caused by the extra hydroxyl groups formed on the silica matrix during the hydrothermal treatment.

Despite having a lower ammonia capacity than CuBTC, after conditioning in saturated water vapor for 5 hours the composite material maintains its structural stability and shows an ammonia capacity decrease of only 16 %. Comparatively, the ammonia capacity of the CuBTC sample decreased 84 % upon conditioning. The enhanced stability of the composite material, when compared to CuBTC, is due to the presence of the silica matrix. The degradation of the crystalline CuBTC impurity in the composite material upon conditioning is partially responsible for the observed decrease in ammonia capacity. The composite did lose ammonia capacity after steam conditioning. We can assume that the CuBTC impurity in the composite has the same decrease in the ammonia capacity after conditioning as the pure CuBTC MOF. If we treat the metal-organic phase and MCM-41 separately and assume that the MCM-41 in our composite has the same ammonia capacity as the pure MCM-41 after conditioning, a material balance calculation shows that the ammonia capacity for the

metal-organic phase decreased about 50 % after conditioning. However, if we treat the metal-organic phase and MCM-41 as an entity and presume that the MCM-41 may not behave in the composite exactly as it does by itself because of more limited access to its surface, then the material balance indicates that the composite loses only 13 % of its ammonia capacity after conditioning. This result, coupled with the XRD results, indicates that the composite has a higher stability compared to CuBTC, which lost about 84 % of its ammonia capacity after conditioning due to the loss of its porosity[13] and collapse of its structure.

The composite material has four types of active sites available for ammonia adsorption. First, the base silica matrix provides ammonia capacity.[18,19,46] Second, the addition of hydroxyl groups to the silica surface from exposure to humid air, steam, or liquid water enhances the ammonia capacity; the composite is synthesized using a liquid solvent of water and ethanol, and all materials are steamed for hydrothermal conditioning. Third, the copper sites distributed throughout the matrix provide additional sites for ammonia to form diammine-copper complexes.[27,46] Finally, carboxylic acid groups on the organic molecule provide coordination sites for the ammonia.[25,47]

The retention of the structure of the composite material and minimal decrease in ammonia capacity after conditioning are indicative of hydrothermal stability. In contrast, the degradation of the CuBTC structure and decrease in ammonia capacity upon conditioning is indicative of low hydrothermal stability.

3.4 Conclusions

A new composite material has been synthesized and characterized by combining an ordered mesoporous silica phase, specifically MCM-41 impregnated with copper and benzene-1,3,5-tricarboxylic acid, the organic BTC linker used in the synthesis of a common MOF, to give an ordered mesoporous silica – metal organic (MSMO) composite material. The nitrogen isotherm confirms the formation of the mesoporous

composite material. According to TGA results, approximately 12 % organic BTC is loaded onto the MCM-41 and bound to the copper sites dispersed throughout MCM-41. X-ray diffraction results confirm that the composite does not lose its long range MCM-41 order after impregnation with the BTC. It also confirms that small amounts of CuBTC crystals (about 3 wt %) are present in the final sample as an impurity. SEM images confirm this observation. XPS shows that copper sites that are distributed throughout the MCM-41 matrix are actively bound to BTC. The presence of both copper sites and intact BTC result in an ammonia capacity that is higher than the base ordered mesoporous silica (5.2 mol/kg compared to 2.0 mol/kg) due to the functionality provided by the metal organic phase.

After hydrothermal conditioning, the novel composite material maintains its high ammonia capacity, whereas the corresponding metal organic framework sample degrades, resulting in a large decrease in ammonia capacity. XPS shows that the BTC present in the composite material remains intact after conditioning. XRD shows that the MCM-41 structure is also maintained. These results show that the new composite material provides both the high ammonia capacity associated with MOF materials and the hydrothermal stability associated with the silica phase, and is a promising candidate for ammonia removal applications.

References

[1] V. Ravat, D. B. Mantri, P. Selvam, P. Aghalayam. Platinum group metals substituted MCM-41 molecular sieves: Synthesis, characterization and application as novel catalysts for the reduction of NO by CO. *J. Mol. Catal. A: Chem.*, 2009, **314**, 49-54.

[2] C. Chanquia, K. Sapag, E. Rodriguez-Castellon, E. Herrero, G. Eimer. Nature and location of copper nanospecies in mesoporous molecular sieves. *J. Phys. Chem. C*, 2010, **114**, 1481-1490.

[3] D. Lensveld, J. Mesu, A. van Dillen, K. de Jong. Synthesis and characterization of MCM-41 supported nickel oxide catalysts. *Microporous Mesoporous Mater.*, 2001, **44-45**, 401-407.

[4] R. Savidha, A. Pandurangan. Vapour phase isopropylation of phenol over zinc- and iron-containing Al-MCM-41 molecular sieves. *Appl. Catal., A*, 2004, **262**, 1-11.

[5] D. A. Sheppard, C. E. Buckley. Hydrogen adsorption on porous silica. *Int. J. Hydrogen Energy*, 2008, **33**, 1688-1692.

[6] A. Vinu, K. Nandhini, V. Murugesan, W. Bohlmann, V. Umamaheswarl, A. Poppl, M. Hartmann. Mesoporous FeAlMCM-41: an improved catalyst for the vapor phase tert-butylation of phenol. *Appl. Catal., A*, 2004, **265**, 1-10.

[7] C. Wu, Q. Gao, J. Hu, Z. Chen, W. Shi. Rapid preparation, characterization and hydrogen storage properties of pure and metal ions doped mesoporous MCM-41. *Microporous Mesoporous Mater.*, 2009, **117**, 165-169.

[8] A. Gervasini, C. Messi, P. Carniti, A. Ponti, N. Ravasio, F. Zaccheria. Insight into the properties of Fe oxide present in high concentrations on mesoporous silica. *J. Catal.*, 2009, **262**, 224-234.

[9] D. Britt, H. Furukawa, B Wang , T.G. Glover, O.M. Yaghi. Highly efficient separation of carbon dioxide by a metal organic framework replete with open metal sites. *Proc. Natl. Acad. Sci. U. S. A.*, 2009, **106**, 20637-20640.

[10] N. L. Rosi, J. Eckert, M. Eddaoudi, D. T. Vodak, J. Kim, M. O'Keeffe, O. M. Yaghi. Hydrogen storage in microporous metal organic frameworks. *Science*, 2003, **300**, 1127-1129.

[11] D. Britt, D. Tranchemontagne, O. M. Yaghi. Metal organic frameworks with high capacity and selectivity for harmful gases. *Proc. Natl. Acad. Sci. U. S. A.*, 2008, **33**, 11623-11627.

[12] J. J. Low, A. I. Benin, P. Jakubczak, J. F. Abrahamian, S. A. Faheem, R. R. Willis. Virtual high throughput screening confirmed experimentally: Porous coordination polymer hydration. *JACS*, 2009, **131**, 15834–15842.

[13] J. Liu, Y. Wang, A. I. Benin, P. Jakubczak, R. R. Willis, M. D. LeVan. CO2/H2O adsorption equilibrium and rates on metal-organic frameworks: HKUST-1 and Ni/DOBDC. *Langmuir*, 2010, **26**, 14301-14307.

[14] L Grajciar, O. Bludsky, P. Nachtigall. Water adsorption on coordinatively unsaturated sites in CuBTC MOF. *J. Phys. Chem. Lett.*, 2010, **1**, 3354-3359.

[15] P. Kusgens, M. Rose, I. Senkovska, H. Frode, A. Henschel, S. Siegle, S. Kaskel. Characterization of metal-organic frameworks by water adsorption. *Microporous Mesoporous Mater.*, 2009, **120**, 325-330.

[16] C. T. Kresge; M. E. Leonowicz; W. J. Roth; J. C. Vartuli; J. S. Beck. Ordered mesoporous molecular sieves synthesized by a liquid crystal template mechanism *Nature*, 1992, **359**, 710-712.

[17] F. Hoffmann, M. Cornelius, J. Morell, M. Froba. Silica-based mesoporous organic-inorganic hybrid materials. *Angew. Chem. Int. Ed.*, 2006, **45**, 3216-3251.

[18] B. A. Morrow, I. A. Cody. Infrared studies of reactions on oxide surfaces. 6. Active sites on dehydroxylated silica for the chemisorption of ammonia and water. *J. Phys. Chem.*, 1976, **80**, 1998-2004.

[19] B. A. Morrow, I. A. Cody, L. S. M. Lee. Infrared studies of reactions on oxide surfaces. IV. The structure of chemisorbed ammonia on silica. *J. Phys. Chem.*, 1975, **79**, 2405-2408.

[20] N. Chino, T. Okubo. Nitridation mechanism of mesoporous silica: SBA-15. *Microporous Mesoporous Mater.*, 2005, **87**, 15-22.

[21] T. G. Glover, K. I. Dunne, R. J. Davis, M. D. LeVan. Carbon-silica composite adsorbent: Characterization and adsorption of light gases. *Microporous Mesoporous Mater.*, 2008, **111**, 1-11.

[22] J. M. Kim, J. H. Kwak, S. Jun, R. Ryoo. Ion exchange and thermal stability of MCM-41. *J. Phys. Chem.*, 1995, **99**, 16742-16747.

[23] S. Shen, S. Kawi. MCM-41 with improved hydrothermal stability: Formation and prevention of Al content dependent structural defects. *Langmuir*, 2002, **18**, 4720-4728.

[24] T. Linssen, K. Cassiers, P. Cool, E.F. Vansant. Mesoporous templated silicates: an overview of their synthesis, catalytic activation and evaluation of the stability. *Adv. Colloid Interface Sci.*, 2003, **103**, 121-147.

[25] C. Petit, T. Bandosz. MOF-graphite oxide nanocomposites: surface characterization and evaluation as adsorbents of ammonia. *J. Mater. Chem.*, 2009, **19**, 6521-6528.

[26] C. Petit, T. Bandosz. MOF-GO Composites: combining the uniqueness of graphene layers and MOFs. *Adv. Funct. Mater.*, 2009, **21**, 4753-4757.

[27] C. Petit, T. Bandosz. Enhanced ddsorption of ammonia on MOF/GO composites: analysis of surface interactions. *Adv. Funct. Mater.*, 2010, **20**, 111-118.

[28] C. Petit, B. Mendoza, T. Bandosz. Reactive adsorption of ammonia on copper-based MOF/graphene composites. *Langmuir*, 2010, **26**, 15302-15309.

[29] S. J. Yang, J. Y. Choi, H. K.Chae, J. H. Cho, K. S. Nahm, C. R. Park. Preparation and enhanced hydrostability and hydrogen storage capacity of CNT/MOF-5 hybrid composite. *Chem. Mater.*, 2009, **21**, 1893-1897.

[30] B. Liu, H. Shioyama, H. Jiang, X. Zhang, Q. Xu. Metal organic framework (MOF) as a template for syntheses of nanoporous carbons as electrode materials for supercapacitor. *Carbon*, 2010, **48**, 456-463.

[31] G. Hundal, Y. K. Hwang, J. S. Chang. Formation of nanoporous and non-porous organic-inorganic hybrid materials incorporating a-Keggin phosphotungstate anion: X-ray crystal structure of a 3D polymeric complex [(Na6(C9H5O6)3(H2O)15)(PW12O40)]1 with a Ball-in-Bowl type molecular structure. *Polyhedron*, 2009, **28**, 2450-2458.

[32] Toxic FAQ Sheet for Ammonia. Agency for Toxic Substances and Disease Registry (ATSDR). September 2004.

[33] J. Helminen, J. Helenius, E. J. Paatero. Adsorption equilibria of ammonia gas on inorganic and organic sorbents at 298.15 K. *Chem. Eng. Data*, 2001, **46**, 391-399.

[34] C. J. Doonan, D. J. Tranchemontagne, T. G. Glover, J. R. Hunt, O. M. Yaghi. Exceptional ammonia uptake by a covalent organic framework. *Nat. Chem.*, 2010, **2**, 235-238.

[35] J.F. Moulder, W.F. Stickle, P.E. Sobol, K.D. Bomben, Handbook of X-ray Photoelectron Spectroscopy: A Reference of Standard Spectra for Identification and Interpretation of XPS Data, Chigasaki City, Japan, 2007.

[36] R. Ryoo, S. Jun. Improvement of hydrothermal stability of MCM-41 using salt effects during the crystallization process. *J. Phys. Chem. B*, 1997, **101**, 317-320.

[37] K. A. Cychosz and A. J. Matzger. Water stability of microporous coordination polymers and the adsorption of pharmaceuticals from water. *Langmuir*, 2010, **26**, 17198-17202.

[38] D. R. Lide, W. M. Haynes. Physical Constants of Inorganic Compounds. *CRC Handbook of Chemistry and Physics*, CRC Press, Boca Raton, FL, 2009.

[39] B. Mu, F. Li, K. S. Walton. A novel metal-organic coordination polymer for selective adsorption of CO2 over CH4. *Chem. Commun.*, 2009, **18**, 2493-2495.

[40] D. Trong On, S. M. J. Zaidi, S. Kaliaguine. Stability of mesoporous aluminosilicate MCM-41 under vapor treatment, acidic and basic conditions. *Microporous Mesoporous Mater.*, 1998, **22**, 211-224.

[41] B. Marler, U. Oberhagemann, S. Vortmann, H. Gies. Influence of the sorbate type on the XRD peak intensities of loaded MCM-41. *Microporous Mater.*, 1996, **6**, 375-383.

[42] S. Syukri, C. Fischer, A. Al Hmaideen, Y. Li, Y. Zheng, F. Kuhn. Modified MCM-41-supported acetonitrile ligated copper(II) and its catalytic activity in cyclopropanation of olefins. *Microporous Mesoporous Mater.*, 2008, **113**, 171-177.

[43] J. Goworek, A. Kierys, W. Gac, A. Borowka, R. Kusak. Thermal degradation of CTAB in as-synthesized MCM-41. *J. Therm. Anal. Calorim.*, 2009, **96**, 375-382.

[44] S. Damyanova, L. Dimitrov, R. Mariscal, J. L. G. Fierro, L. Petrov, I. Sobrados. Immobilization of 12-molybdophosphoric and 12-tungstophosphoric acids on metal-substituted hexagonal mesoporous silica. *Appl. Catal., A*, 2003, **256**, 183-197.

[45] C. G. Kontoyannis, N. V. Vagenas. Calcium carbonate phase analysis using XRD and FT-Raman Spectroscopy. *Analyst*, 1999, **125**, 251-255.

[46] A. M. B. Furtado, Y. Wang, T. G. Glover, M. D. LeVan. MCM-41 impregnated with active metal sites: synthesis, characterization, and ammonia adsorption. *Microporous Mesoporous Mater.*, 2011, **142**, 730-739.

[47] M. Seredych, A. B. Tamashausky, T. J. Bandosz. Graphite oxides obtained from porous graphite. *Adv. Funct. Mater.*, 2010, **20**, 1670-1679.

CHAPTER IV

CARBON SILICA COMPOSITES FOR SULFUR DIOXIDE AND AMMONIA ADSORPTION

4.1 Introduction

The carbon silica composite (CSC) introduced by Glover et al.[1] in 2008 consists of carbonized poly(furfuryl alcohol) within the pores of MCM-41. This was the first in a series of articles by our group to produce biphasic composite materials targeting light gas adsorption. The CSC provides a large surface area and two distinct phases in which adsorption can occur: a nonpolar (carbonaceous) phase and a polar (siliceous) phase. The CSC material is of interest since it is well documented that interactions between the adsorbate and adsorbent are affected by the polarity of each; nonpolar surfaces such as carbon show greater attraction for adsorbate molecules of low polarity, whereas polar surfaces have higher affinity for polar molecules.[2] Materials that provide both polar and nonpolar surfaces for adsorption demonstrate an advantage over single-phase adsorbents.

Composite materials incorporating active metal sites for chemisorption can also provide an advantage over single-phase adsorbents when regeneration is not a concern. Another manuscript published in this series considers the optimization of the silica phase of this composite material with metal active sites to enhance the ammonia capacity of one phase of the composite.[3] Addition of a carbonaceous phase and metal active sites in both phases would produce multifunctional adsorbent materials with broad applications.

Mesoporous materials with an ordered pore structure and large surface areas have shown great promise for use in industrial applications ranging from air to water purification. MCM-41, which is a member of the M41S family of siliceous materials,

is one popular example of this type of structured mesoporous material. MCM-41 was invented by Mobil scientists in the early 1990's.[4] This siliceous material forms a hexagonal close-packed structure composed of unidirectional channels arranged in a hexagonal manner.[5] This ordered mesoporous material has a high surface area and a repeating structure of cylindrical pores, which is an ideal backbone for a well characterized adsorbent material.

Extensive work by Foley and others[6–10] has provided the foundation for the use of carbonized furfuryl alcohol as one carbon phase of the composite material. Carbonized furfuryl alcohol has been extensively studied as a carbonaceous adsorbent material because it has a small pore size distribution centered at an average pore size of 4-5 Å.[6] Pore formation by furfuryl alcohol due to combustion depends on the carbonization temperature. Bertarione et al.[7] researched the carbonization of polymerized furfuryl alcohol within the pores of a zeolite at different temperatures and proposed decomposition mechanisms for the polymer in confined spaces at each temperature. They showed that furfuryl alcohol decomposes and amorphous carbon forms when heated to 400 °C. Foley[8] performed extensive work producing and characterizing carbogenic molecular sieves (CMS) using furfuryl alcohol as the carbon source. They determined that carbonization above 600 °C results in a fully amorphous carbon material, and the highest micropore surface area was achieved at carbonization temperatures in the 800-900 °C range.[10] In another paper,[6] it was determined that both mesopores and micropores began to appear within the material at carbonization temperatures as low as 300 °C. They speculate that mesopores are formed from the incomplete carbonization of polymer remnants and aromatic cores. As the carbonization temperature was increased from 300 °C to 600 °C, the initial mesoporosity collapsed, leaving only micropores ranging from 4-5 Å after carbonization at 500-600 °C. With such a narrow and controlled pore size distribution, furfuryl alcohol-based CMS materials are useful for separating two gaseous compounds of dif-

ferent sizes.[11] The small pore sizes and large surface area of this CSC material make it a good candidate for the removal of light gases for air purification.[12]

Carbonized sucrose is another carbon phase that could be of interest in a CSC material. Sucrose has been shown to form a mesoporous carbon phase with high surface areas (on the order of 1000 m^2/g) and a pore size of approximately 20 Å.[13,14] Extensive work on sucrose carbonization has been performed at different temperatures and using different synthesis procedures. Ting et al.[14] performed a one-pot synthesis using sucrose catalyzed with sulfuric acid and carbonized at 900 °C. The resulting mesoporous carbons had surface areas of 1200 m^2/g and 44 Å pores. Peng et al.[15] synthesized mesoporous carbonaceous materials at carbonization temperatures ranging from 400-600 °C. In 2009, Zhuang and Yang[16] successfully produced carbonaceous spheres from aqueous sucrose solutions carbonized under high pressure at 175 °C. Zheng et al.[17] took advantage of the low temperature carbonization of sucrose to produce CMK-3 type materials by carbonizing sucrose in ethanol at 200 °C in a high pressure reactor. Banham et al.[13] templated sucrose into hexagonal mesoporous silicas. After high temperature carbonization, the ordered mesoporous carbon silica composites were evaluated as materials for electrochemical capacitors. Sucrose has also been templated into silica gel and carbonized at 800 °C.[18] Bimodal porous carbons have been produced by impregnating silica spheres with sucrose and carbonizing at high temperatures.[19] After removal of the silica spheres, the carbon phase was found to be connected by macropores and mesopores.

Sucrose as a carbon phase is different from carbonaceous furfuryl alcohol since the pores are larger and the temperature necessary for carbonization is much lower than that of furfuryl alcohol. Consequently, impregnating MCM-41 with carbonaceous sucrose results in a different composite material that could be useful for air purification.

The introduction of active metal sites for chemisorption has been widely used

to enhance the efficiency of adsorbent materials. Sheppard and Buckley[20] studied Zn-MCM-41 samples as materials for hydrogen adsorption. Savidha and Pandurangan[21] used zinc sulfate to incorporate zinc into MCM-41 using a substitution method that maintained the long range order of the MCM-41. In the carbon phase, there have been reports of successful formation of a ZnO-carbon composite material by dispersing zinc chloride into a furfuryl alcohol solution and heating at temperatures ranging from 100-800 °C under nitrogen with small amounts of oxygen.[22] Other groups have used copper and zinc nitrate as active sites to enhance catalysis.[23–25] In 2007, a study was published investigating the effects of metal sites, specifically iron, copper, and zinc, substituted into aluminated MCM-41.[26] These studies demonstrate that incorporating zinc, copper, and iron into the pores of adsorbent materials provides an effective means of catalyzing reactions and providing active sites for chemisorption.

This research focuses on carbonaceous CSC materials as biphasic adsorbents for toxic light gas adsorption. It builds on previous research from our group also published in this journal that introduced a CSC material based on MCM-41 and furfuryl alcohol,[1] optimized its synthesis,[27] characterized its light gas adsorption properties,[1,27] and optimized the silica phase of the CSC for basic gas adsorption.[3] In this research, the carbonization method for CSC materials with different carbon phases is investigated. The pore sizes and structure are examined after carbonization at different temperatures to increase surface area in the CSCs. The materials are characterized using nitrogen adsorption isotherms, X-ray diffraction, thermogravimetric analysis, and tested for toxic light gas adsorption capacity. The most promising materials are then impregnated with active metal sites and tested for adsorption of toxic light gases.

4.2 Experimental Methods

Materials

MCM-41

Tetramethylammonium hydroxide pentahydrate, TMAOH,(97 %),tetramethylammonium silicate solution, TMASi, (99.99 %, 15-20 wt % in water), sulfuric acid (95.0-98.0 %), and furfuryl alcohol (99 %) were purchased from Sigma Aldrich. Hexadecyltrimethylammonium chloride, CTAC, (25 %) in water was purchased from Pfaltz and Bauer. A solution of ammonium hydroxide (29 wt %) in water, Cab-O-Sil M5, and anhydrous zinc chloride were purchased from Fisher Scientific. Copper nitrate, zinc nitrate, and iron nitrate were purchased from Fisher Scientific and were ACS grade chemicals.

CSC-furfuryl alcohol

Furfuryl alcohol (99 %) and toluene (99 %) were purchased from Sigma Aldrich.

CSC-sucrose

Sucrose was purchased from Fisher Scientific and dry ethanol (200 proof) was purchased from Pharmco-aaper.

MCM-41 synthesis

All CSC materials include MCM-41 as the silica phase. Hexagonally-ordered MCM-41 with a 37 Å pore was synthesized according to the procedure described in a previous study.[3]

CSC-FA

CSC-FA synthesis

The furfuryl alcohol-impregnated carbon silica composite material was synthesized using the procedure outlined by Glover et al.[1] After impregnation with the furfuryl alcohol phase, the samples were carbonized at the following temperatures: 300, 500, and 600 °C, following the method previously described.[1]

Metal impregnation in the silica phase

For the impregnation of metals into the silica phase, 5 wt % metal salt versus silica, which corresponds to 0.23 g of metal salt ($ZnCl_2$, $Cu(NO_3)_2$, or $Fe(NO_3)_3$), was added to the MCM-41 reaction gel. To accomplish this impregnation, 2.4 g of 29 wt % ammonium hydroxide was mixed with 21.2 g of 26 wt % hexadecyltrimethylammonium chloride to create solution A. Solution B was formed by mixing 3.04 g tetramethylammonium hydroxide pentahydrate and 20 g of 10 wt % tetramethylammonium silicate. Solutions A and B were then combined while stirring. Then, 5 wt % metal salt and 4.5 g Cab-O-Sil M5 were added to the reaction gel with stirring. The reaction was stirred for 30 minutes, then placed in a Teflon-lined reaction vessel and heated to 80 °C. The remainder of the procedure mirrors that of Glover et al.[1]

Metal impregnation in the carbon phase

Active metal sites were impregnated into the carbon phase of the CSC-FA samples by introducing zinc chloride, copper nitrate, and iron nitrate into the synthesis procedure. To impregnate metals in the carbon phase, aluminated-MCM-41 was mixed with 5 wt % metal salt on a per carbon basis (assuming a 37 % carbon impregnation yield in the base CSC material; therefore 1.4 g of metal salt), 24 mL furfuryl alcohol, and 6 mL toluene. This solution was stirred in an ice bath for 18 hours. The liquid was then separated from the impregnated MCM-41 using vacuum filtration, and the recovered sample was heated in a furnace according to the procedure developed by Glover et al.[1]

CSC-sucrose

CSC-sucrose synthesis

The sucrose-impregnated CSC material was synthesized using a low temperature carbonization technique. Equal parts ethanol and water were mixed in a Teflon-lined Parr reactor at room temperature. One gram of sucrose was then added to the mixture, which was then covered and stirred vigorously for thirty minutes. Next, 0.2 g

of calcined MCM-41 was added to the mixture and stirred an additional 1 hour. The Parr reactor was then sealed and put into the oven at 200 °C for either 24 hours (to produce CSC-1) or 48 hours (to produce CSC-2). After the reaction was complete, the Parr reactor was removed from the oven and cooled to room temperature. The CSC material was then separated from the brown solution via vacuum filtration and rinsed with distilled water. The CSC was air dried overnight.

Active metal site impregnation in the carbon phase

A series of metal salts were impregnated into the carbon phase of the CSC materials to enhance the sulfur dioxide capacity. The nitrates of zinc, copper, and iron were added to the CSC reaction mixture in a silicon : metal ratio of 5 : 1. Equal parts ethanol and water were mixed in a teflon-lined Parr reactor at room temperature. The appropriate amount of metal salt and 1 gram of sucrose was added to the mixture, which was then covered and stirred for 30 minutes. The remainder of the procedure mirrors that of the base CSC synthesis.

Materials characterization

Textural characterization

Adsorption isotherms were measured using a Micromeritics ASAP 2020 at -196 °C with either UHP argon or UHP nitrogen as the analysis gas. Prior to measurement, approximately 0.1 g of each sample was degassed with heating to 90 °C and vacuum to 10 μbar. After reaching 10 μbar, the samples were heated to 100 °C under vacuum for an additional 6 hours.

X-ray diffraction (XRD)

XRD spectra were used to confirm the long range structure of the native and impregnated MCM-41 samples. The spectra were measured using a Scintag X1h/h automated powder diffractometer with Cu target, a Peltier-cooled solid-state detector, a zero background Si(5 1 0) support, and with a copper X-ray tube as the radiation

source. Spectra were collected from 1.2 to 7 degrees two θ using a step size of 0.02 degrees.

Thermogravimetric analysis (TGA)

Thermogravimetric analysis was performed on the CSC materials to determine the amount of carbon impregnated into the MCM-41. A TA Instruments Q600 SDT simultaneous DSC-TGA was used for the thermogravimetric analysis. Samples were heated in zero air from room temperature to 600 °C using a ramp rate of 5 °C per minute with an air flow rate of 10 ml per min. To fully burn off the carbonaceous phase, the samples were maintained at 600 °C for 3 hours.

Light gas capacity

Equilibrium capacities for room temperature light gas adsorption of both ammonia and sulfur dioxide were measured for all samples using a breakthrough apparatus, a schematic of which is given in Chapter 1 and Furtado et al.[3,28] Prior to analysis, all samples were regenerated under vacuum at 120 °C for 2 hours.

The flow rate of gas across the adsorbent bed was kept constant at 1133 mg/m^3 for ammonia (1500 ppm in helium) and 1428 mg/m^3 for sulfur dioxide (500 ppm in helium). The capacity of the adsorbent material, n (mol ammonia/kg adsorbent), was calculated via material balance using

$$n = \frac{F}{m} \int_0^\infty (c_0 - c)\, dt \tag{4.1}$$

where c_0 is the feed molar concentration, and c is the effluent concentration at time t. The volumetric flow rate of gas through the adsorbent bed, F, was adjusted to yield a breakthrough time of approximately one hour. The mass of the sample, m, was approximately 10 mg and was contained in a small cylindrical adsorbent bed. The capacities calculated using the breakthrough apparatus have a standard deviation on the order of 3 %, and different batches of CSC and metal impregnated CSCs are repeatable to within 5 %.

4.3 Results

CSC-Furfuryl Alcohol

Unimpregnated CSC-FA carbonized at different temperatures

The CSC-FA materials were characterized by X-ray diffraction to verify that the impregnation of the silica phase with carbon did not disrupt the MCM-41 structure. Figure 4.1 shows the XRD spectra of the base CSC-FA materials carbonized at different temperatures and the MCM-41 base material. Despite the decrease in intensity of the base CSC materials compared to MCM-41, which is due to interference from the carbon phase, the MCM-41 peaks are identifiable in the CSC-FA spectra. Thus, carbon impregnation does not alter the MCM-41 hexagonal order. Long range XRD scans were also run to look for evidence of graphitization, which can be expected to occur during carbonization at higher temperatures. No graphitic peaks were detected from these scans.

Characterization of the CSC-FA materials was performed by measuring argon isotherms at 77 K. It was previously reported that the carbon phase resulting from furfuryl alcohol carbonization results in slow nitrogen diffusion.[8] Consequently, argon was used to perform the isotherm measurements. Using the IUPAC classification system, the isotherms in Figure 4.2 are representative of Type I isotherms. The base CSC-FA materials are nanoporous, and exhibit Type I behavior due to the sharp increase in the amount adsorbed at low relative pressures, which levels off as the relative pressure approaches unity. The hysteresis during desorption is characteristic of a Type IV isotherm. This could mean either incomplete MCM-41 pore filling during impregnation with carbon, or the material could be classified as Type H4, which is characteristic of slit-shaped pores in the micropore size range.[12]

Surface area and pore information were calculated from the adsorption isotherm for the unimpregnated CSC-FA materials. The Brunauer-Emmett-Teller surface areas were calculated according to the procedure for microporous materials

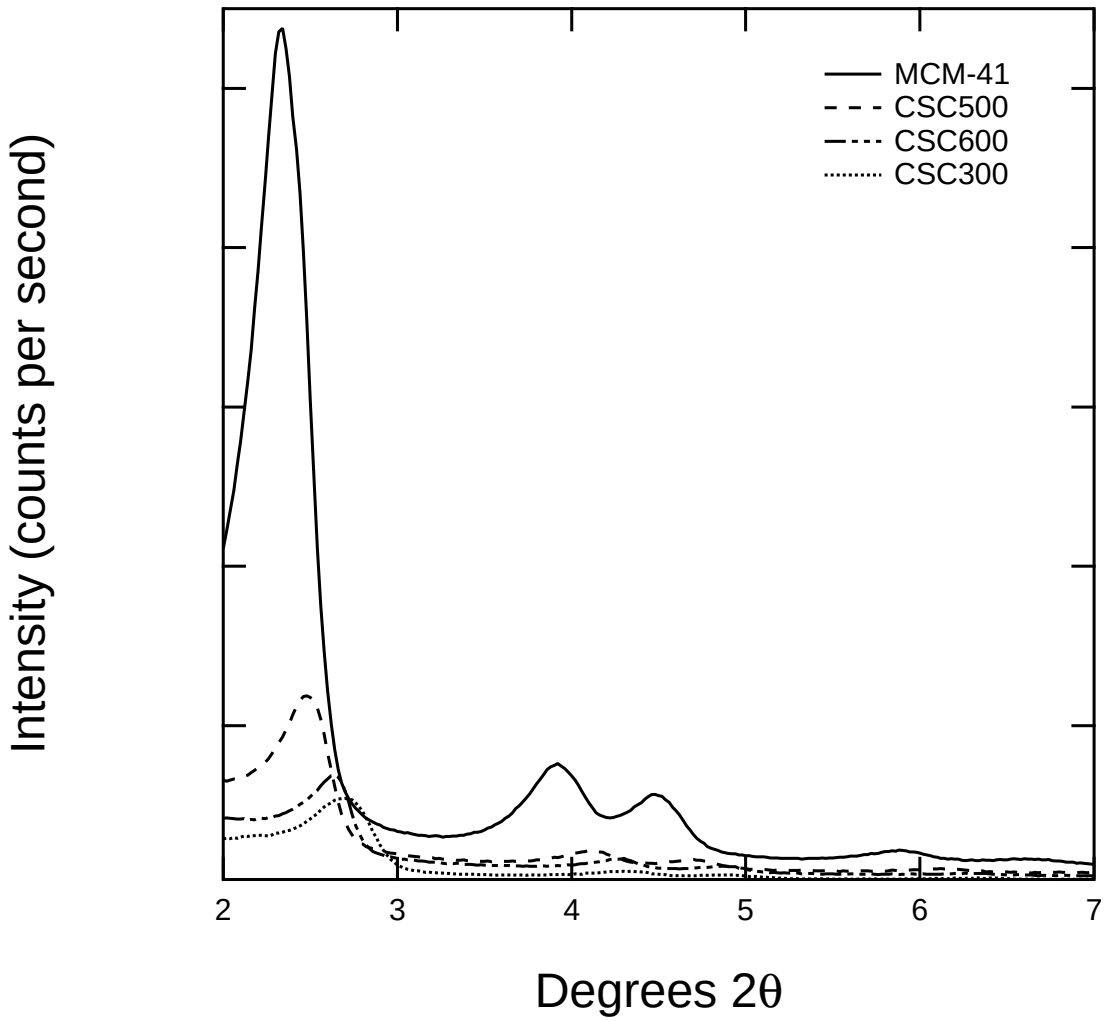

Figure 4.1 X-ray diffraction spectra for MCM-41 and CSC-FAs carbonized at different temperatures.

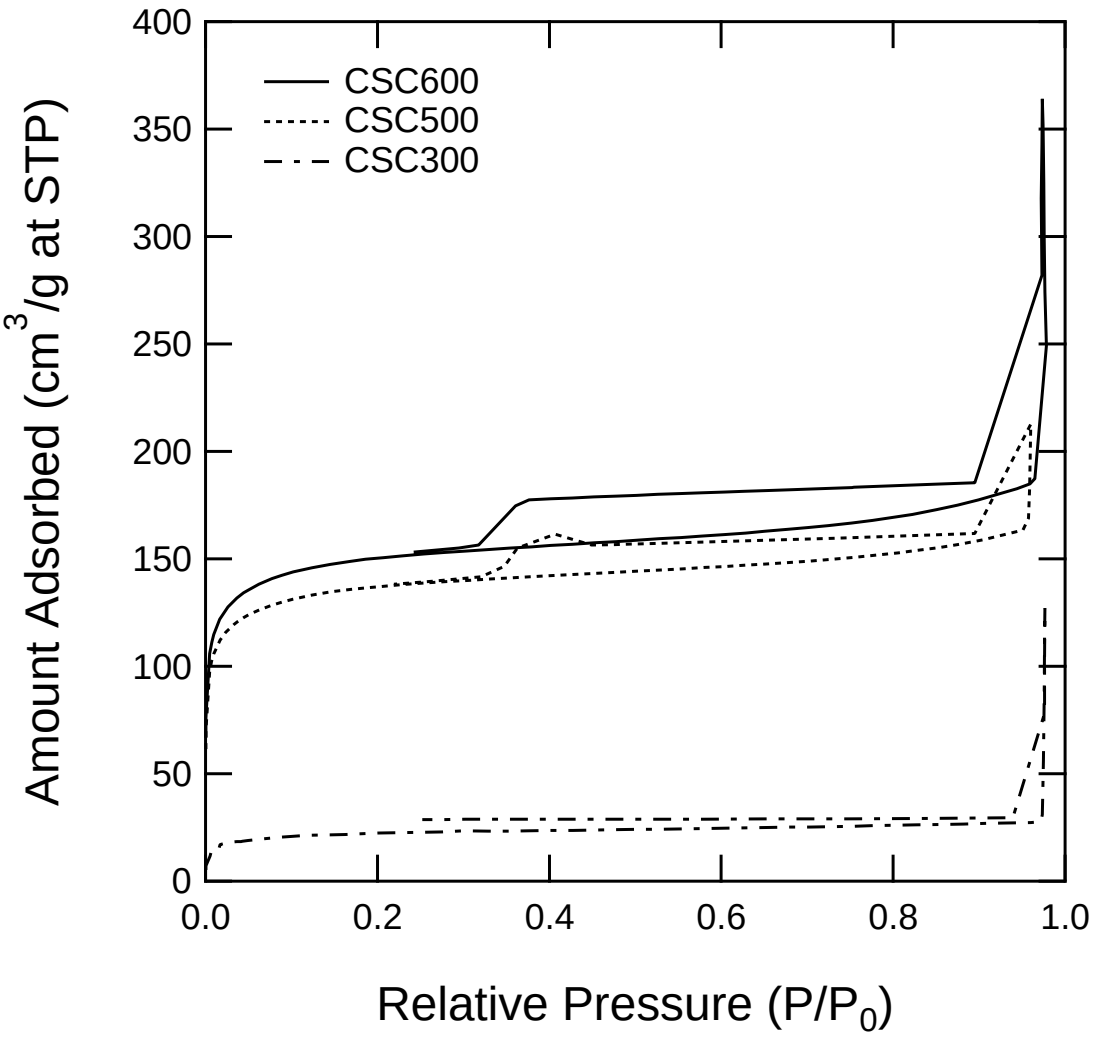

Figure 4.2 Adsorption isotherms for CSC-FAs carbonized at different temperatures.

Table 4.1: BET surface areas, pore volumes, and amount of carbon in each CSC-FA carbonized at different temperatures and in MCM-41

Sample	Carbonization Temp. (K)	BET SA (m^2/g)	V_{pore} (cm^3/g)	wt % carbon
MCM-41	–	836	1.2	–
CSC300	300	73	0.2	51
CSC500	500	434	2.3	40
CSC600	600	490	0.5	44

outlined by Rouquerol et al.[29] and are summarized in Table 4.1. When all samples are compared, the samples carbonized at mid-range temperatures (500-600 °C) have higher surface areas and larger pore volumes than the sample carbonized at 300 °C.

TGA analysis was performed on the CSC-FA samples produced at different carbonization temperatures. As summarized in Table 4.1, TGA data shows that the CSC-FA carbonized at 300 °C sample has the highest mass loss, 51 wt %, due to incomplete polyfurfuryl alcohol carbonization at the lower temperature. The average carbon content for the remaining samples is approximately 40 %.

Metal impregnation of CSC-FA

Calculated BET surface areas from adsorption isotherms of the parent CSC600 and metal-impregnated CSC600 materials are shown in Table 4.2. Similar to the base CSC-FA material, the metal-impregnated CSC-FA isotherms exhibit Type I behavior. Except for the CSC[Si(0),C(Fe)] sample, the metal impregnations result in decreases in surface area compared to the unimpregnated CSC.

Select X-ray diffraction spectra are shown in Figure 4.3. All samples impregnated with metals maintain the hexagonal order of the MCM-41 phase apparent in the CSC-FA base material. According to Sheppard and Buckley,[20] a slight shift toward a lower 2θ value for an XRD peak results from an increase in wall thickness, provided the pore size remains constant. Because the (1 0 0) peak in the CSC[Si(Fe),C(0)] sample shows a slight shift toward a lower 2θ value, there is an increase in wall thick-

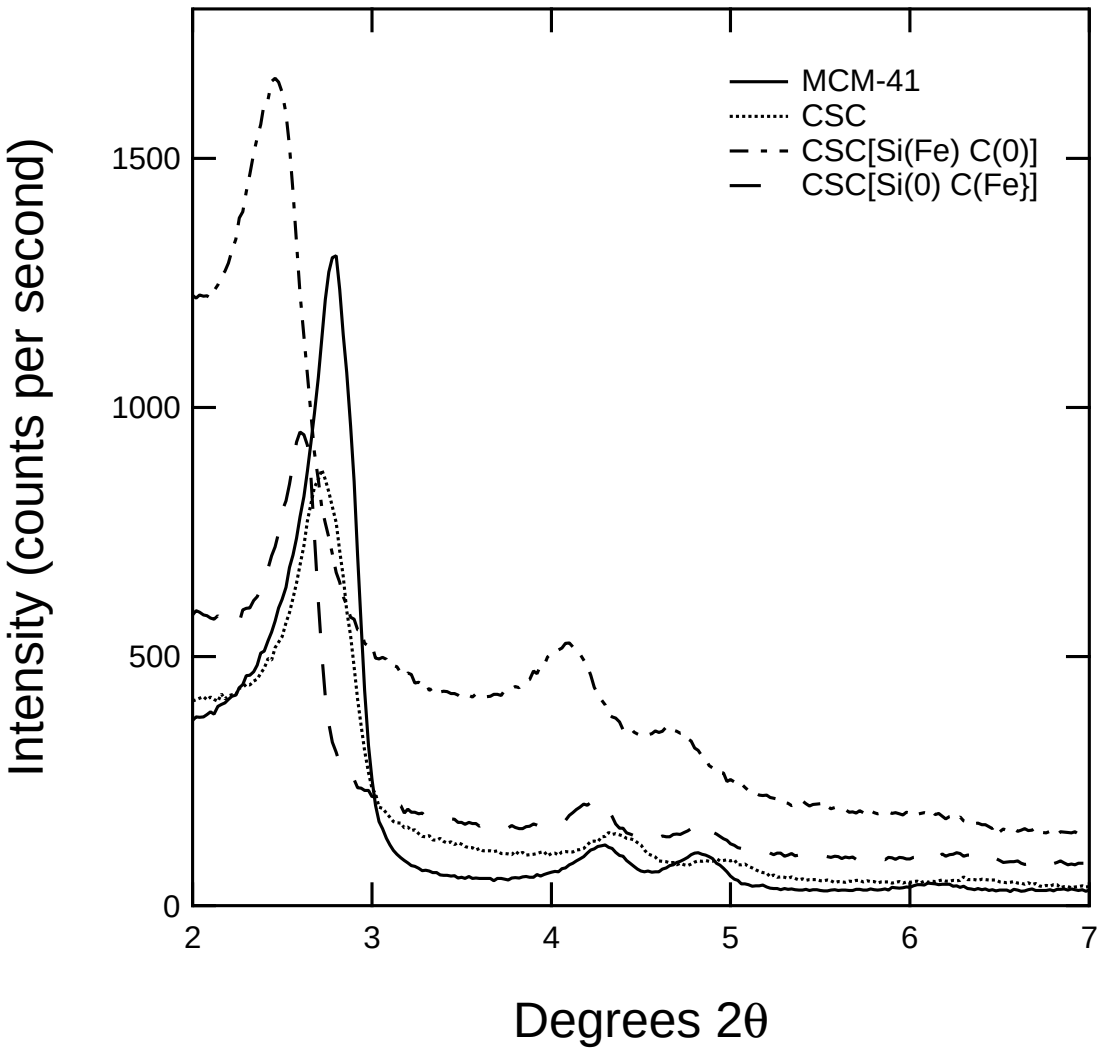

Figure 4.3 Select XRD spectra for metal impregnated CSC-FAs.

Table 4.2: BET surface areas, pore volumes, and amount of carbon in CSC-FA and metal impregnated CSC-FAs

Sample	BET SA (m^2/g)	V_{pore} (cm^3/g)
CSC600	490	0.48
CSC[Si(0)C(Zn)]	320	0.23
CSC[Si(0)C(Cu)]	488	0.33
CSC[Si(0)C(Fe)]	556	0.28
CSC[Si(Zn)C(0)]	376	0.16
CSC[Si(Cu)C(0)]	400	0.26
CSC[Si(Fe)C(0)]	421	0.22

ness of the MCM-41 pore wall due to the incorporation of iron into the silica wall. This is the case for all samples with metals impregnated in the silica phase.

Light gas adsorption for CSC-FA samples

Table 4.3 summarizes the light gas adsorption capacities for the unimpregnated CSC-FA samples and for the parent MCM-41. The presence of the carbon phase enhances the sulfur dioxide adsorption compared to the parent MCM-41, with CSC600 having the highest SO_2 capacity. When compared on a mol/kg silica basis, the carbon phase produced at 300 °C carbonization temperature causes a decrease in the ammonia capacity compared to MCM-41. However, the carbon phases in CSC500 and CSC600 result in an increase in the ammonia capacity compared to the base MCM-41. For the CSC-FA samples, it is obvious that higher adsorption capacities correspond to higher carbonization temperatures. This is consistent with the physical characteristics of the samples, which show incomplete furfuryl alcohol carbonization at the low carbonization temperature. The sample carbonized at 300 °C shows a decrease in ammonia and sulfur dioxide capacity compared to the samples carbonized at 500 and 600 °C.

The porosity and hexagonal order of the CSC-FA samples carbonized at 500 and 600 °C should be most beneficial for active site impregnation. The sample car-

Table 4.3: Ammonia and sulfur dioxide equilibrium adsorption capacities for MCM-41 and CSC-FA samples

Sample	SO_2 Capacity		NH_3 Capacity	
	mol/kg sample	mol/kg carbon	mol/kg sample	mol/kg SiO_2
MCM-41	0.02	0.02	2.01	2.01
CSC300	0.20	0.55	0.76	1.19
CSC500	0.25	0.71	1.38	2.14
CSC600	0.34	0.95	1.48	2.30

bonized at 300 °C is not fully carbonized; the surface area is low since the furfuryl alcohol polymer structure has not fully collapsed. The sample carbonized at 600 °C has slightly higher surface area and higher light gas capacities than the 500 °C sample. Consequently, active metal site impregnations will focus on CSC-FA carbonized at 600 °C.

Table 4.4 summarizes the ammonia and sulfur dioxide capacities for the unimpregnated and metal impregnated CSC-FA samples. The same weight percentage of three different metals were impregnated into each phase of the CSC-FA materials to determine which metal enhances ammonia adsorption (by impregnating into the silica phase) and to determine which enhances sulfur dioxide adsorption (via impregnation into the carbon phase). Unfortunately, all metals impregnated into both phases either maintain or reduce the ammonia and sulfur dioxide capacities compared to the parent CSC-FA.

One possible reason for the lack of TIC capacity enhancement resulting from the metal impregnations is that the high temperatures necessary for furfuryl alcohol carbonization causes the metal salts to decompose to states of lower reactivity. According to Furtado et al.,[3] the metal salts used to impregnate active sites into the CSCs decompose to metal oxides at temperatures above 250 °C. Since the furfuryl alcohol polymer must be carbonized between 500 and 600 °C for several hours, it is possible that the active metal sites decompose during the carbonization process and

Table 4.4: Ammonia and sulfur dioxide equilibrium adsorption capacities for CSC-sucrose and metal impregnated CSC-sucrose samples

Sample	SO_2 Capacity		NH_3 Capacity	
	mol/kg sample	mol/kg carbon	mol/kg sample	mol/kg SiO_2
MCM-41	0.02	0.02	2.01	2.01
CSC600	0.34	0.95	1.48	2.30
CSC[Si(0)C(Zn)]	0.3	0.60	0.85	1.79
CSC[Si(0)C(Cu)]	0.2	0.42	0.61	1.19
CSC[Si(0)C(Fe)]	0.35	0.99	1.29	2.22
CSC[Si(Zn)C(0)]	0.23	0.57	1.11	2.02
CSC[Si(Cu)C(0)]	0.13	0.31	1.05	2.00
CSC[Si(Fe)C(0)]	0.24	0.55	0.81	1.59

are unavailable for chemisorption in the final product. Another possibility is that impregnation with metal salts physically blocks the pores of the carbon phase and thus reduces the ammonia and sulfur dioxide capacities. This is backed up by the data in Table 4.2, which shows that all metal salt impregnated samples also result in a decrease in surface area and pore volume compared to the parent CSC material. The only sample that does not show a surface area decrease after metal impregnation is the sample with iron impregnated in the silica phase, and the sulfur dioxide and ammonia capacities of this sample are closest to that of the parent CSC.

CSC-Sucrose

CSC synthesis and characterization

Two CSC materials using sucrose as the carbon phase were successfully produced by impregnating MCM-41 with carbonaceous sucrose using two different reaction times. As shown via the thermogravimetric analysis in Figure 4.4, the amount of carbon loaded into the MCM-41 scales with the reaction time. The initial mass loss corresponds to the liberation of adsorbed water and the second gradual mass loss represents the loss of carbon from the samples. Table 4.5 summarizes the amount of

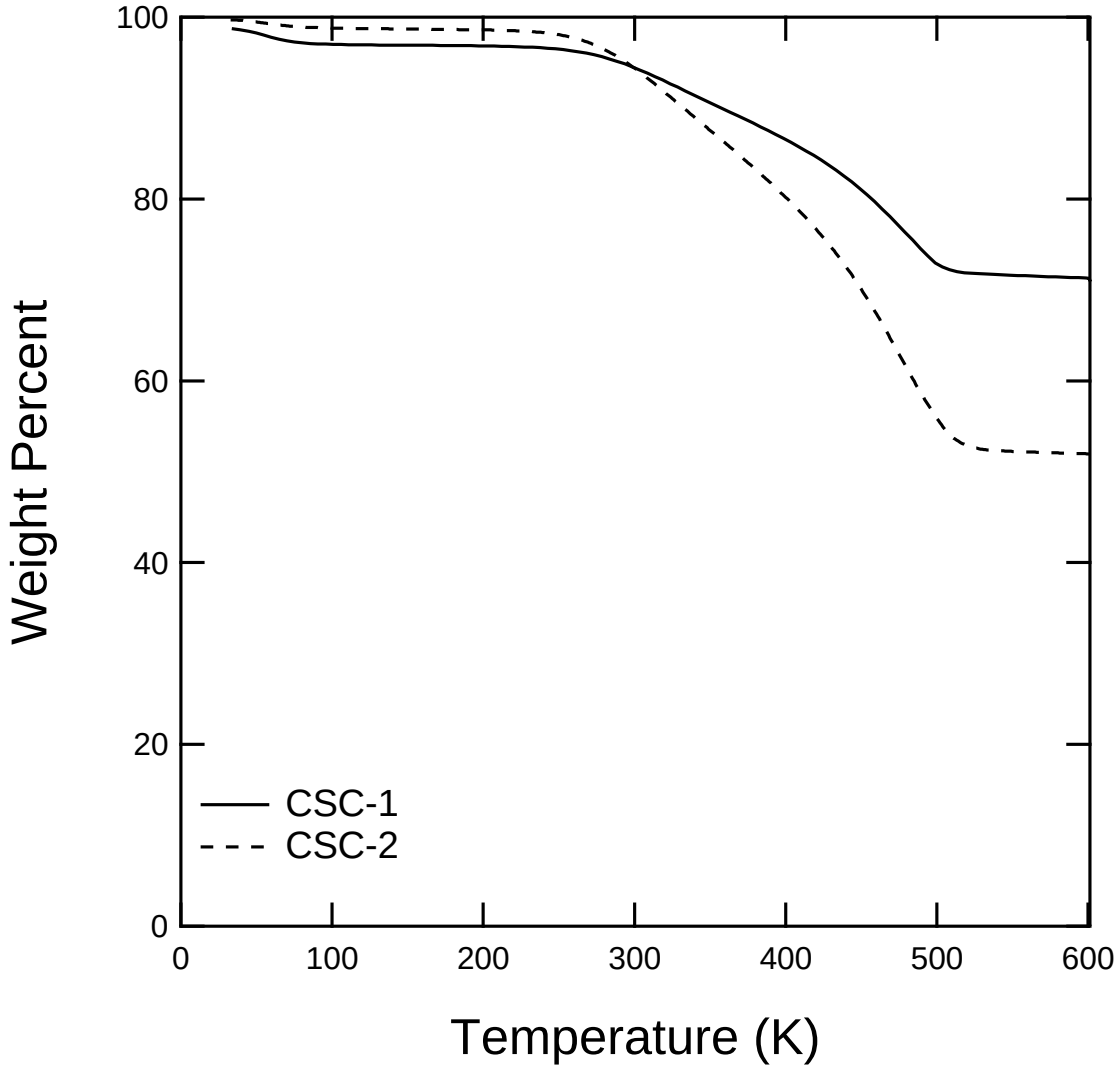

Figure 4.4 Thermogravimetric analysis of CSC-sucrose samples.

Table 4.5: Physical properties of the CSC-sucrose samples

Sample	Reaction Time (hrs)	wt % Carbon	BET SA (m^2/g)	V_{pore} (cm^3/g)
CSC-1	24	26	436	0.56
CSC-2	48	46	263	0.45

carbon loaded into each sample. Based on the TGA information, the longer reaction time results in a larger weight percentage of carbon within the CSC material.

Nitrogen isotherms are summarized in Figure 4.5 for both CSC-sucrose materials and for the unimpregnated MCM-41. The parent MCM-41 exhibits a Type IV behavior, and the CSC isotherms are hybrids between Type I and Type IV according to the IUPAC classification.[30] The CSCs are microporous, and exhibit Type I behavior due to the sharp increase in the amount adsorbed at low relative pressures, which levels off as the relative pressure increases. The hysteresis during desorption is characteristic of a Type IV isotherm. This could mean either incomplete MCM-41 pore filling during impregnation with carbon, or the material could be classified as Type H4, which is characteristic of slit-shaped pores in the micropore size range.[12] BET surface areas and pore volumes calculated from the isotherms are summarized in Table 4.5. Impregnating MCM-41 with the sucrose phase decreases the surface area and pore volume of the materials compared to the parent MCM-41, which has a surface area of 836 m^2/g and a pore volume of 1.2 cm^3/g. This is due to filling the mesopores with a carbon phase, which results in an increase in microporosity and a decrease in mesoporosity. The initial MCM-41 has an average pore size of approximately 37 Å. After filling the MCM-41 pores with different amounts of sucrose carbon, density functional theory predicts much lower pore sizes, which are a result of pores formed by the carbon phase. Consequently, it is evident that sucrose carbon fills the MCM-41 mesopores and introduces micropores into the material after carbonization.

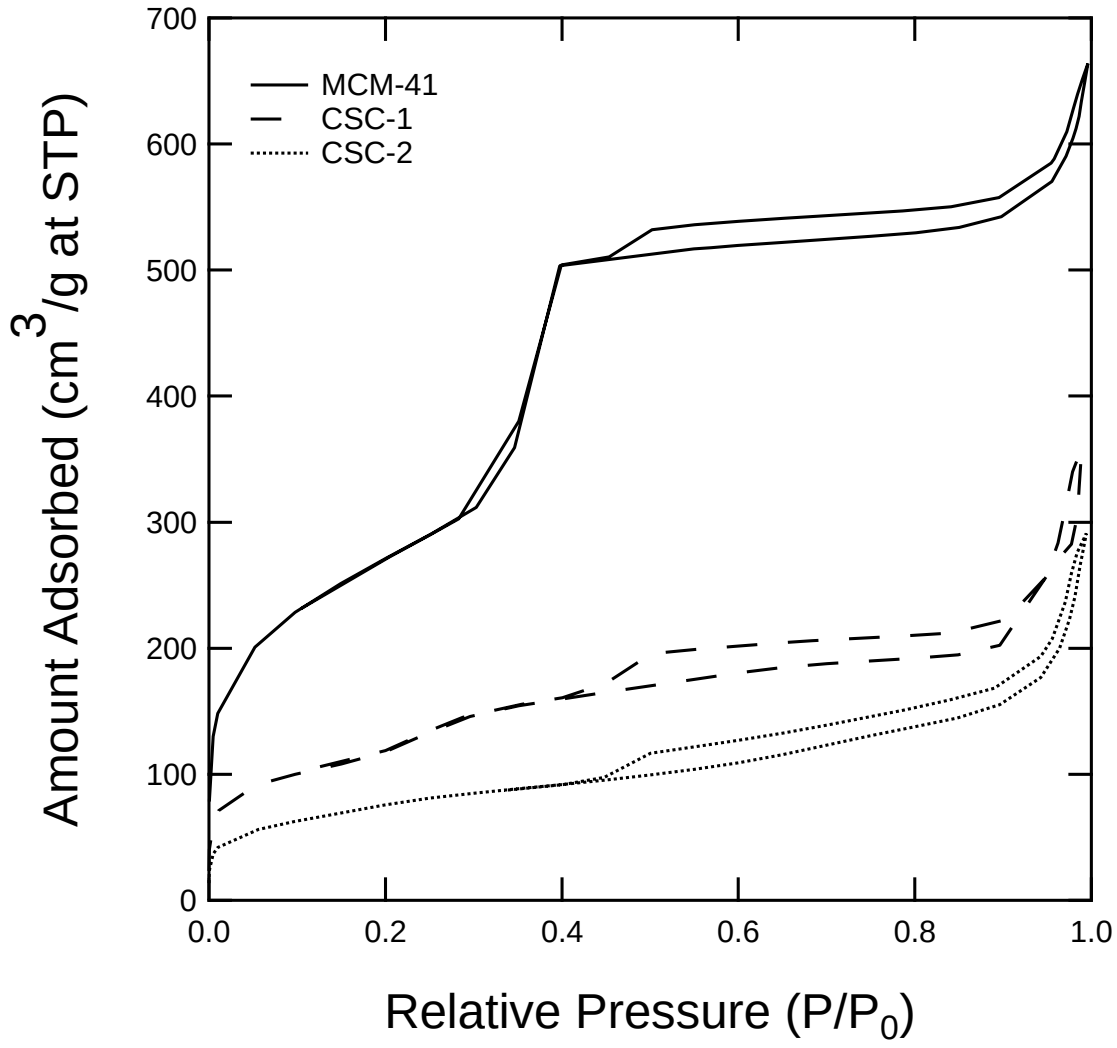

Figure 4.5 Adsorption isotherms for CSC-sucrose samples.

Table 4.6: Physical properties of the metal impregnated CSC-sucrose samples

Sample	BET SA (m^2/g)	V_{pore} (cm^3/g)
CSC	436	0.56
CSC[$Zn(NO_3)_2$]	347	0.62
CSC[$Cu(NO_3)_2$]	128	0.33
CSC[$Fe(NO_3)_3$]	116	0.45

Impregnation of active metal sites into CSC-sucrose

The nitrates of zinc, copper, and iron were impregnated into the carbon phase of the CSC during synthesis. Nitrogen isotherms of these materials are compared in Figure 4.6. The metal impregnated samples maintain the Type IV isotherm behavior characteristic of the parent CSC-sucrose samples. Table 4.6 summarizes the BET surface areas and pore volumes calculated from the isotherms. It is evident that BET surface areas of the metal impregnated CSCs are much lower than the base CSC-sucrose and the unimpregnated MCM-41.

CSC-sucrose light gas adsorption

As summarized in Table 4.7, the sucrose-based carbon silica composites were tested for ammonia and sulfur dioxide capacity and compared to MCM-41. It is obvious from the table that the presence of the sucrose carbon phase increases both the ammonia and sulfur dioxide capacities compared to the parent MCM-41. When the ammonia capacities are compared on a mol/kg SiO_2 basis, the carbon phase enhances the ammonia capacity over the base siliceous phase. For sulfur dioxide, the carbon phase provides base capacity for the composite, whereas the silica phase does not. Consequently, impregnating this CSC material with active metal sites has the potential to enhance the sulfur dioxide capacity to a large degree.

Since there was minimal difference between the sulfur dioxide capacities of the CSC samples carbonized for 24 and 48 hours, the 24 hour synthesis procedure was followed when impregnating the metal salts into the carbon phase. The sulfur dioxide

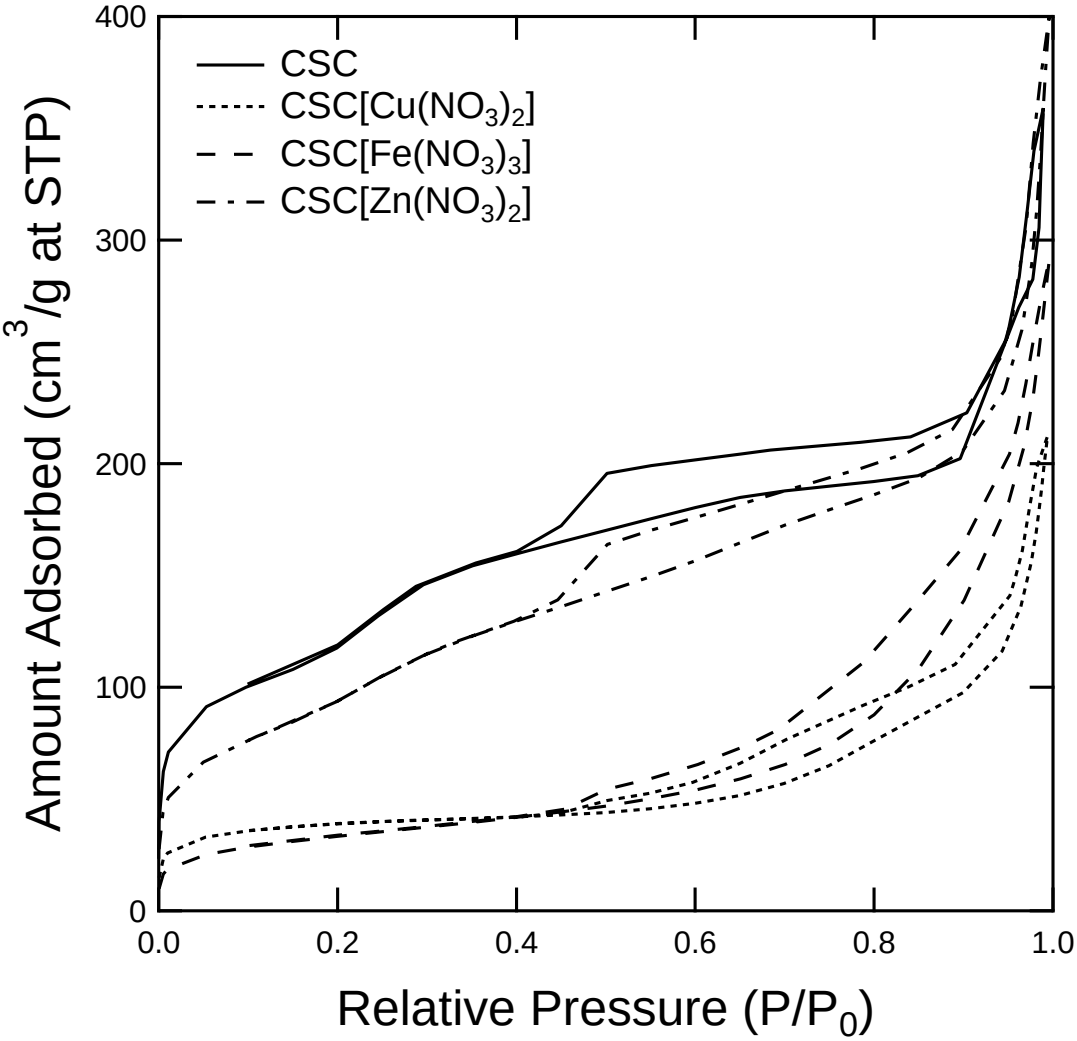

Figure 4.6 Nitrogen isotherms for CSC-sucrose and metal impregnated CSC samples.

Table 4.7: Light gas adsorption of the CSC-sucrose samples

Sample	SO_2 Capacity		NH_3 Capacity	
	mol/kg sample	mol/kg carbon	mol/kg sample	mol/kg SiO_2
MCM-41	0.02	0.02	2.01	2.01
CSC-1	0.10	0.38	2.18	2.95
CSC-2	0.15	0.33	2.10	3.93

Table 4.8: Sulfur dioxide adsorption of the metal impregnated CSC-sucrose samples

Sample	SO_2 Capacity	
	mol/kg sample	mol/kg carbon
CSC-1	0.10	0.38
CSC[$Zn(NO_3)_2$]	0.10	0.26
CSC[$Cu(NO_3)_2$]	0.06	0.07
CSC[$Fe(NO_3)_3$]	0.14	0.35

capacities for these metal impregnated materials are summarized in Table 4.8. It is evident that the metal salt impregnations did not enhance the sulfur dioxide capacities of these materials when compared to the unimpregnated CSC. It is possible that the metal salts are degrading at the temperature necessary for sucrose carbonization. The melting points for zinc nitrate, iron nitrate, and copper nitrate are 110 °C, 125 °C, and 256 °C, respectively.[31] With such low melting points, it is possible that the metal salts are decomposing to their metal oxides, even at the low sucrose carbonization temperature of 200 °C, and are unavailable in their reactive form to enhance the sulfur dioxide capacities.[3,32] Similar to the furfuryl alcohol CSCs, it is also possible that the metal salt impregnates are blocking the pores of the sucrose phase and thus decreasing the ammonia and sulfur dioxide capacities compared to the parent material.

4.4 Conclusions

A series of carbon silica composites with MCM-41 as the silica phase and carbonized furfuryl alcohol or sucrose as the carbon phase have been synthesized

using different carbonization temperatures. These materials have been characterized via adsorption isotherms, X-ray diffraction, and TGA. They were also tested for their ammonia and sulfur dioxide capacities. MCM-41 has a large capacity for ammonia and minimal affinity for the acidic gas sulfur dioxide.

Impregnation of MCM-41 with furfuryl alcohol to form the CSC maintains the ammonia capacity and enhances the sulfur dioxide capacity of the adsorbent. The CSC-FA carbonized at 600 °C has the highest surface area, followed by the samples carbonized at 500 and 300 °C. Carbonization of the furfuryl alcohol polymer is a rate process, consequently the sample heated to 300 °C is not fully carbonized, and the sample carbonized at 600 °C has the most well-developed pore structure.

Similar to furfuryl alcohol, impregnation of MCM-41 with carbonized sucrose results in an increase in the sulfur dioxide and ammonia capacities compared to the unimpregnated MCM-41. The carbonized sucrose phase of the composite enhances the sulfur dioxide capacity of the adsorbent compared to the unimpregnated silica phase. The sucrose phase also results in an increase in ammonia capacity. This increase in ammonia and sulfur dioxide capacity is true for samples impregnated using both 24 and 48 hour reaction time.

Metal sites have been successfully incorporated into the CSC adsorbents. The presence of these active sites within CSC-FA composites does not disrupt the structure of the base CSC, and all but one sample results in a surface area decrease compared to the unimpregnated CSC-FA. The metal site impregnations in both phases do not enhance the ammonia or sulfur dioxide capacities compared to the parent CSC-FA material. Similarly, the metal sites impregnated into the carbon phase of the CSC-sucrose do not enhance the sulfur dioxide capacities compared to the parent. It is possible that the metal salt impregnates block the pores of the carbon phases, as evidenced by the decrease in surface area for all metal impregnated samples. This pore blocking could also explain the lack of capacity enhancement seen for the metal

impregnated samples. Since both furfuryl alcohol and sucrose must be carbonized at elevated temperatures, it is also possible that the active metal sites decompose during the carbonization process and are unavailable for chemisorption in the final product. Metal impregnation into CSC materials composed of a carbon phase developed with a much lower temperature requirement could enhance the activity of the active metal sites by minimizing decomposition during synthesis.

Despite the lack of capacity enhancement provided by the metal salt impregnations, the presence of the carbon phases in the carbon silica composites successfully enhances the toxic light gas capacity compared to the parent silica phase. Consequently, these two novel carbon silica composites are promising candidates for air purification applications.

References

[1] T.G. Glover, K.I. Dunne, R.J. Davis, M.D. LeVan. Carbon-silica composite adsorbent: Characterization and adsorption of light gases. *Microporous Mesoporous Mater.*, 2008, **111**, 1-11.

[2] F. Rodriguez-Reinoso, M. Molina-Sabio, M. A. Muiiecas. Effect of microporosity and oxygen surface groups of activated carbon in the adsorption of molecules of different polarity. *J. Phys. Chem.*,1992, **96**, 2707-2713.

[3] A. M. B. Furtado, Y. Wang, T. G. Glover, M. D. LeVan. MCM-41 impregnated with active metal sites: synthesis, characterization, and ammonia adsorption. *Microporous Mesoporous Mater.*, 2011, **142**, 730-739.

[4] C.T. Kresge, M.E. Leonowicz, W.J. Roth, J.C. Vartuli, J.S. Beck. Ordered mesoporous molecular sieves synthesized by a liquid crystal template mechanism. *Nature*, 1992, **359**, 710-712.

[5] B. Marler, U. Oberhagemann, S. Vortmann, H. Gies. Influence of the sorbate type on the XRD peak intensities of loaded MCM-41. *Microporous Mater.*, 1996, **6**, 375-383.

[6] C. L. Burket, R. Rajagopalan, A. P. Marencic, K. Dronvajjala, H. C. Foley. Genesis of porosity in polyfurfuryl alcohol derived nanoporous carbon. *Carbon*, 2006, **44**, 2957-2963.

[7] S. Bertarione, F. Bonino, F. Cesano, A. Damin, D. Scarano, A. Zecchina. Furfuryl alcohol polymerization in H-Y confined spaces: reaction mechanism and structure of carbocationic intermediates. *J. Phys. Chem. B*, 2008, **112**, 2580-2589.

[8] H. C. Foley. Carbogenic molecular sieves: synthesis, properties and applications. *Microporous Mater.*, 1995, **4**, 407-433.

[9] K. Dettmer, W. Engewald. Adsorbent materials commonly used in air analysis for adsorptive enrichment and thermal desorption of volatile organic compounds. *Anal. Bioanal. Chem.*, 2002, **373**, 490-500.

[10] D. Lafyatis, J. Tung, H. C. Foley. Polyfurfuryl alcohol-derived carbon molecular sieves: dependence of adsorptive properties on carbonization temperature, time, and polyethylene glycol additive. *Ind. Eng. Chem. Res.*, 1991, **30**, 865-873.

[11] A. Hong, R. K. Mariwala, M. S. Kane, H. C. Foley. Adsorbate shape selectivity: separation of the HF/134a azeotrope over carbogenic molecular sieve. *Ind. Eng. Chem. Res.*, 1995, **34**, 992-996.

[12] F. Rouquerol, J. Rouquerol, K. Sing. Adsorption by Powders and Porous Solids. San Diego : Academic Press, 1999.

[13] D. Banham, F. Feng, J. Burt, E. Alsrayheen, V. Birss. Bimodal, templated mesoporous carbons for capacitor applications. *Carbon*, 2010, **48**, 1056-1063.

[14] C. Ting, H. Wub, S. Vetrivel, D. Saikia, Y. Pan, G. T.K. Fey, H. Kao. A one-pot route to synthesize highly ordered mesoporous carbons and silicas through organic-inorganic self-assembly of triblock copolymer, sucrose and silica. *Microporous Mesoporous Mater.*, 2010, **128**, 1-11.

[15] L. Peng, A. Philippaerts, X. Ke, J. Van Noyen, F. De Clippel, G. Van Tendeloo, P. A. Jacobs, B. F. Sels. Preparation of sulfonated ordered mesoporous carbon and its use for the esterification of fatty acids. *Cat. Today*, 2010, **150**, 140-146.

[16] Z. Zhuang, Z. Yang. Preparation and characterization of colloidal carbon sphere/rigid polyurethane foam composites. *J. App. Pol. Sci.*, 2009, **114**, 3863-3869.

[17] M. Zheng, Y. Liu, K. Jiang, Y. Xiao, D. Yuan. Alcohol-assisted hydrothermal carbonization to fabricate spheroidal carbons with a tunable shape and aspect ratio. *Carbon*, 2010, **48**, 1224-1233.

[18] A.Puziy, O. I. Poddubnaya, C. A. Reinish, M. M. Tsyba, L. I. Mikhalovska, S. V. Mikhalovsky. One-pot preparation of functionalized nanostructured carbons. *Carbon*, 2011, **49**, 599-604.

[19] S. Zhang, L. Chen, S. Zhou, D. Zhao, L. Wu. Facile synthesis of hierarchically ordered porous carbon via in situ self-assembly of colloidal polymer and silica spheres and its use as a catalyst support. *Chem. Mater.*, 2010, **22**, 3433-3440.

[20] D.A. Sheppard, C.E. Buckley. Hydrogen adsorption on porous silica. *Int. J. Hydrogen Energy*, 2008 **33**, 1688-1692.

[21] R. Savidha, A. Pandurangan. Vapour phase isopropylation of phenol over zinc- and iron-containing Al-MCM-41 molecular sieves. *Appl. Catal., A*, 2004, **262**, 1-11.

[22] F. Cesano, D. Scarano, S. Bertarione, F. Bonino, A. Damin, S. Bordiga, C. Prestipino, C. Lamberti, A. Zecchina. Synthesis of ZnO-carbon composites and imprinted carbon by the pyrolysis of $ZnCl_2$ catalyzed furfuryl alcohol polymers. *J. Photochem. Photobiol. A: Chem.*, 2008, **196**, 143-153.

[23] H. L. Huang, H. P. Wang, J.-E. Chang, Y.-L. Wei. Speciation and distribution of copper and zinc in MCM-41. *J. Electron. Spectrosc. Relat. Phenom.*, 2007, **156**, 357-360.

[24] M. Naderi, J. L. Pickett, M. J. Chinn, D. R. Brown. Modified mesoporous silicates for the adsorption and decomposition of toxic gases. *J. Mater. Chem*, 2002, **12**, 1086-1089.

[25] J. Y. Kim, J. S. Yu, L. Kevan. Location of cupric ion and its adsorbate interactions in Cu(II)-exchanged mesoporous AlMCM-41 determined by electron spin resonance and electron spin echo modulation. *Mol. Phys.*, 1998, **95**, 989-997.

[26] M. H. Nilsen, E. Antonakou, A. Bouzga, A. Lappas, K. Mathisen, M. Stocker. Investigation of the effect of metal sites in Me-Al-MCM-41 (Me = Fe, Cu or Zn) on the catalytic behavior during the pyrolysis of wooden based biomass. *Microporous Mesoporous Mater.*, 2007, **103**, 189-203.

[27] T. G. Glover, M. D. LeVan. Carbon-silica composite adsorbent: Sensitivity to synthesis conditions. *Microporous Mesoporous Mater.*, 2009, **118**, 21-27.

[28] A. M. B. Furtado, J. Liu, Y. Wang, M. D. LeVan. Mesoporous silica-metal organic composite: synthesis, characterization, and ammonia adsorption. *J. Mater. Chem.*, 2011, **21**, 6698-6706.

[29] J. Rouquerol, P. Llewellyn, F. Rouquerol. Is the BET equation applicable to microporous adsorbents? *Stud. Surf. Sci. Catal.*, 2007, **160**, 49-56.

[30] S. J. Gregg, K. S. W. Sing. Adsorption, Surface Area and Porosity. London: Academic Press, 1982.

[31] D.R. Lide, W.M. Haynes, CRC Handbook of Chemistry and Physics, CRC Press, Boca Raton, 2009.

[32] T. Tsoncheva, J. Rosenholm, M. Linden, F. Kleitz, M. Tiemann, L. Ivanova, M. Dimitrov, D. Paneva, I. Mitov, C. Minchev. Critical evaluation of the state of iron oxide nanoparticles on different mesoporous silicas prepared by an impregnation method. *Microporous Mesoporous Mater.*, 2008, **112**, 327-337.

CHAPTER V

BIFUNCTIONAL ORGANOALKOXYSILANE-GRAFTED SILICA COMPOSITES FOR ACIDIC AND BASIC GAS ADSORPTION

5.1 Introduction

Nanoporous adsorbents have attracted attention due to their numerous potential applications, which range from catalysts to energy storage and environmental protection materials.[1–4] The removal of light gases from air is of extreme interest in the United States today, since adsorbents that accomplish this have applications in a wide array of industries including building filtration and protection of military personnel and civilians. In particular, adsorbents for use in respirators and for protection against chemical threats should have high single-pass capacities for a broad spectrum of trace impurities.

Structured mesoporous silica materials, such as members of the M41S family, are prime candidates for use in new adsorbent applications. Members of the M41S family are formed via a liquid crystal templating method with ionic surfactants as structure directing agents.[1,5] The mesoporous materials are formed by condensing silica onto the surfactant liquid crystals and then removing the surfactant from the final product.[6] The high surface areas and regularly repeating structures allow for post synthetic modifications to tailor the adsorption capacity to specific types of molecules.[7–9]

There are two general routes available for surface modification of structured silicas with functional groups. First, in co-condensation, also known as one-pot synthesis, silane molecules containing the functional group of interest are included in the gel during synthesis. In this method, the surfactant must be removed from the pores using solvent extraction rather than calcination, since high temperatures would

result in destruction of the functional groups.[10] The resulting siliceous materials have different pore structures and morphology than the corresponding mesoporous material made without the organoalkoxysilane.[11,12] Second, in the post-synthetic grafting route, hydroxyl groups on the synthesized mesoporous silica are functionalized with silane molecules containing the functional group of interest. The distribution of grafted molecules is not as uniform as for the co-condensation route.[13–15] However, the grafted mesoporous silicas remain ordered when grafting at higher concentrations, whereas attempting co-condensation at high alkoxysilane concentrations generally results in a breakdown in the mesoporous silica structure.[12,14] One common method of post-synthetic functionalization involves treating calcined mesoporous silicas with functional organoalkoxysilanes.[9,16–21] The silanol groups on the mesoporous silicas are used to covalently bond the organosilane in the presence of solvent, thereby resulting in a functionalized mesoporous silica that retains its native structure.[22]

Research into amine-modified adsorbent materials has become popular since the functional group provides efficacy for carbon dioxide adsorption.[19] Post synthetic grafting of amine molecules on siliceous materials results in bifunctional materials[23] that have chemisorption potential for a wide range of light gases.[19,24–26] It has been previously shown[27–30] that due to the hydroxyl groups on MCM-41, the material exhibits a high capacity for basic gases such as ammonia. The addition of amine and carbonyl sites to the material should provide it with the potential to chemisorb both acidic and basic gases.[31–36]

In this study, different organoalkoxysilane molecules are grafted onto MCM-41. These contribute carbonyl and amine functional groups to enhance the removal of ammonia and sulfur dioxide from air. Ammonia is used as a representative basic molecule and sulfur dioxide is used as an acidic molecule to optimize the interactions between the bifunctional adsorbent and the light gases.

5.2 Experimental Methods

Materials

To make MCM-41, tetramethylammonium hydroxide pentahydrate (97 %), tetramethylammonium silicate solution (99.99 %, 15–20 wt % in water), and sulfuric acid (95.0–98.0 %) were purchased from Sigma-Aldrich. Hexadecyltrimethylammonium chloride (25 %) in water was purchased from Pfaltz and Bauer. A solution of ammonium hydroxide (29 wt %) in water and Cab-O-Sil M5 were purchased from Fisher Scientific.

Four organoalkoxysilanes were used for grafting. Five mL of nitrogen flushed 3-(aminopropyl)triethoxysilane (APTES) was purchased from Fisher Scientific. Methacryloxpropyl-trimethoxysilane (MAPS, 98 %), 3-(triethoxysilyl)propyl isocyanate (isocyanate, 95 %), and 3-(trimethoxysilyl)propyl urea (urea, 97 %) were purchased from Sigma-Aldrich.

For light gas analysis, cylinders of 1500 ppm_v ammonia in helium, 500 ppm_v of sulfur dioxide in air, ultra high purity helium, and zero air were purchased from A-L Compressed Gas.

MCM-41 synthesis

Hexagonally-ordered MCM-41 with a 37 Å pore was synthesized according to a procedure described in a previous study.[27] The as-synthesized material was calcined by heating in air from room temperature to 540 °C at 1 °C/min and holding at 540 °C for 10 hours.

Organoalkoxysilane Grafting

Organoalkoxysilanes were chosen for grafting based on their functional groups. For ammonia and sulfur dioxide removal, molecules were chosen with carbonyl and amine groups, respectively. Figure 5.1 shows the molecular structure of the organoalkoxysilanes chosen. Table 5.1 summarizes the number of carbonyl and amine

groups present in each molecule. The reaction mechanism for grafting the alkoxysilanes onto MCM-41 is given in Figure 5.2. The reaction involves hydroxyl groups on the MCM-41 interacting with the organoalkoxysilane molecule. Cleavage of the C-O bond results, which produces organoalkoxysilane-grafted MCM-41 and methanol or ethanol, depending on the alkoxysilane present in the reaction.[8] The silane chemistry is the same for all molecules.

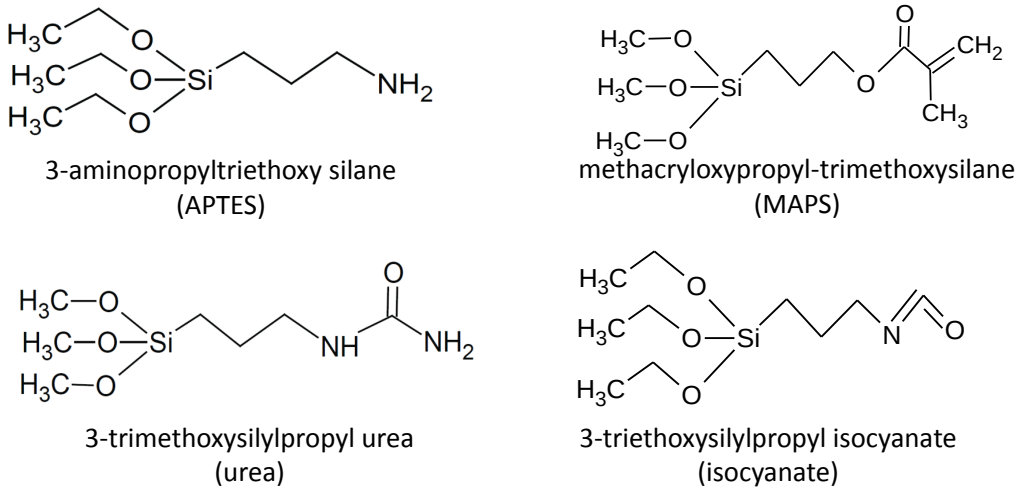

Figure 5.1 Molecular structures for grafted organoalkoxysilanes.

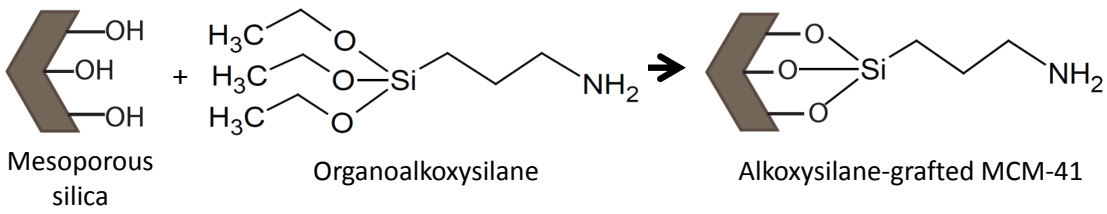

Figure 5.2 Silane grafting reaction.

MCM-41 was grafted with the organoalkoxysilanes under an inert environment in a 250 mL Schlenk flask. Calcined MCM-41 and 125 mL of ethanol were added to the flask, which was then flushed with dry nitrogen for 15 minutes while stirring. An amount of organoalkoxysilane was added as given by the weight percentage in Table 1. The sample was stirred at room temperature for 24 hours under an inert environment and then was recovered via vacuum filtration. The filtered sample was washed with deionized water to remove excess solvent and air-dried overnight.

All samples summarized in Table 1 have 2 moles of each functional groups per kg MCM-41. This was obtained by adjusting the wt % of the organoalkoxysilane grafted onto MCM-41. Two urea-MCM-41 samples were produced. Urea-MCM-41 has 2 mol amine groups/kg MCM-41 and 1 mol carbonyl groups/kg MCM-41, and urea(2x)-MCM-41 has 2 mol carbonyl groups/kg MCM-41 and 4 mol amine groups/kg MCM-41. An additional sample was synthesized using a double impregnation technique to graft 2 mol/kg APTES and 2 mol/kg isocyanate onto MCM-41. In this instance, 2 mol/kg isocyanate was first grafted onto MCM-41 following the previously described procedure. After this sample was recovered, it was then grafted with 2 mol/kg APTES to produce the APTES-isocyanate-MCM-41.

Materials characterization

Textural characterization

Adsorption isotherms were measured using a Micromeritics ASAP 2020 at -196 °C with nitrogen as the analysis gas. Prior to measurement, approximately 0.1 g of each sample was degassed with heating to 50 °C and vacuum to 10 μbar. After reaching 10 μbar, the samples were heated to 70 °C under vacuum for an additional 6 hours.

X-ray diffraction (XRD)

XRD spectra were used to confirm the long range structure of the native and impregnated MCM-41 samples. The spectra were measured using a Scintag X1h/h automated powder diffractometer with Cu target, a Peltier-cooled solid-state detector,

Table 5.1: Molecules grafted onto MCM-41 and experimental conditions for grafting. All molecule amounts correspond to 1 g MCM-41

Grafted Molecule (Abbreviation)	Carbonyl groups	Amine groups	Molec. Amt. (mL)	wt % in sample
3-aminopropyltriethoxy silane (APTES)	0	1	0.48	31
3-trimethoxysilylpropyl urea (urea)	1	2	0.19	18
3-trimethoxysilylpropyl urea (urea(2x))	1	2	0.39	31
3-triethoxysilylpropyl isocyanate (isocyanate)	1	1	0.50	33
methacryloxypropyl-trimethoxysilane (MAPS)	1	0	0.24	20

a zero background Si(5 1 0) support, and with a copper X-ray tube as the radiation source. Spectra were collected from 1.2 to 7 degrees two θ using a step size of 0.02 degrees.

X-ray photoelectron spectroscopy (XPS)

XPS was performed using a PHI Versaprobe XPS Microprobe analysis system manufactured by Physical Electronics, Inc. The apparatus was equipped with a monochromatic Al K(α) X-ray source (E = 1486.6 eV). Spectra were collected over binding energies ranging from 1300 to 100 eV, with high resolution spectra taken of carbon, silicon, oxygen, and nitrogen. The pass energy was set to 23.5 eV for determination of atomic ratios and binding energies were referenced to the oxygen 1s peak.[37]

Light gas capacity

Equilibrium capacities for room temperature light gas adsorption of both ammonia and sulfur dioxide were measured for all samples using a breakthrough apparatus, a schematic of which is given in Chapter 1 and Furtado et al.[27,36] Prior to analysis, all samples were regenerated under vacuum using a vacuum oven at 60 °C for 2 hours.

To eliminate the possibility of side reactions with the carrier gas, ammonia breakthrough tests were conducted using 1500 ppm_v ammonia pre-mixed with dry helium. The concentration of ammonia fed to the adsorbent bed was kept constant at 1133 mg/m^3. Before analysis, regenerated samples were equilibrated for 1 hour in 10 sccm helium.

Pre-mixed sulfur dioxide in air was used for SO_2 breakthrough testing to determine whether oxygen or humidity affects the samples. The concentration of sulfur dioxide in dry air was kept constant at 1428 mg/m^3 (500 ppm_v). Samples tested under dry conditions were equilibrated in 10 sccm dry helium for 1 hour prior to analysis. The samples tested under humid conditions were equilibrated in 10 sccm air at 70 %RH for 1 hour before testing. After equilibration under either dry or humid conditions, the samples were analyzed using the pre-mixed sulfur dioxide in dry air.

The capacity of the adsorbent material, n (mol ammonia/kg adsorbent), was calculated via material balance using

$$n = \frac{F}{m} \int_0^\infty (c_0 - c)\, dt \tag{5.1}$$

where c_0 is the feed molar concentration, and c is the effluent concentration at time t. The volumetric flow rate of gas through the adsorbent bed, F, was adjusted to yield a breakthrough time of approximately one hour. The mass of the sample, m, was approximately 10 mg and was contained in a small cylindrical adsorbent bed with an internal diameter of 4 mm. The capacities calculated using the breakthrough apparatus have a standard deviation on the order of 3 %. The capacities of different batches of the grafted samples have larger standard deviations, on the order of 20 %, due to variations in the distribution of grafted molecules throughout the silica substrate.

To test for reaction between adsorbate and adsorbent, select samples were first analyzed for ammonia or sulfur dioxide capacity, purged with helium or air for 10 minutes using a 10 sccm flow rate, vacuumed for 30 minutes, and then re-tested for ammonia or sulfur dioxide capacity. The vacuum pump used after the desorption step was an Edwards vacuum pump model RV5 that is capable of producing a vacuum of $1.5\text{x}10^{-3}$ torr.

5.3 Results

Material characterization

Nitrogen isotherms for the parent and grafted MCM-41 materials are shown in Figure 5.3. Similar to the parent isotherm, all grafted samples exhibit type IV isotherms indicative of mesoporous materials. The hysteresis loops represent capillary condensation in the mesopores.

Surface areas and pore volumes are compared in Table 5.2. Organoalkoxysilane grafting results in a decrease in surface area compared to the parent material. The decrease in surface area corresponds to a decrease in pore volume when compared to

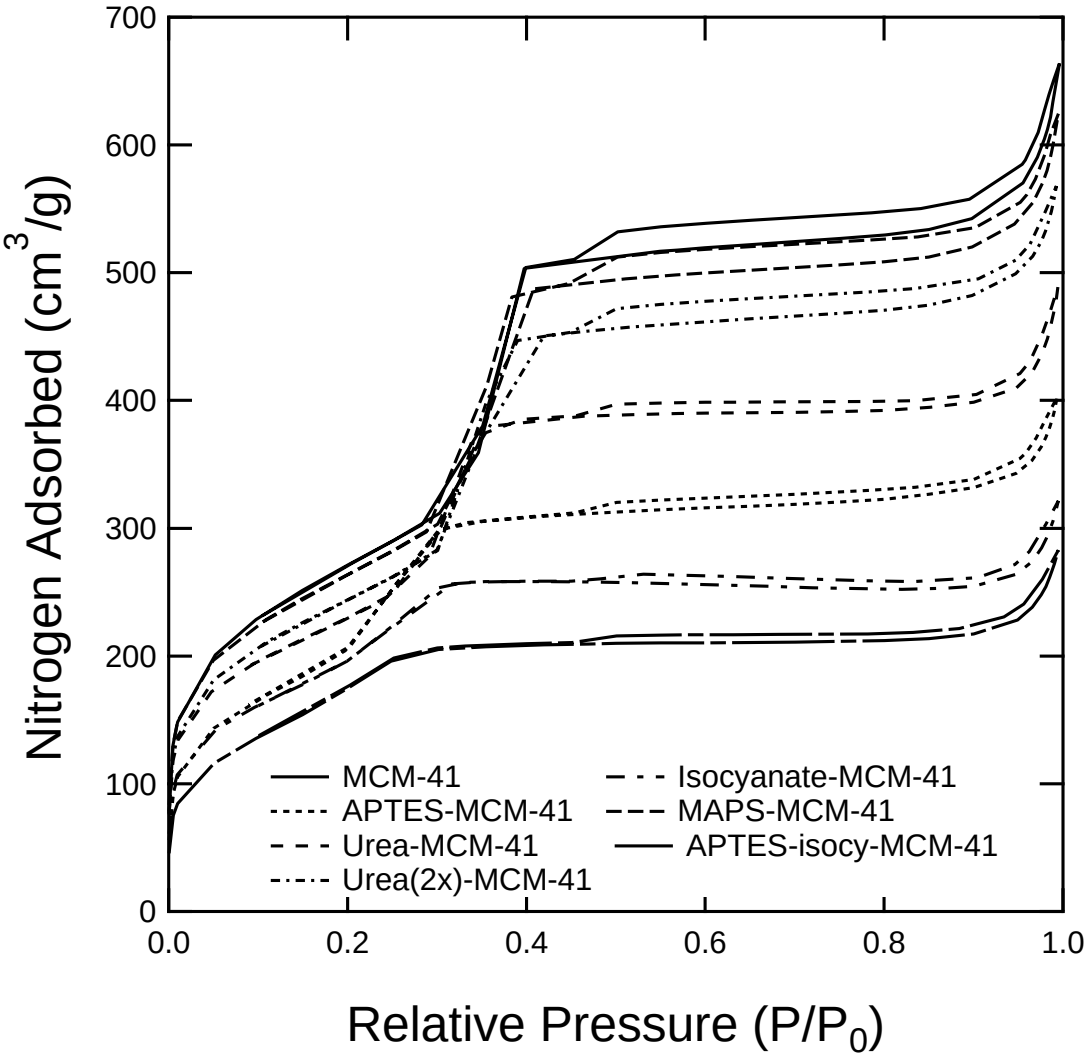

Figure 5.3 Nitrogen isotherms for parent MCM-41 and grafted materials.

the parent material. This is consistent with grafting a large molecule within the pores of an ordered MCM-41 material. The APTES-isocyanate-MCM-41 has undergone two grafting steps, and the surface area and pore volume of this material is less than the other materials, which is consistent with a reduction in surface area with each grafting step.

Table 5.2: BET surface areas and pore volumes of grafted samples.

Sample	BET SA (m^2/g)	V_{pore} (cm^3/g)
MCM-41	952	1.03
APTES-MCM-41	711	0.62
urea-MCM-41	856	0.88
urea(2x)-MCM-41	805	0.76
isocyanate-MCM-41	681	0.50
MAPS-MCM-41	925	0.96
APTES-isocy-MCM-41	603	0.44

The X-ray diffraction patterns for the parent and grafted materials are compared in Figure 5.4. According to the XRD spectrum, parent MCM-41 is highly ordered as indicated by the five peaks characteristic of the hexagonally ordered MCM-41 structure.[27] XRD spectra of the grafted samples show that the corresponding MCM-41 peaks are intact, but shifted to smaller angles. This is due to an expansion in the unit cell after grafting the organoalkoxysilanes onto the hexagonally ordered MCM-41.[31]

Ammonia adsorption

The ammonia capacities of the parent MCM-41 and the organoalkoxysilane grafted samples are compared in Table 5.3. The samples are listed in order of increasing carbonyl content, since the purpose of including the carbonyl functional group is to enhance ammonia capacity.

As mentioned previously,[27] the parent MCM-41 exhibits an ammonia capacity of 2 moles ammonia/kg sample. In grafted samples without carbonyl groups (i.e., the

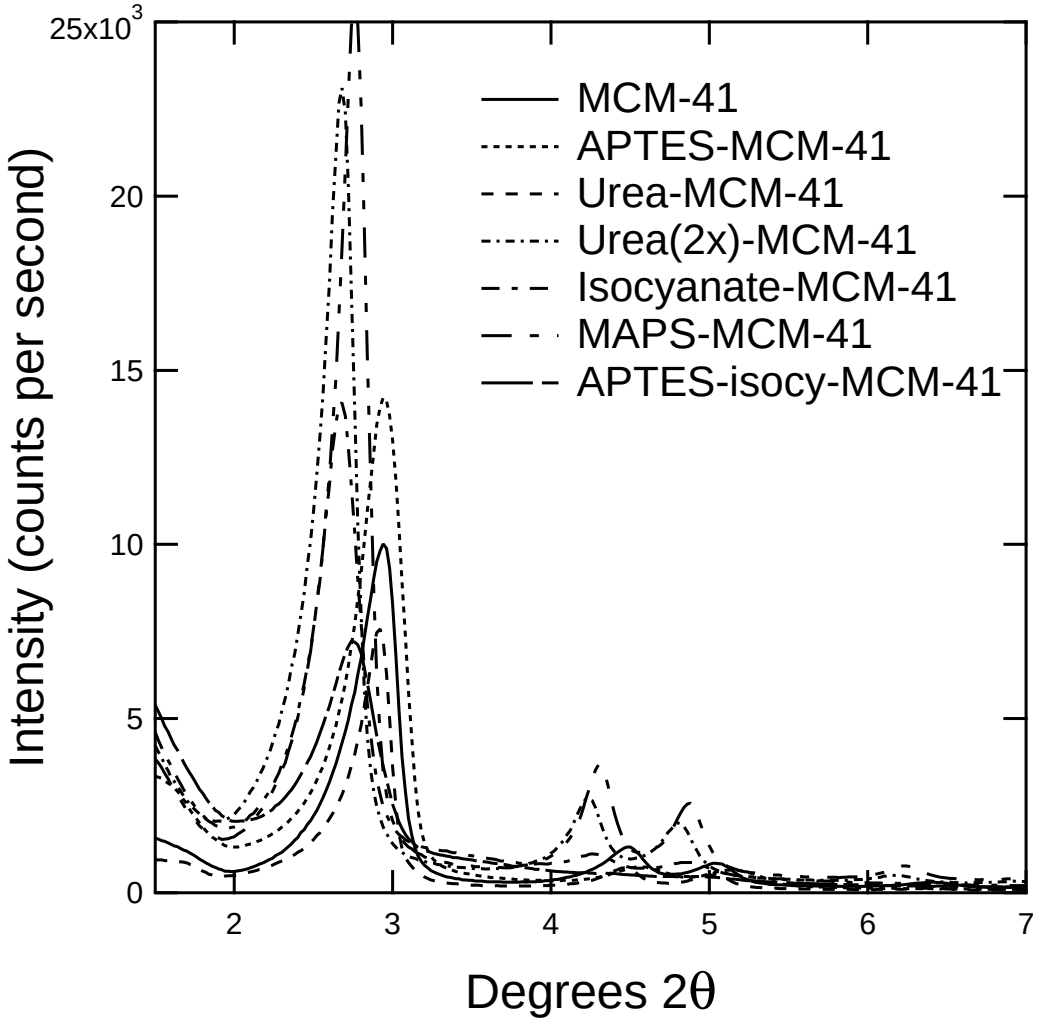

Figure 5.4 X-ray diffraction patterns for parent MCM-41 and grafted materials.

Table 5.3: Ammonia capacities for all samples in order of increasing carbonyl groups

Sample	mol carbonyl groups /kg MCM-41	mol amine groups /kg MCM-41	NH_3 capacity (mol/kg sample)	NH_3 capacity (mol/kg MCM-41)
MCM-41	0	0	2.00	2.00
APTES-MCM-41	0	2	1.34	1.95
urea-MCM-41	1	2	5.55	6.78
urea(2x)-MCM-41	2	4	6.21	9.00
APTES-isocy-MCM-41	2	4	5.90	11.5
isocyanate-MCM-41	2	2	9.75	14.6
MAPS-MCM-41	2	0	6.41	5.88

material with grafted APTES), the presence of amine groups decreases the ammonia capacity over that of parent MCM-41, viz., 1.34 mol/kg compared to 2 mol/kg. This decrease in capacity is a result of calculating capacity per kg sample rather than per kg MCM-41. The last column in Table 3 shows the ammonia capacity for the samples with units of mol NH_3/kg MCM-41. A comparison of the ammonia capacities of APTES-MCM-41 and parent MCM-41 are within experimental error (1.95 mol/kg compared to 2.00 mol/kg). Consequently, grafting amine groups onto the siliceous support does not measurably decrease the ammonia capacity compared to that of the parent.

In general, the presence of carbonyl groups in a grafted molecule enhances the ammonia capacity. Two urea-MCM-41 samples were prepared, corresponding to 1 and 2 mol carbonyl groups/kg MCM-41. The urea-MCM-41 sample with twice the amount of urea molecules grafted onto MCM-41 has a larger ammonia capacity. The isocyanate-MCM-41 and MAPS-MCM-41 samples have larger capacities (9.75 mol/kg and 6.41 mol/kg) compared to the urea grafted materials. The shapes of the breakthrough curves for these samples with carbonyl groups indicate that reactions are occurring between ammonia and the carbonyl functional groups; the ammonia breaks through quickly, but it takes a long time for the ammonia to fully saturate the sample, which results in a long tail. This is true for all samples containing carbonyl functional groups.

To better understand the reactions taking place, additional analyses were performed on the two samples with the highest ammonia capacities, MAPS-MCM-41 and isocyanate-MCM-41. XPS, which involves a high vacuum, was used to analyze these samples before and after exposure to ammonia. There was no visible shifting of high resolution carbon or nitrogen peaks when comparing the exposed and unexposed samples, which would indicate the formation of bonds between ammonia and the functional carbonyl groups on the grafted molecule. Interestingly, as summa-

Table 5.4: XPS atomic ratios for parent and ammonia-exposed isocyanate-MCM-41 and MAPS-MCM-41 samples.

Atomic Ratio	Isocyanate-MCM-41		MAPS-MCM-41	
	parent	NH_3 exposed	parent	NH_3 exposed
Si/O	0.37	0.40	0.39	0.41
Si/C	4.90	3.10	8.80	10.4
Si/N	18.0	52.4	—	—

rized in Table 5.4, the concentration of nitrogen in the isocyanate-MCM-41 decreases after exposure to ammonia. Also, there is no measurable nitrogen present in the MAPS-MCM-41 either before or after ammonia exposure.

For additional analysis, the mass spectrometer used in the breakthrough experiments was used to perform a scan across mass-to-charge ratios from 10 to 500 at intervals of 0.006 seconds. This technique generates peaks that correspond to compounds being removed from the system at different time points during the reaction. As a control, the parent MCM-41 was also analyzed using this method. All peaks identified during the analysis remain at or below an m/z of 40, which is indicative of only small molecules being present in the effluent. The majority of these peaks correspond to residual gases in the vacuum system of the mass spectrometer, as was found via the control MCM-41 analysis. Based on the peak positions shared by all three samples, oxygen, nitrogen, and ammonia were present in the effluent. No other distinct peaks were found for both the isocyanate and MAPS samples. Interestingly, MAPS-MCM-41 gave a small peak at an m/z of 40 that was not present in the MCM-41 or isocyanate-MCM-41 samples. However, purging a fresh, regenerated sample of MAPS-MCM-41 with helium under vacuum also gave this same small peak, which likely indicates some instability in the grafted MAPS molecule, perhaps it breaking apart at the carbonyl carbon to liberate a small amount of hydrocarbon from the solid.

The doubly-grafted APTES-isocyanate-MCM-41 has a lower ammonia capacity than isocyanate-MCM-41 but a higher ammonia capacity than APTES-MCM-41. Because the APTES molecule is grafted after the isocyanate molecules, the amine groups in the grafted APTES molecules could shield the carbonyl groups on the isocyanate from reacting as efficiently with ammonia. They could also be reacting with carbonyl groups in the grafted isocyanate molecules and thus reduce the ammonia capacity. Based on the analysis of the sulfur dioxide capacity of this sample in the following section, the shielding effect is most likely the reason for the decrease in ammonia capacity compared to isocyanate-MCM-41. However, some of the carbonyl groups are exposed enough to react with ammonia since the ammonia capacity is much higher than those of the parent or APTES-grafted MCM-41. Consequently, by grafting different molecules onto the siliceous support, it is possible to tailor the ammonia capacity of the samples.

Sulfur dioxide adsorption

The sulfur dioxide capacities of all grafted samples are compared in Table 5.5. The samples are listed in order of increasing amine content. In this system, SO_2 is much more difficult to remove from carrier gas than NH_3 since the parent MCM-41 has minimal sulfur dioxide capacity. Consequently, the capacities in this table are lower than the corresponding ammonia capacities. Under dry conditions, the grafted APTES-MCM-41 has the highest sulfur dioxide capacity of 0.85 mol/kg sample or 1.24 mol/kg MCM-41. When compared on a per silica basis, the APTES-MCM-41 material shows about a 40 times increase in capacity compared to the parent MCM-41. Prehumidification at 70 %RH in air does not influence the sulfur dioxide capacities compared to testing under dry conditions. The APTES-isocyanate-MCM-41 has a capacity of 1.23 mol/kg MCM-41, which is comparable to that of APTES-MCM-41. Thus, the amines on the APTES-isocyanate-MCM-41 sample are available for reaction with SO_2 and are not bound to the carbonyl active sites on the isocyanate

molecules that are also present in this sample.

It is evident from the table that the carbonyl groups do not enhance SO_2 capacity and actually hinder this capacity in samples with both carbonyl and amine functional groups. In general, all grafted molecules that have a carbonyl group mask the effectiveness of the amine groups. This includes both urea-grafted and isocyanate-grafted samples. The sulfur dioxide capacities for these materials are statistically similar to that of the parent MCM-41. As expected, grafting only carbonyl groups onto the siliceous support using MAPS does not increase the sulfur dioxide capacity above that of the parent.

The presence of carbonyl groups on the same grafted molecule with the amine groups reduces the efficiency of sulfur dioxide chemisorption by shielding the amines from interaction with SO_2. However, additional grafting of APTES onto the isocyanate-MCM-41 sample improves the sulfur dioxide capacity. Consequently, grafting different functional groups onto MCM-41 by using different molecules, rather than grafting one molecule with multiple functional groups, provides the ability to tailor adsorbent materials for better removal of both acidic and basic gases.

Testing for reaction

The reactions presented for ammonia and sulfur dioxide involve the interaction of these molecules with functional groups on the organoalkoxysilanes. The capacities presented in the previous sections were single pass capacities; they were calculated by exposing regenerated, fresh adsorbent containing functional groups available for reaction to the gas. To help verify the types of adsorption promoted by the grafted functional groups, samples containing a single functional group (APTES and MAPS) were first analyzed for ammonia or sulfur dioxide capacity, purged with helium or air for 10 minutes while monitoring the amount of ammonia or sulfur dioxide desorbed, vacuumed for 30 minutes, and then re-tested for ammonia or sulfur dioxide capacity. In this way, it is possible to determine whether the adsorbed ammonia or sulfur

Table 5.5: Sulfur dioxide capacities for all samples in order of increasing amine groups

Sample	mol amines	mol carbonyls	SO_2 capacity dry		SO_2 capacity 70 %RH	
	/kg MCM-41	/kg MCM-41	mol/kg sample	mol/kg MCM-41	mol/kg sample	mol/kg MCM-41
MCM-41	0	0	0.03	0.03	0.03	0.03
MAPS-MCM-41	0	2	0.14	0.18	0.09	0.11
urea-MCM-41	2	1	0.05	0.06	0.09	0.11
isocyanate-MCM-41	2	2	0.06	0.09	0.11	0.16
APTES-MCM-41	2	0	0.85	1.24	0.88	1.28
urea(2x)-MCM-41	4	2	0.08	0.12	0.17	0.24
APTES-isocy-MCM-41	4	2	0.63	1.23	0.60	1.16

dioxide is able to be easily removed from the system during the purging step. If the capacities of the purge step and the second breakthrough are low, then minimal light gas can be removed from the system, and a reaction is indicated to have occurred between the functional groups and the light gas of interest. However, if large amounts of gas are removed during the purging step and the second breakthrough capacity is high, then the light gas is physically adsorbed onto the adsorbent.

Figure 5.5 summarizes the ammonia capacities for the MAPS-MCM-41 sample. The first pass capacity is high: 6.4 mol/kg sample. The 10 minute desorption step using the helium purge shows that approximately 0.45 mol/kg ammonia is desorbed from the sample. This is consistent with desorption of physically adsorbed ammonia throughout the MCM-41 support, since the parent MCM-41 has an ammonia capacity of 2 mol/kg and most of that can be desorbed during the desorption step. After pulling a high vacuum for 30 minutes, the second breakthrough capacity, at 11.20 mol/kg sample, is even higher than the first capacity. As shown in Figure 5.5, successive adsorption and desorption cycles generally increase the ammonia capacity. The fourth adsorption was performed after vacuuming overnight for 16 hours. To double check the validity of these results, a second batch of sample was synthesized according to the same synthesis procedure. A breakthrough test was performed on the new sample after pulling a vacuum overnight before the first run. The calculated capacities for this sample were 31.3 mol/kg and 30.4 mol/kg for the first and second adsorption steps.

The sulfur dioxide capacities for APTES-MCM-41 are shown in Figure 5.6. Based on the desorption capacity of 0.09 mol/kg, most of the adsorbed sulfur dioxide is complexed on amine sites on the adsorbent and is therefore not removed during the desorption step. The capacity calculated from the second breakthrough test is also small, 0.12 mol/kg, which is consistent with active amine sites being consumed during reaction in the first breakthrough test.

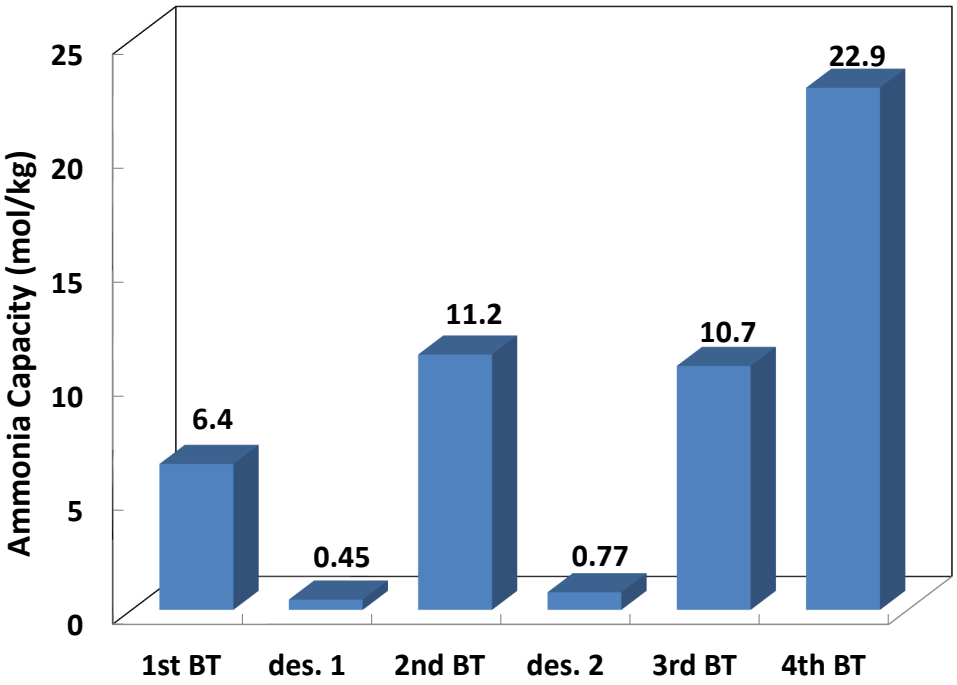

Figure 5.5 Ammonia chemisorption on MAPS-MCM-41.

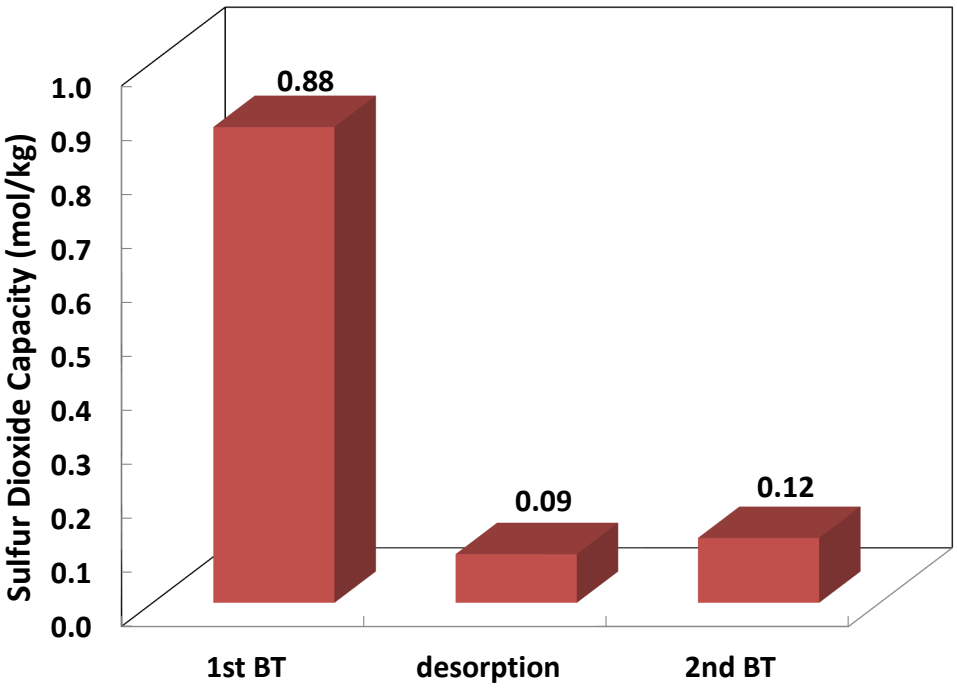

Figure 5.6 Sulfur dioxide chemisorption on APTES-MCM-41.

5.4 Discussion

In this section, we consider the possible mechanisms for the retention of the sulfur dioxide and ammonia molecules by the samples based on experimental evidence and reports in the literature. Our experiments involved gas breakthrough analysis, mass spectrometry of effluents during the gas capacity studies, and XPS of samples. There are three possible mechanisms for the retention and fate of the ammonia and sulfur dioxide molecules on the organoalkoxysilane-silica composite samples that we wish to distinguish: (1) physically adsorbed molecules associating with the polar, hydroxylated silica surface and grafted molecules, (2) intact chemisorbed molecules or chemisorbed molecules that react with all reaction products retained by a sample, and (3) chemisorbed molecules that react with some or all of the products eluted as the result of reactions consuming the grafted molecules or catalytic reactions.

For sulfur dioxide, the data and literature provide a straightforward interpretation of retention by the sample. For the amine-grafted APTES sample, the first breakthrough capacity is modest, with very little sulfur dioxide removed during the subsequent purge, and very little additional retained on the second breakthrough. In this case, the sulfur dioxide molecules have associated strongly with the amine groups. In the presence of amines, sulfur dioxide can form 1:1 charge-transfer complexes with electrons from nitrogen transferring to antibonding orbitals on the sulfur.[32] This complexation reaction provides the basis for chemisorption of sulfur dioxide onto the amine-grafted MCM-41 samples. The sulfur dioxide molecule is retained intact by the sample with no elution of reaction products. For samples with a grafted carboxylate group, sulfur dioxide retention is still enhanced over the parent silica support, although the extent of this retention is low; what is retained is likely held by physical adsorption.

The cause of ammonia retention on the grafted samples is not as straightforward as that of sulfur dioxide. For ammonia, grafted amine functional groups do

not improve, nor should they be expected to improve, the retention of ammonia by the silica support. Chemisorption of ammonia on silica is not promoted by amines. Retention of ammonia by the carbonyl-impregnated samples is more complex. The gas capacity experiments show a high capacity for the first breakthrough, measurable desorption during the regenerative helium purge and vacuum, and additional breakthrough capacities that exceed the first breakthrough capacity for the parent silica support. The multiple high capacities are an indication of significant physical adsorption occurring in these samples. XPS provides the interesting result that some nitrogen is lost from the isocyanate-grafted sample from exposure to ammonia. This indicates that a chemical reaction has occurred with removal of some of the nitrogen in the effluent. However, no additional peaks above a threshold value were found in mass spectrometry scans, suggesting either that the reaction product was present at too low a concentration to be detected or that the reaction product was N_2, which was obscured by the large residual nitrogen peak.

Physical adsorption of ammonia can be expected to involve its hydrogen bonding, and this would be promoted by the presence of the carbonyl group. The last column in Table 5.6 summarizes the number of ammonia molecules that must be interacting with each carbonyl group to achieve the corresponding capacity for each sample if physical adsorption alone were responsible for the large ammonia capacities. It is obvious that each carbonyl group would need to promote the adsorption of a large number of ammonia molecules. However, it should be pointed out that water adsorption on many common adsorbents shows similar capacities (>20 mol/kg) and involves extensive hydrogen bonding. The development of large clusters of hydrogen bound water molecules during adsorption is understood for both activated carbons[40] and zeolites.[41–44] While ammonia does not hydrogen bond as perfectly as water, such clusters should still be expected to form, especially when promoted by chemical functionalities such as carbonyl groups. After ammonia adsorption, the samples used in

XPS analysis were exposed to high vacuum prior to beginning that study, and it is possible that the large clusters of ammonia molecules were removed from the grafted samples before the actual analysis.

The cyclic adsorption seen from the first MAPS-MCM-41 samples also suggests that the ammonia is participating in hydrogen bonding with the carbonyl groups, rather than chemisorbing with them. If the carbonyl groups had been chemisorbing with ammonia, then each successive ammonia capacity should be lower than that calculated from the previous run. The fact that the first sample showed increasing ammonia capacities is most likely due to hydrogen bonded water being present on the material and taking up the carbonyl active sites that can also participate in hydrogen bonding with ammonia. After pulling a vacuum for 30 minutes after the desorption analysis, more of the water is removed, which results in an increase in ammonia capacity as calculated by the second breakthrough. The second sample that was found to have an ammonia capacity of 31 mol/kg was analyzed only after fully removing the adsorbed water from the sample by exposing it to a high vacuum overnight. In this case, the first and second breakthrough capacities are similar and very high.

From the standpoint of chemisorption, the high ammonia capacities might be thought to be indicative of the nucleophilic nitrogen in ammonia molecules reacting with the electrophilic carbon in the carbonyl group, as shown in the reaction in Figure 5.7.[45] The formation of the hemiaminal intermediate provides an additional hydroxyl group that could interact with ammonia and boost the chemisorption potential of the material similar to the interactions of ammonia with the hydroxyl groups on the silica substrate. Assuming that one ammonia molecule interacts with one carbonyl group according to the reaction in Figure 5.7, and considering the resulting theoretical capacities in Table 5.6, it is obvious that the actual capacities are much higher than the theoretical capacities suggested by the proposed reaction. Also, if

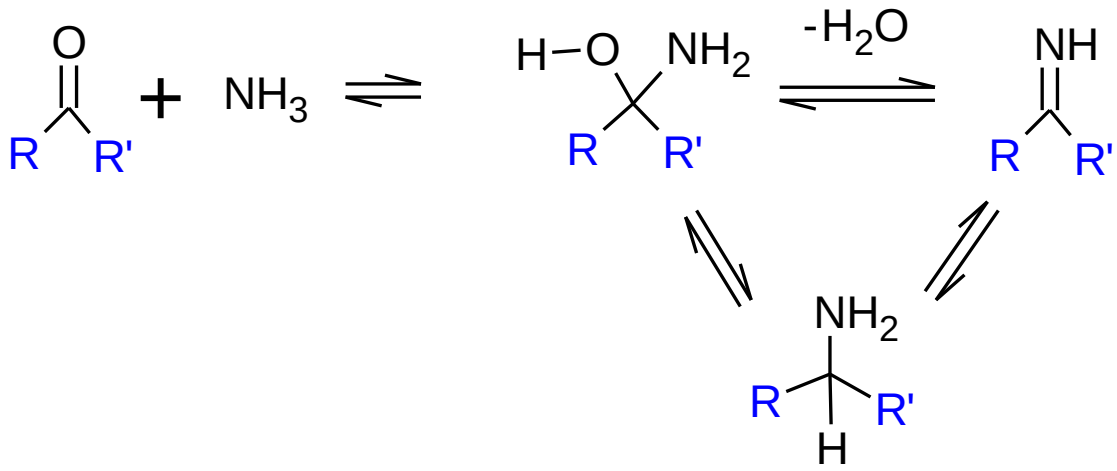

Figure 5.7 A proposed reaction schematic for ammonia and carbonyl groups.

the ammonia molecules were participating in the reaction proposed in Figure 5.7, in which reacted nitrogen remains bound to the solid phase, there should be an increase in nitrogen present in the ammonia-exposed samples when compared to the unexposed materials. XPS showed a decrease in nitrogen content.

Table 5.6: Comparison of theoretical and actual ammonia capacities in grafted samples.

Sample	NH_3 capacity (mol/kg sample)		Number of NH_3 molecs.
	Theoretical	Actual	/carbonyl group
MCM-41	2.00	2.00	—
urea-MCM-41	2.82	5.55	7
urea(2X)-MCM-41	3.39	6.21	5
isocyanate-MCM-41	3.34	9.75	8
MAPS-MCM-41	3.61	22.9	15

5.5 Conclusions

A series of composite materials has been synthesized using silane chemistry to graft organoalkoxysilanes with unique functional groups onto an ordered siliceous substrate. By exploiting the chemistry of the functional groups, the biphasic materials exhibit high single pass capacities for sulfur dioxide, an acidic gas, and ammonia, a basic gas. The siliceous parent material provides initial ammonia capacity. Organoalkoxysilane molecules containing carbonyl groups provide additional ammonia capacity, and molecules containing amine groups provide sulfur dioxide capacity.

The arrangement of functional groups on the organoalkoxysilanes result in different ammonia and sulfur dioxide capacities for the grafted samples. A shielding effect is thought to occur when both carbonyl and amine functional groups are present on the same grafted molecule. Urea-MCM-41 samples are dominated by the carbonyl groups on the urea and thus exhibit high ammonia capacities but low sulfur dioxide capacities, despite the fact that there are two amine groups per urea molecule. The

APTES molecule imparts the highest sulfur dioxide capacity of all grafted molecules. MAPS-MCM-41 has the highest ammonia capacity since it has only a single carbonyl functionality to enhance hydrogen bonding. The amine functional group enhances the sulfur dioxide capacity by forming charge-transfer complexes with SO_2. The carbonyl groups enhance the capacity for ammonia through hydrogen bonding.

Grafting two molecule types onto MCM-41 is one way to tailor the adsorbent for the removal of both gases. APTES-isocyanate-MCM-41 has a high sulfur dioxide capacity, which is comparable to that of APTES-MCM-41. Although not as high as for MAPS-MCM-41, the ammonia capacity of this sample is still extremely high. Both capacities are much higher than those of commercial adsorbents. Grafting different amounts of these molecules onto MCM-41 provides the ability to tailor the resulting acidic and basic gas capacities for this bifunctional adsorbent material.

References

[1] C.T. Kresge, M.E. Leonowicz, W.J. Roth, J.C. Vartuli, J.S. Beck. Ordered mesoporous molecular sieves synthesized by a liquid crystal template mechanism. *Nature*, 1992, **359**, 710-712.

[2] M. Shengqian, L. Meng. Energy-related applications of functional porous metal-organic frameworks. *Pure Appl. Chem.*, 2011, **83**, 167-188.

[3] G. W. Peterson, G. W. Wagner, J. H. Keller, J. A. Rossin. Enhanced cyanogen chloride removal by the reactive zirconium hydroxide substrate *Ind. Eng. Chem. Res.*, 2010, **49**, 11182-11187.

[4] K. Tanabe, T. Yamaguchi. Acid-base bifunctional catalysis by ZrO2 and its mixed oxides. *Catal. Today*, 1994, **20**, 185-198.

[5] F. Hoffmann, M. Cornelius, J. Morell and M. Froba. Silica-based mesoporous organic-inorganic hybrid materials. *Angew. Chem., Int. Ed.*, 2006, **45**, 3216-3251.

[6] B. Marler, U. Oberhagemann, S. Vortmann, H. Gies. Influence of the sorbate type on the XRD peak intensities of loaded MCM-41. *Microporous Mater.*, 1996, **6**, 375-383.

[7] E. P. Plueddemann, G. L. Stark. Catalytic and electrokinetic effects in bonding through silanes. *Modern Plastics*, 1974, **51**, 74-84.

[8] N. R. E. N. Impens, P. van der Voort, E. F. Vansant. Silylation of micro-, meso- and non-porous oxides: a review. *Microporous Mesoporous Mater.*, 1999, **28**, 217-232.

[9] N. Gartmann, D. Bruhwiler. Controlling and imaging the functional-group distribution on mesoporous silica. *Angew. Chem., Int. Ed.*, 2009, **48**, 6354-6356.

[10] M. Etienne, B. Lebeau, A. Walcarius. Organically-modified mesoporous silica spheres with MCM-41 architecture. *New J. Chem.*, 2002, **26**, 384-386.

[11] A. Walcarius, C. Delacote. Rate of access to the binding sites in organically modified silicates. 3. Effect of structure and density of functional groups in mesoporous solids obtained by the co-condensation route. *Chem. Mater.*, 2003, **15**, 4181-4192.

[12] R. Richer, L. Mercier. Direct synthesis of functionalized mesoporous silica by non-ionic alkylpolyethyleneoxide surfactant assembly. *Chem. Commun.*, 1998, 1775-1776.

[13] M. H. Lim, A. Stein. Comparative studies of grafting and direct syntheses of inorganic-organic hybrid mesoporous materials. *Chem. Mater.*, 1999, **11**, 3285-3295.

[14] J. M. Rosenholm, M. Linden. Wet-chemical analysis of surface concentration of accessible groups on different amino-functionalized mesoporous SBA-15 silicas. *Chem. Mater.*, 2007, **19**, 5023-5034.

[15] J. M. Rosenholm, T. Czuryszkiewicz, F. Kleitz, J. B. Rosenholm, M. Linden. On the nature of the bronsted acidic groups on native and functionalized mesoporous siliceous SBA-15 as studied by benzylamine adsorption from solution. *Langmuir*, 2007, **23**, 4315-4323.

[16] S. Yoo, J. D. Lunn, S. Gonzalez, J. A. Ristich, E. E. Simanek, D. F. Shantz. Engineering nanospaces: OMS/dendrimer hybrids possessing controllable chemistry and porosity. *Chem. Mater.*, 2006, **18**, 2935-2942.

[17] E. J. Acosta, C. S. Carr, E. E. Simanek, D. F. Shantz. Engineering nanospaces: Iterative synthesis of melamine-based dendrimers on amine-functionalized SBA-15 leading to complex hybrids with controllable chemistry and porosity. *Adv. Mater.*, 2004, **16**, 985-989.

[18] I. Shimizu, A. Yoshino, H. Okabayashi, E. Nishio, C. O'Connor. Kinetics of interaction of 3-amimopropyltriethoxysilane on a silica gel surface using elemental analysis and diffuse reflectance infrared Fourier transform spectra. *J. Chem. Soc., Faraday Trans.*, 1997, **93**, 1971-1979.

[19] B. Aziz, G. Zhao, N. Hedin. Carbon dioxide sorbents with propylamine groups-silica functionalized with a fractional factorial design approach. *Langmuir*, 2011, **27**, 3822-3834.

[20] T. Borrego, M. Andrade, M. L. Pinto, A. R. Silva, A. P. Carvalho, J. Rocha, C. Freire, J. Pires. Physicochemical characterization of silylated functionalized materials. *J. Colloid Interface Sci.*, 2010, **344**, 603-610.

[21] K. C. Vrancken, K. Possemeirs, P. Van Der Voort, E. F. Vansant. Surface modification of silica gels with aminoorganosilanes. *Colloids Surf. A: Physicochem. Eng. Aspects*, 1995, **98**, 235-241.

[22] J. A. Bae, K. C. Song, J. K. Jeon, Y. S. Ko, Y. K. Park, J. H. Yim. Effect of pore structure of amine-functionalized mesoporous silica-supported rhodium catalysts on 1-octene hydroformylation. *Microporous Mesoporous Mater.*, 2009, **123**, 289-297.

[23] F. Shang, H. Liu, J. Sun, B. Liu, C. Wang, J. Guan, Q. Kan. Synthesis, characterization and catalytic application of bifunctional catalyst: Al-MCM-41-NH(2). *Catal. Commun.*, 2011, **12**, 739-743.

[24] T. Yokoi, H. Yoshitake, T. Tatsumi. Synthesis of amino-functionalized MCM-41 via direct co-condensation and post-synthesis grafting methods using mono-, di- and tri-amino-organoalkoxysilanes. *J. Mater. Chem.*, 2004, **14**, 951-957.

[25] X. Wang, K. S. K. Lin, J. C. C. Chan, S. Cheng. Direct synthesis and catalytic applications of ordered large pore aminopropyl-functionalized SBA-15 mesoporous materials. *J. Phys. Chem. B*, 2005, **109**, 1763-1769.

[26] D. Bruhwiler. Postsynthetic functionalization of mesoporous silica. *Nanoscale*, 2010, **2**, 887-892.

[27] A. M. B. Furtado, Y. Wang, T. G. Glover, M. D. LeVan. MCM-41 impregnated with active metal sites: synthesis, characterization, and ammonia adsorption. *Microporous Mesoporous Mater.*, 2011, **142**, 730-739.

[28] B. A. Morrow, I. A. Cody. Infrared studies of reactions on oxide surfaces. 6. active sites on dehydroxylated silica for the chemisorption of ammonia and water. *J. Phys. Chem.*, 1976, **80**, 1998-2004.

[29] B. A. Morrow, I. A. Cody, L. S. M. Lee. Infrared studies of reactions on oxide surfaces. IV. the structure of chemisorbed ammonia on silica. *J. Phys. Chem.*, 1975, **79**, 2405-2408.

[30] S. Kittaka, M. Morimura, S. Ishimaru, A. Morino, K. Ueda. Effect of confinement on the fluid properties of ammonia in mesopores of MCM-41 and SBA-15. *Langmuir*, 2009, **25**, 1718-1724.

[31] S. Parambadath, V. K. Rana, D. Zhao, C. Ha. N,N'-diureylenepiperazine-bridged periodic meso organosilica for drug delivery. *Microporous Mesoporous Mater.*, 2011, **141**, 94-101.

[32] F. Cotton, G. Wilkinson, C. Murillo, M. Bochmann, Advanced Inorganic Chemistry 6^{th} ed. New York: John Wiley and Sons, Inc. 1999.

[33] H. C. Kolb, M. G. Finn, K. B. Sharpless. Click chemistry: Diverse chemical function from a few good reactions. *Angew. Chem., Int. Ed.*, 2001, **40**, 2004-2021.

[34] L. Chen, D. E. Woon. A theoretical investigation of the plausibility of reactions between ammonia and carbonyl species (formaldehyde, acetaldehyde, and acetone) in interstellar ice analogs at ultracold temperatures. *J. Phys. Chem.*, 2011, **115**, 5166-5183.

[35] P. Falus, Z. Boros, G. Hornyanszky, J. Nagy, F. Darvas, L. Urge, L. Poppe. Reductive amination of ketones: novel one-step transfer hydrogenations in batch and continuous-flow mode. *Tetrahedron Lett.*, 2011, **52**, 1310-1312.

[36] A. M. B. Furtado, J. Liu, Y. Wang, M. D. LeVan. Mesoporous silicaŰmetal organic composite: synthesis, characterization, and ammonia adsorption. *J. Mater. Chem.*, 2011, **21**, 6698-6706.

[37] J.F. Moulder, W.F. Stickle, P.E. Sobol, K.D. Bomben, Handbook of X-ray Photoelectron Spectroscopy: A Reference of Standard Spectra for Identification and Interpretation of XPS Data, Chigasaki City, Japan, 2007.

[38] K. Nakanishi, P. H. Solomon, Infrared absorption spectroscopy: Second edition, Holden-Day, Inc., San Francisco, 1977.

[39] K. Nishikida, E. Nishio, R. W. Hannah, Selected applications of modern FT-IR techniques, Gordon and Breach Publishers, Australia, 1995.

[40] O. Talu and F. Meunier. Adsorption of associating molecules in micropores and application to water on carbon. *AIChE J.*, 1996, **42**, 809-819.

[41] M. G. Ahunbay. Monte carlo simulation of water adsorption in hydrophobic MFI zeolites with hydrophilic sites. *Langmuir*, 2011, **27**, 4986-4993.

[42] R. Krishna, J. M. van Baten. Hydrogen bonding effects in adsorption of water-alcohol mixtures in zeolites and the consequences for the characteristics of the Maxwell-Stefan diffusivities. *Langmuir*, 2010, **26**, 10854-10867.

[43] P. Demontis, G. Stara, G. B. Suffritti. Behavior of water in the hydrophobic zeolite silicalite at different temperatures. A molecular dynamics study. *J. Phys. Chem. B*, 2003, **107**, 4426-4436.

[44] C. Chmelik, He. Bux, J. Caro, L. Heinke, F. Hibbe, T. Titze, J. Karger. Mass transfer in a nanoscale material enhanced by an opposing flux. *PRL*, 2010, **104**, 085902 1-4.

[45] T. W. G. Solomons, C. B. Fryhle, Organic Chemistry. New York: John Wiley and Sons, Inc. 2008

CHAPTER VI

BIFUNCTIONAL ORGANOALKOXYSILANE-GRAFTED ZIRCONIUM HYDROXIDE COMPOSITE FOR ACIDIC AND BASIC GAS ADSORPTION

6.1 Introduction

Adsorbent materials designed specifically for air purification applications are in high demand. These materials can be used for numerous applications including building filtration and chemical protective masks.[1–4] Light gases can be retained within the small pores of high surface area adsorbents via physical adsorption, but they can be retained more strongly by using active basic and acidic sites to promote chemical adsorption. In order for an adsorbent material to target extreme air purification successfully, it should have the ability to remove a broad spectrum of light gases, including both acidic and basic gases, such as sulfur dioxide and ammonia.

Metal oxides such as ordered siliceous materials,[5–7] templated titanias,[8] and zirconium oxides[4, 9, 10] have been used extensively as the scaffold for composite materials. These materials generally exhibit repeating structure with long range order, high surface areas, and narrow pore size distributions that produce structured composite materials. Furtado et al.[6] took advantage of the hexagonally ordered mesoporous silica MCM-41 to produce a composite material with a metal organic phase. This material showed enhanced ammonia capacity compared to the unimpregnated silica. Other research groups have used templated metal oxides as the scaffold to produce ordered single phase materials after removal of the oxide phase. Zhang et al.[7] impregnated highly ordered and spherical silicas with carbonaceous sucrose. After removal of the siliceous phase, the carbonaceous spheres were found to be highly ordered and connected by macropores and mesopores. The base oxide material is often chosen for use in a composite material based on its individual properties. Ordered mesoporous

silicas such as MCM-41 have been found to have high capacities for basic gases.[5] Conversely, zirconium hydroxide has been found to have a high capacity for acidic gases such as sulfur dioxide.[11–14] Consequently, composite materials can be tailored for the removal of different gases by using the scaffold material to enhance the capacity for one type of gas and a grafted impregnate to enhance another.

Post synthetic grafting of amine molecules on templated metal oxide materials results in bifunctional materials[15] that have chemisorption potential for a wide range of light gases.[16–19] Post-synthetic functionalization uses silane chemistry to create covalent bonds between silica or metal oxides and functional organoalkoxysilanes.[20–23] Organoalkoxysilanes such as methacryloxypropyl-trimethoxysilane add functional groups to the scaffold that can interact with various toxic light gases to enhance the capacity of the composite for light gases.

In this study, a methacryloxypropyl-trimethoxysilane molecule (MAPS) is grafted onto a commercially available zirconium hydroxide scaffold to produce a composite material with high capacities for basic and acidic gases. The material is tested for capacity of ammonia, which is a basic gas, and sulfur dioxide, which is an acidic gas. Diffuse reflectance infrared fourier transform spectroscopy (DRIFTS) and nitrogen adsorption isotherms are used to characterize the composite material and compare it to the ungrafted zirconium hydroxide.

6.2 Experimental Methods

Materials

Zirconium hydroxide powder was purchased from Magnesium Electron, Inc. Nitrogen flushed methacryloxypropyl-trimethoxysilane (MAPS, 98 %) was purchased from Sigma-Aldrich. Dry ethanol (200-proof) was purchased from Pharmco-aaper.

For light gas analysis, cylinders of 1500 ppm_v ammonia in helium, 500 ppm_v of sulfur dioxide in air, ultra high purity helium, and zero air were purchased from A-L Compressed Gas.

Organoalkoxysilane grafting

The carbonyl functional group present in the methacryloxypropyl-trimethoxysilane molecules should enhance the ammonia capacity, and the base zirconium hydroxide scaffold has an inherent sulfur dioxide capacity.[11] The grafting was performed at a concentration of 4 moles of methacryloxypropyl-trimethoxysilane/kg zirconium hydroxide.

The grafting was performed under an inert environment in a 250 mL Schlenk flask. One half gram of $Zr(OH)_4$ and 125 mL of ethanol were added to the flask, which was then flushed with dry nitrogen for 15 minutes while stirring. A volume of 0.24 mL of methacryloxypropyl-trimethoxysilane was then added to the Schlenk flask to produce a material grafted with 4 moles organoalkoxysilane/kg adsorbent. The sample was stirred at room temperature overnight under an inert environment and then recovered via vacuum filtration. The filtered sample was washed with ethanol and water and degassed at 60 °C for 2 hours under vacuum.

Materials characterization

Textural characterization

Adsorption isotherms were measured using a Micromeritics ASAP 2020 at -196 °C with nitrogen as the analysis gas. Prior to measurement, approximately 0.1 g of each sample was degassed with heating to 50 °C and vacuum to 10 μbar. After reaching 10 μbar, the samples were heated to 70 °C under vacuum for an additional 6 hours.

Diffuse Reflectance Infrared Fourier Transform Spectroscopy (DRIFTS)

Reactions between the grafted $Zr(OH)_4$ and the analysis gas were monitored in real time using Fourier Transform Infrared Spectroscopy (FTIR) on a Nicolet 6700 FTIR from Thermo Fisher Scientific. The FTIR was equipped with a liquid nitrogen cooled mercury cadmium telluride detector that is available for scanning in the mid-IR range. The FTIR was also equipped with a Praying Mantis diffuse reflectance infrared fourier transform spectroscopy (DRIFTS) attachment and a Praying Mantis high tempera-

ture reaction chamber that fits inside the DRIFTS chamber. The powder sample is loaded into the sample cup, which has an internal diameter of 3.1 mm, in the center of the reaction chamber. The chamber is enclosed by two KBr windows to allow infrared light to reach the sample and one glass window for observation. An image of the reaction chamber inside the DRIFTS chamber on the Nicolet 6700 is shown in Figure 6.1.

During the analysis, premixed sulfur dioxide in helium at 500 ppm_v and 1500 ppm_v ammonia in helium were passed over the sample in the reaction chamber at a 10 sccm flow rate. The gas manifold is shown in Figure 6.2. A background scan was initially taken using the sample while purging with helium. The samples were then purged with helium and one baseline scan was taken. The scans were performed at 4 cm^{-1} resolution with 64 coadded scans. The helium flow was then stopped, the analysis gas started, and FTIR scans were taken of the sample every five minutes to monitor how the substrate changes with reaction. After the reaction was complete, the reaction chamber was purged with helium for one hour, with scans taken every 5 minutes to monitor the retention of ammonia or sulfur dioxide by the sample. FTIR band information was obtained from two sources.[24,25]

Light gas capacity

Equilibrium capacities for room temperature light gas adsorption of both ammonia and sulfur dioxide were measured for all samples using a breakthrough apparatus, a schematic of which is given in Furtado et al.[5,6] Prior to analysis, all samples were regenerated under vacuum at 60 °C for 2 hours.

To eliminate the possibility of side reactions with the carrier gas, ammonia breakthrough tests were conducted using 1500 ppm_v ammonia pre-mixed with dry helium, and pre-mixed sulfur dioxide in air was used for SO_2 breakthrough testing. The concentration of ammonia fed to the adsorbent bed was kept constant at 1133 mg/m^3. The concentration of sulfur dioxide in dry air was kept constant at 1428

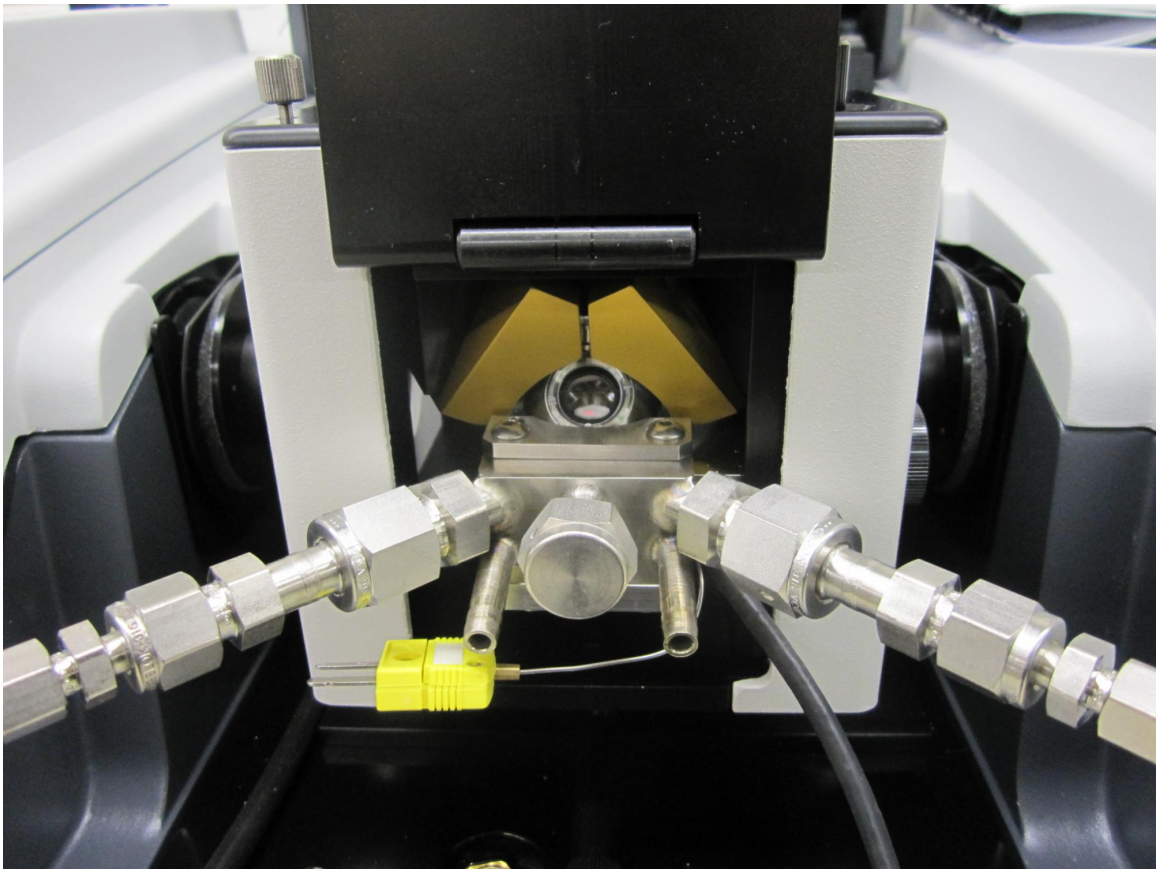

Figure 6.1 Powder reaction chamber located inside the DRIFTS-FTIR apparatus.

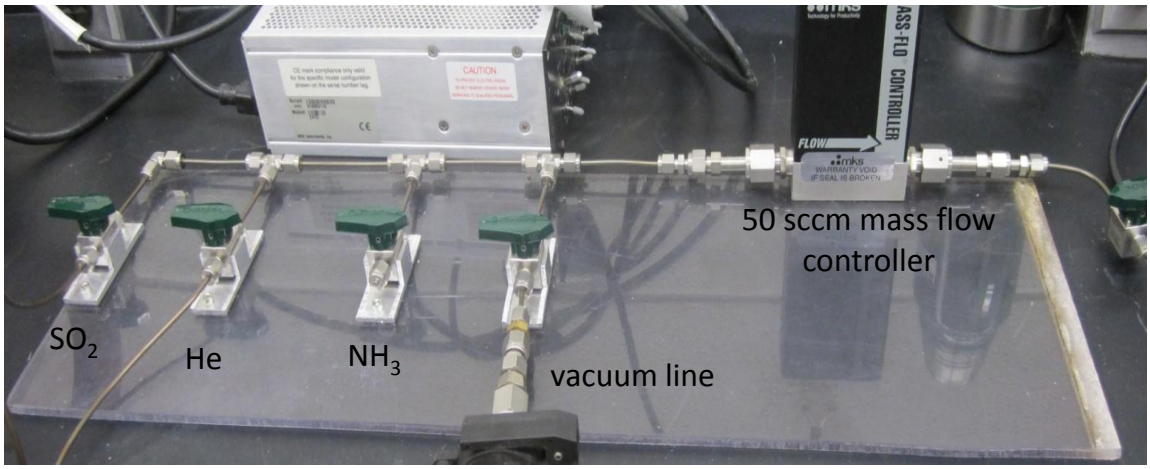

Figure 6.2 Gas manifold setup for the DRIFTS-FTIR apparatus.

Table 6.1: BET surface areas and pore volumes of grafted samples.

Sample	BET SA (m^2/g)	V_{pore} (cm^3/g)
$Zr(OH)_4$	395	0.38
MAPS-$Zr(OH)_4$	243	0.24

mg/m^3 (500 ppm_v). Before analysis, regenerated samples were equilibrated for 30 minutes in 10 sccm helium.

The capacity of the adsorbent materials was calculated according to the procedure described in previous publications.[5,6] The mass of the sample was approximately 4 mg and was contained in a small cylindrical adsorbent bed with an internal diameter of 4 mm. The capacities calculated using the breakthrough apparatus have a standard deviation on the order of 3%. The capacities of different batches of the grafted samples are expected to have larger standard deviations, on the order of 20 %, due to variations in the distribution of grafted molecules throughout the inorganic substrate.

6.3 Results

Material characterization

Nitrogen isotherms for the parent and grafted $Zr(OH)_4$ materials are shown in Figure 6.3. Surface areas and pore volumes for these materials are compared in Table 6.1. Organoalkoxysilane grafting results in a decrease in surface area compared to the parent material. The decrease in surface area corresponds to a decrease in pore volume when compared to the parent. This is consistent with grafting a large molecule within the pores of the zirconium hydroxide scaffold material.

Light gas adsorption

Ammonia and sulfur dioxide capacities for the $Zr(OH)_4$ and MAPS-$Zr(OH)_4$ materials are summarized in Table 6.2. The zirconium hydroxide substrate boasts a

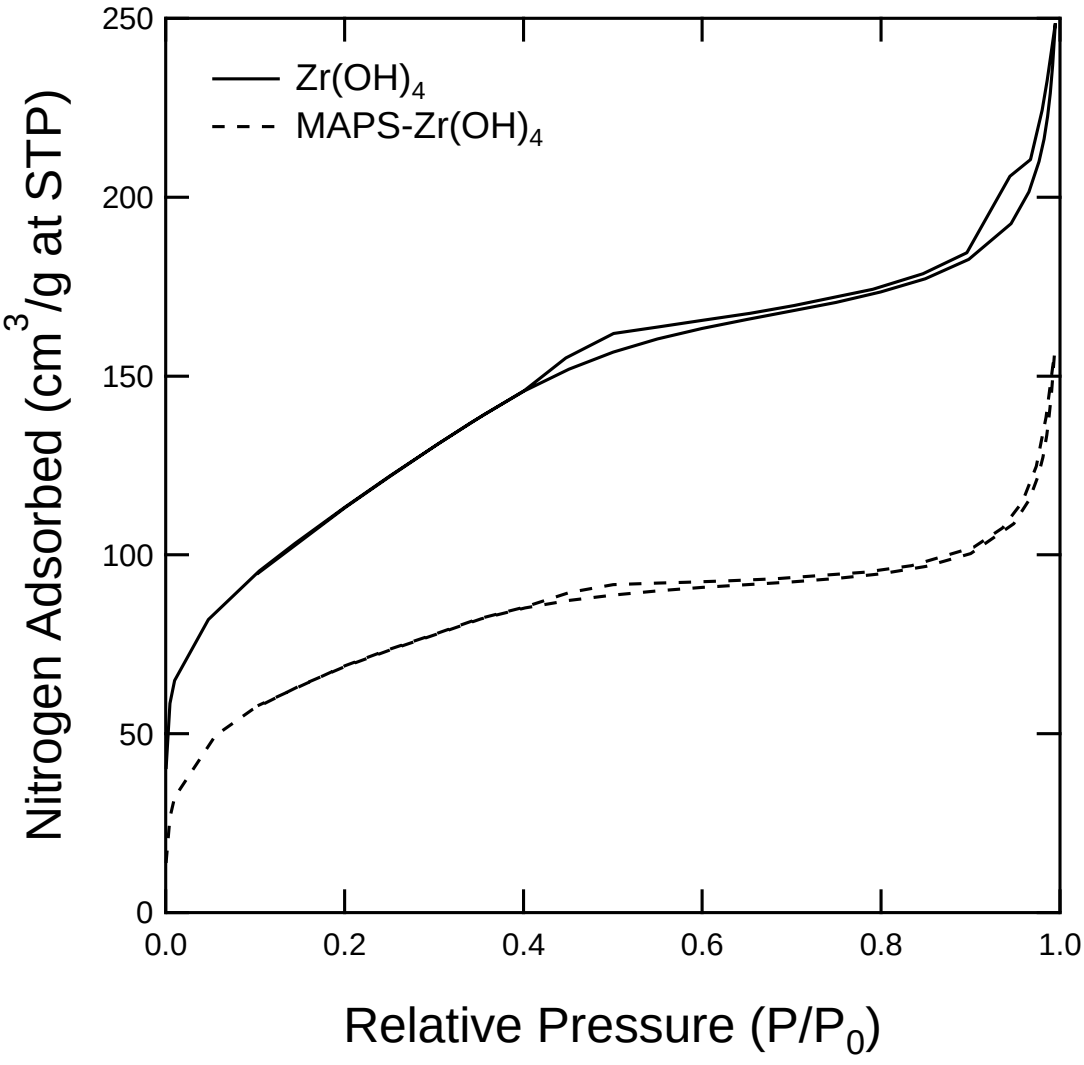

Figure 6.3 Nitrogen isotherms of $Zr(OH)_4$ and MAPS-$Zr(OH)_4$.

Table 6.2: Ammonia and sulfur dioxide capacities for the zirconium hydroxide samples.

Sample	NH_3 capacity (mol/kg sample)	SO_2 capacity (mol/kg sample)
$Zr(OH)_4$	1.45	1.30
MAPS-$Zr(OH)_4$	5.57	0.61

high initial sulfur dioxide capacity of 1.30 mol/kg. This is due to the basic terminal hydroxyl groups on the zirconium hydroxide, which interact with the sulfur dioxide and form sulfite species.[11] The chemisorption of SO_2 onto zirconium hydroxide allows for strong retention of the light gas after adsorption. As shown in the table, the parent material also has a high initial ammonia capacity; however, this is due to physical adsorption rather than chemisorption. The zirconium hydroxide initially has a high ammonia capacity, but since the ammonia molecules are not chemically bound to the substrate, regenerating using a vacuum for 30 minutes removes most of the ammonia, after which a similar high capacity can then be calculated from a second breakthrough test on the vacuumed sample.

It is evident from this table that the grafted MAPS molecule enhances the ammonia capacity by three-fold compared to the parent. This is most likely due to the carbonyl group providing hydrogen bonding sites for the ammonia. Unfortunately, the presence of the grafted molecule decreases the sulfur dioxide capacity compared to the parent material. Peterson et al.[11] postulate that the terminal hydroxyl groups on the parent zirconium hydroxide provide chemisorption sites for sulfur dixode. It is possible that grafting MAPS onto the parent material decreases the number of terminal hydroxyl groups available for reaction with sulfur dioxide, thereby resulting in a capacity decrease. Despite this decrease, this sulfur dioxide capacity is still very high compared to many commercial adsorbents.

DRIFTS

The parent zirconium hydroxide was exposed to sulfur dioxide to monitor the reaction between SO_2 and the substrate. The FTIR scans from this experiment are shown in Figure 6.4. One prominent band is apparent at 1124 cm^{-1} that increases over time during the sulfur dioxide purge. This band is representative of symmetric SO_2 stretching. Based on the position of this peak, it is evident that the sulfur dioxide remains intact when adsorbed on the zirconium hydroxide substrate. Peterson et al.[11,26] performed X-ray photoelectron spectroscopy on the parent and identified the presence of sulfite (SO_3^-) species. A sulfite asymmetric stretching band would be seen in the 1200-1195 cm^{-1} region. This band is not present in the FTIR data, possibly due to the difference in experimental conditions between the two analyses. In their analysis, XPS was used to analyze a sample after the chemisorption of sulfur dioxide had been completed, whereas the present case analyzes the zirconium hydroxide substrate during the reaction. It is possible that it takes time for the sulfur dioxide to react to form the sulfite, and this was not apparent from the FTIR results. It is obvious that relatively strong bonds are being formed between the sulfur dioxide and zirconium hydroxide, since the peak at 1124 cm^{-1} representing intact SO_2 stretching remains prominent during the 1 hour helium purge after the experiment.

There is also a decrease in O-H absorbance intensity compared to the base material, as shown by the peaks at 3702 and 3612 cm^{-1}. This decrease in absorbance compared to the baseline is indicative of sulfur dioxide interacting with the hydroxyl groups on the zirconium hydroxide substrate. This decrease in intensity remains during the 1 hour helium purge; consequently, the sulfur dioxide forms chemical bonds with the hydroxyl groups that are strong enough to remain during the helium purge.

Figure 6.5 plots IR spectra of the parent material exposed to ammonia in a DRIFTS experiment designed to monitor the reaction between ammonia and the

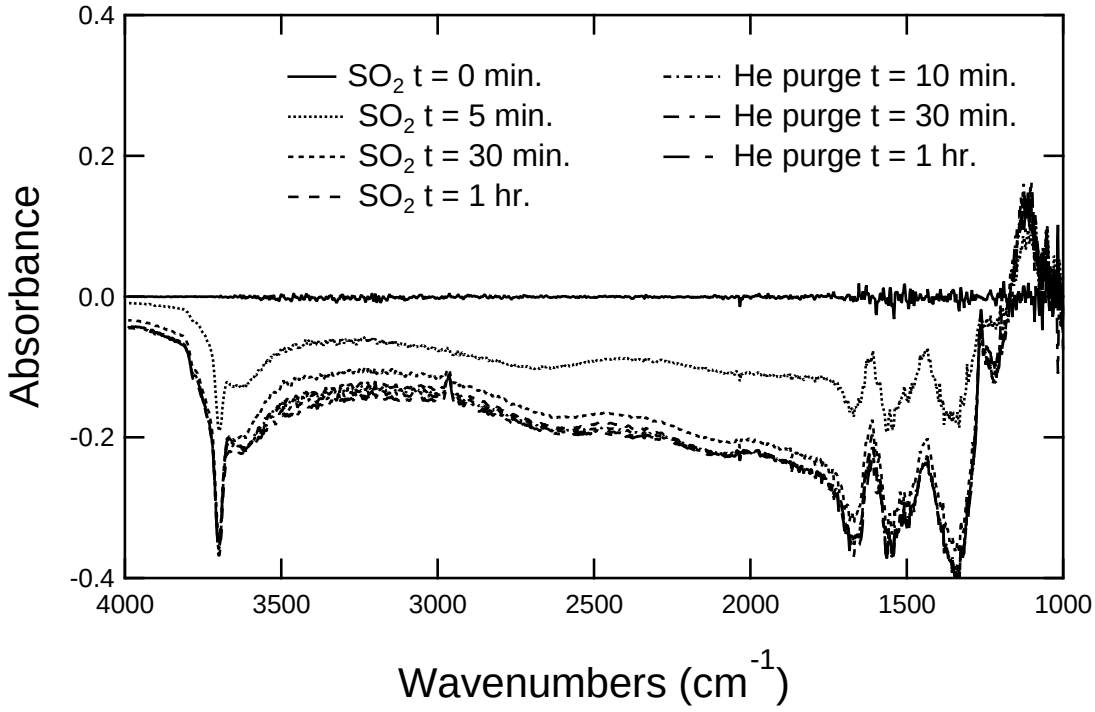

Figure 6.4 DRIFTS experiment: SO_2 on $Zr(OH)_4$.

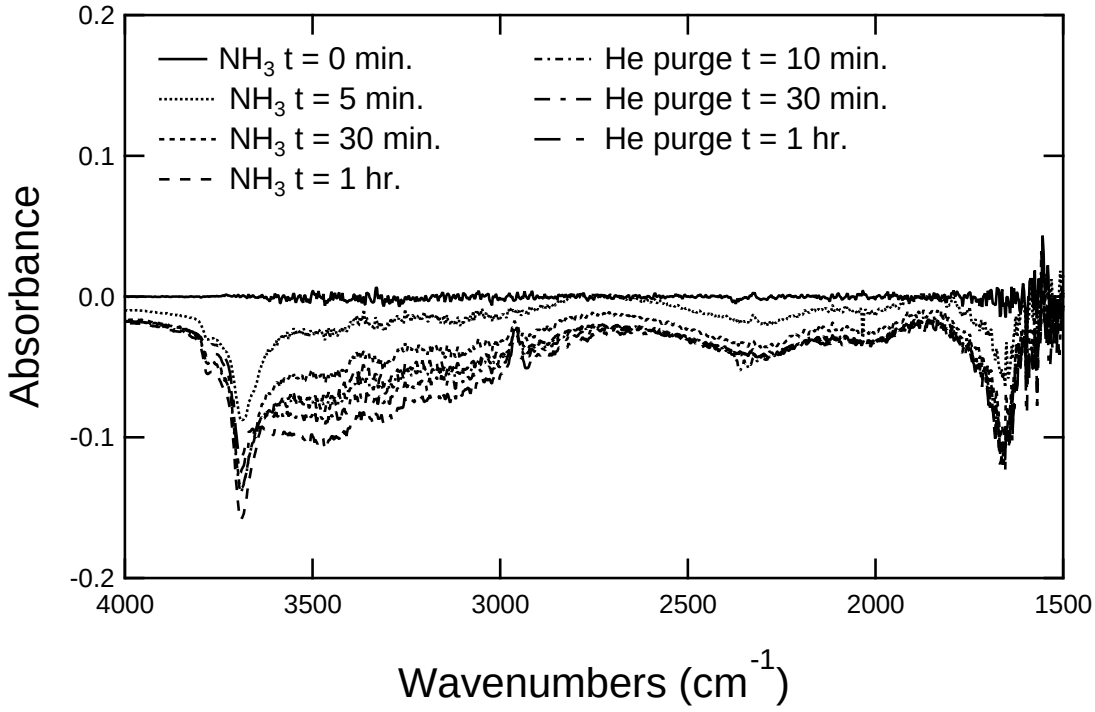

Figure 6.5 DRIFTS experiment: NH_3 on $Zr(OH)_4$.

substrate with respect to time. There are several prominent bands that change with time during the course of the experiment, one at 3693 cm^{-1} and one at 1656 cm^{-1}. The band at 1656 cm^{-1} represents an adsorbed water peak. The decrease in absorbance at this intensity shows that the adsorbed water is removed from the substrate during the ammonia purge. The decreased absorbance at 1656 cm^{-1} remains after purging with helium because the adsorbed water is flushed from the system during the ammonia and helium purges and is not available to readsorb on the substrate. The band at 3693 cm^{-1} corresponds to the O-H stretching of hydroxyl groups on the zirconium hydroxide substrate. The absorbance decrease at 3693 cm^{-1} shows that the ammonia molecules are associating with the hydroxyl groups on the zirconium hydroxide. After stopping the flow of ammonia and beginning the helium purge, the peak at 3693 cm^{-1} reverts closer to the baseline absorbance. Thus, the ammonia is not strongly bound to the hydroxyl groups on the zirconium hydroxide.

Grafting MAPS onto the zirconium hydroxide substrate complicates the FTIR analysis. Figure 6.6 compares the spectra of grafted and ungrafted zirconium hydroxide. The bands between 3000 and 2800 cm^{-1} represent aliphatic C-H stretching due to the grafted MAPS molecule. The MAPS molecule also results in an increase in the number of bands between 1780 and 1200 cm^{-1}, which are generally due to the interactions between oxygen and carbon in the methacrylate portion of the MAPS molecule.

Figure 6.7 shows results of the DRIFTS experiment using ammonia on MAPS-$Zr(OH)_4$. Similar to the ungrafted zirconium hydroxide, this experiment shows a decrease in absorbance at 3693 cm^{-1} in the O-H stretching region. This absorbance decrease reverts closer to the baseline during the helium purge; thus, the grafted MAPS molecule assists with hydrogen bonding of ammonia on the sample in the same way that the hydroxyl groups on the zirconium hydroxide substrate provide ammonia capacity. Consequently, ammonia is able to hydrogen bond with both the

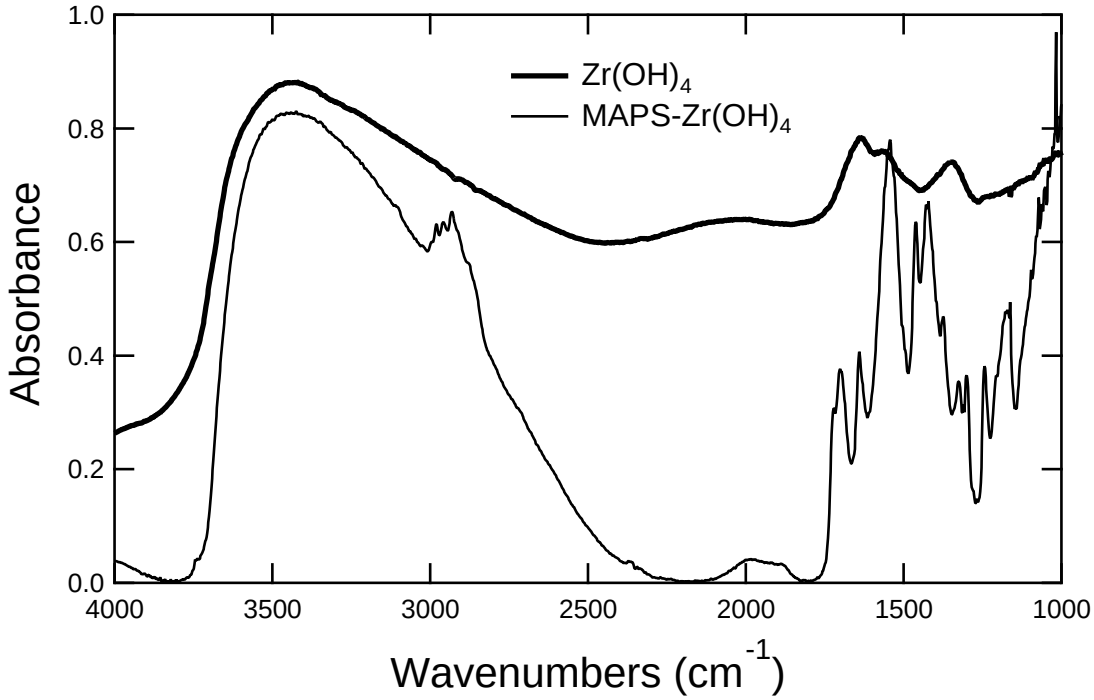

Figure 6.6 Comparison of DRIFTS spectra for MAPS-$Zr(OH)_4$ and $Zr(OH)_4$.

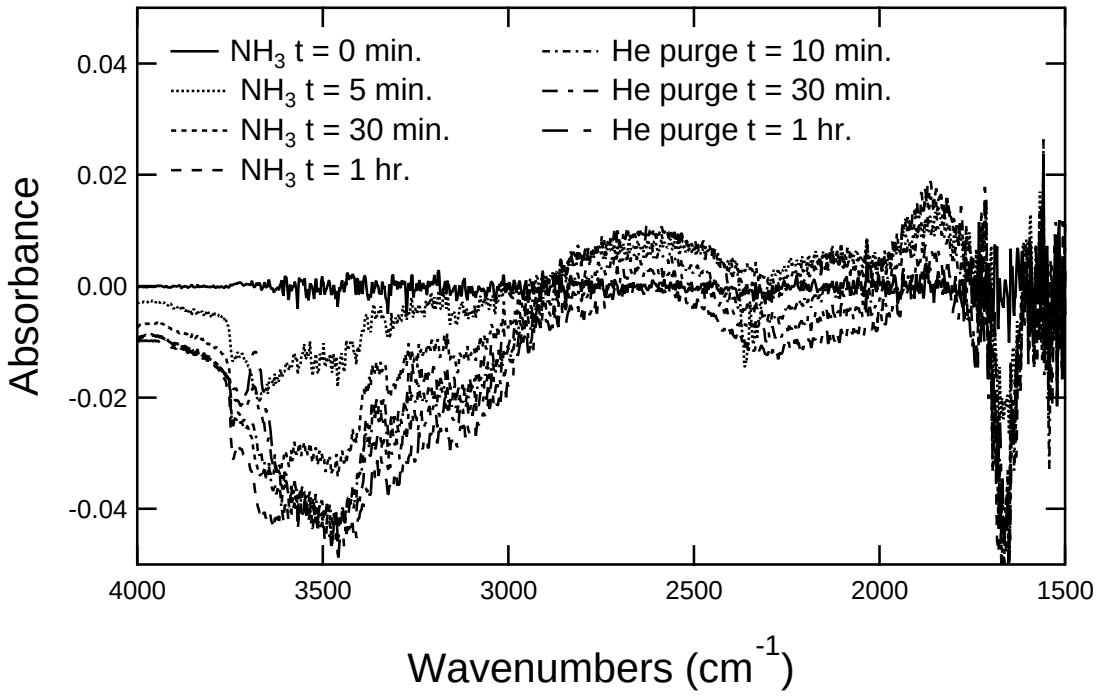

Figure 6.7 DRIFTS experiment: NH_3 on MAPS-$Zr(OH)_4$.

hydroxyl groups and the carbonyls on the MAPS-$Zr(OH)_4$ material. The additional carbonyl groups added due to the grafting of MAPS results in the increase in ammonia capacity associated with the MAPS-$Zr(OH)_4$ compared to the parent. The band at 1656 cm^{-1} represents the adsorbed water peak. Similar to the ungrafted substrate, the grafted sample shows a decrease in adsorbed water during the ammonia and helium purges. Thus, water molecules are liberated from the MAPS-$Zr(OH)_4$ sample during the experiment.

Figure 6.8 shows MAPS-$Zr(OH)_4$ exposed to sulfur dioxide. Similar to the parent material, there is an absorbance decrease in the 3670 cm^{-1} region. This band corresponds to a decrease in the hydroxyl group stretching during the sulfur dioxide purge. Similar to the ungrafted zirconium hydroxide substrate, the sulfur dioxide molecules are strongly bound to the composite since the absorbance decrease remains prominent when purging with helium for one hour after exposure to sulfur dioxide.

6.4 Conclusions

A substrate with an established high chemisorption capacity for sulfur dioxide was grafted with methacryloxypropyl-trimethoxysilane to enhance the ammonia capacity of the composite material. This composite was found to have a decreased sulfur dioxide capacity compared to the ungrafted parent material. However, the grafting does greatly boost the ammonia capacity. Grafting the molecule onto the zirconium hydroxide resulted in a slight decrease in surface area and pore volume compared to the parent material.

Diffuse reflectance infrared fourier transform spectroscopy was used in conjunction with a gas reaction chamber to monitor changes in the composite with time while the sample was exposed to ammonia and sulfur dioxide. This type of analysis was found to be useful in identifying the compounds that are formed throughout the course of a chemisorption reaction. Based on the FTIR analyses, ammonia was found

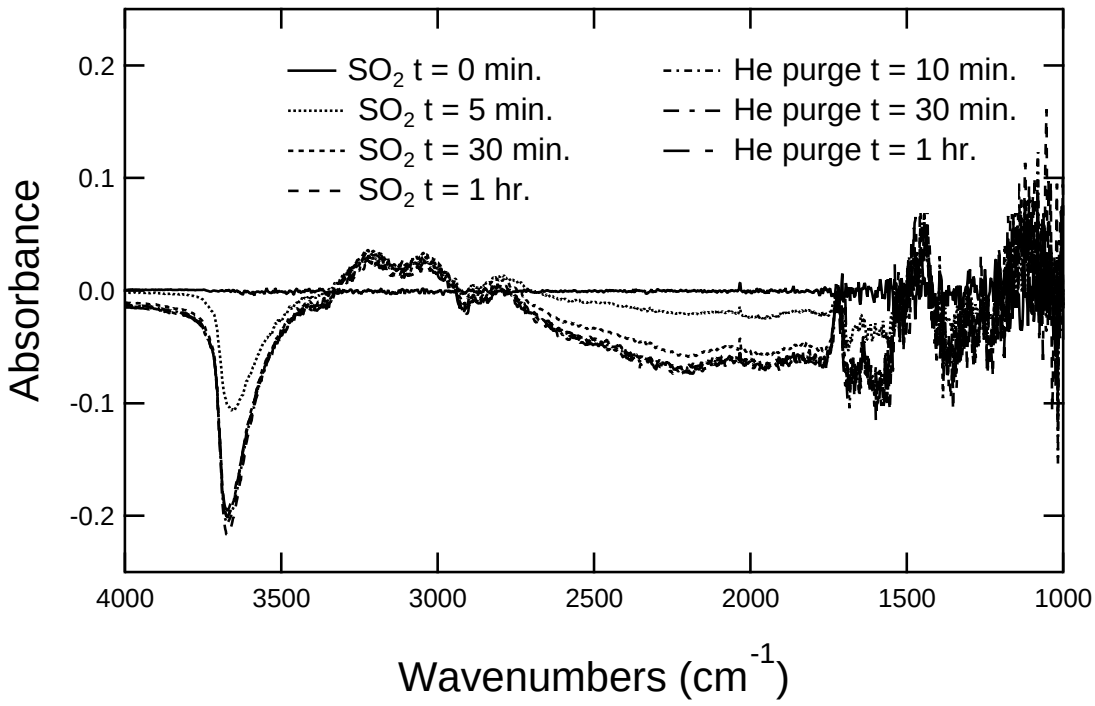

Figure 6.8 DRIFTS experiment: SO_2 on MAPS-$Zr(OH)_4$.

to interact with the hydroxyl groups on the zirconium hydroxide and the carbonyl groups on the grafted MAPS molecule through hydrogen bonding. In both samples, some ammonia molecules were removed during the helium purge. The sulfur dioxide molecules remain intact during chemisorption with the material and do not react quickly to form sulfite species. The bonds between the grafted and ungrafted zirconium hydroxide materials and sulfur dioxide are strong enough to remain intact during a helium purge. Consequently, the sulfur dioxide molecules are strongly bound to the materials.

References

[1] C.T. Kresge, M.E. Leonowicz, W.J. Roth, J.C. Vartuli, J.S. Beck. Ordered mesoporous molecular sieves synthesized by a liquid crystal template mechanism. *Nature*, 1992, **359**, 710-712.

[2] M. Shengqian, L. Meng. Energy-related applications of functional porous metal-organic frameworks. *Pure Appl. Chem.*, 2011, **83**, 167-188.

[3] G. W. Peterson, G. W. Wagner, J. H. Keller, J. A. Rossin. Enhanced cyanogen chloride removal by the reactive zirconium hydroxide substrate *Ind. Eng. Chem. Res.*, 2010, **49**, 11182-11187.

[4] K. Tanabe, T. Yamaguchi. Acid-base bifunctional catalysis by ZrO2 and its mixed oxides. *Catal. Today*, 1994, **20**, 185-198.

[5] A. M. B. Furtado, Y. Wang, T. G. Glover, M. D. LeVan. MCM-41 impregnated with active metal sites: synthesis, characterization, and ammonia adsorption. *Microporous Mesoporous Mater.*, 2011, **142**, 730-739.

[6] A. M. B. Furtado, J. Liu, Y. Wang, M. D. LeVan. Mesoporous silica-metal organic composite: synthesis, characterization, and ammonia adsorption. *J. Mater. Chem.*, 2011, **21**, 6698-6706.

[7] J. Zhang, Z. Maa, J. Jiao, H. Yin, W. Yan, E. W. Hagaman, J. Yu, S. Dai. Surface functionalization of mesoporous silica SBA-15 by liquid-phase grafting of zirconium phosphate. *Microporous Mesoporous Mater.*, 2010, **129**, 200-209.

[8] G. L. Drisko, A. Zelcer, V. Luca, R. A. Caruso, G. J. de A. A. Soler-Illia. One-pot synthesis of hierarchically structured ceramic monoliths with adjustable porosity. *Chem. Mater.*, 2010, **22**, 4379-4385.

[9] A. V. Ivanov, S. V. Lysenko, S. V. Baranova, A. V. Sungurov, T. N. Zangelov, E. A. Karakhanov. Thermally stable materials based on mesostructured sulfated zirconia. *Microporour Mesoporous Mater.*, 2006, **91**, 254-260.

[10] J. M. Kim, C. H. Shin, R. Ryoo. Mesoporous molecular sieve with binary transition metal (Zr-Cr) oxide framework. *Catal. Today*, 1997, **38r**, 221-226.

[11] G. W. Peterson, C. J. Karwacki, W. B. Feaver, J. A. Rossin. Zirconium hydroxide as a reactive substrate for the removal of sulfur dioxide. *Ind. Eng. Chem. Res.*, 2009, **48**, 1694-1698

[12] G. B. Han, N. Park, S. H. Yoon, T. J. Lee. Investigation of catalytic reduction of sulfur dioxide with carbon monoxide over zirconium dioxide catalyst for selective sulfur recovery. *Ind. Eng. Chem. Res.*, 2008, **47**, 1427-1434.

[13] S. N. R. Rao, E. Waddell, M. B. Mitchell, M. G. White. Selective sulfur dioxide adsorbents prepared from designed dispersions of groups IA and IIA metal oxides on alumina. *J. Catal.*, 1996, **163**, 176-185.

[14] A. R. Ramadan, N. Yacoub, S. Bahgat, J. Ragai. Surface and acidic properties of mixed titanium and zirconium sulfated oxides. *Colloids Surf., A: Physicochem. Eng. Aspects*, 2007, **302**, 36-43.

[15] F. Shang, H. Liu, J. Sun, B. Liu, C. Wang, J. Guan, Q. Kan. Synthesis, characterization and catalytic application of bifunctional catalyst: Al-MCM-41-NH(2). *Catal. Commun.*, 2011, **12**, 739-743.

[16] B. Aziz, G. Zhao, N. Hedin. Carbon dioxide sorbents with propylamine groups-silica functionalized with a fractional factorial design approach. *Langmuir*, 2011, **27**, 3822-3834.

[17] T. Yokoi, H. Yoshitake, T. Tatsumi. Synthesis of amino-functionalized MCM-41 via direct co-condensation and post-synthesis grafting methods using mono-, di- and tri-amino-organoalkoxysilanes. *J. Mater. Chem.*, 2004, **14**, 951-957.

[18] X. Wang, K. S. K. Lin, J. C. C. Chan, S. Cheng. Direct synthesis and catalytic applications of ordered large pore aminopropyl-functionalized SBA-15 mesoporous materials. *J. Phys. Chem. B*, 2005, **109**, 1763-1769.

[19] D. Bruhwiler. Postsynthetic functionalization of mesoporous silica. *Nanoscale*, 2010, **2**, 887-892.

[20] S. Yoo, J. D. Lunn, S. Gonzalez, J. A. Ristich, E. E. Simanek, D. F. Shantz. Engineering nanospaces: OMS/dendrimer hybrids possessing controllable chemistry and porosity. *Chem. Mater.*, 2006, **18**, 2935-2942.

[21] E. J. Acosta, C. S. Carr, E. E. Simanek, D. F. Shantz. Engineering nanospaces: Iterative synthesis of melamine-based dendrimers on amine-functionalized SBA-15 leading to complex hybrids with controllable chemistry and porosity. *Adv. Mater.*, 2004, **16**, 985-989.

[22] I. Shimizu, A. Yoshino, H. Okabayashi, E. Nishio, C. O'Connor. Kinetics of interaction of 3-amimopropyltriethoxysilane on a silica gel surface using elemental analysis and diffuse reflectance infrared Fourier transform spectra. *J. Chem. Soc., Faraday Trans.*, 1997, **93**, 1971-1979.

[23] T. Borrego, M. Andrade, M. L. Pinto, A. R. Silva, A. P. Carvalho, J. Rocha, C. Freire, J. Pires. Physicochemical characterization of silylated functionalized materials. *J. Colloid Interface Sci.*, 2010, **344**, 603-610.

[24] K. Nakanishi, P. H. Solomon, Infrared absorption spectroscopy: Second edition, Holden-Day, Inc., San Francisco, 1977.

[25] K. Nishikida, E. Nishio, R. W. Hannah, Selected applications of modern FT-IR techniques, Gordon and Breach Publishers, Australia, 1995.

[26] G. W. Peterson, J. A. Rossin, C. J. Karwacki, T. G. Glover. Surface chemistry and morphology of zirconia polymorphs and the influence on sulfur dioxide removal. *J. Phys. Chem. C*, 2011, **115**, 9644-9650.

CHAPTER VII

CONCLUSIONS AND RECOMMENDATIONS

The work presented in this dissertation focuses on engineering adsorbent materials to remove light gases from air. Various composite materials have been designed and tested for their ammonia and sulfur dioxide removal capacities under dry and humid conditions. Most composites include a hexagonal siliceous support that has a high initial ammonia capacity. The second phase in the composite ranges from carbonaceous sucrose to grafted organoalkoxysilane molecules that contain functional groups for chemisorption with light gases.

The principal findings of this research are:

Metal salt impregnations into MCM-41

- Metal salts including the nitrates, sulfates, chlorides, and carbonates of iron, copper, and zinc were impregnated into MCM-41 via aqueous impregnations. These aqueous impregnations were found to enhance the ammonia capacity compared to the siliceous material. Statistical analysis was used to produce predictive equations relating the metal salt impregnations with corresponding ammonia capacities. The metal type and anion type were found to be the most statistically significant predictors of ammonia capacity for the impregnated samples. The intrinsic metal salt pH and metal oxidation state were determined not to be statistically significant ammonia capacity predictors.

- Impregnation with zinc chloride resulted in the highest ammonia capacity, and amounts between 20 and 50 wt % $ZnCl_2$ impregnation yield the highest ammonia capacities, ranging from 7.0 - 8.9 mol/kg loading. After 50 wt % $ZnCl_2$ loading, the ammonia capacity decreases because the metal salt is present at too high a

concentration to be well dispersed throughout the MCM-41 matrix.

- Insoluble metal salts, specifically the metal carbonates, were found to have lower ammonia capacities at both conditioning temperatures due to the aqueous impregnation method used.

- The conditioning temperature was found to play a large role in the metal salt activity after impregnation. A high temperature conditioning step resulted in the formation of Zn and ZnO from decomposition of $ZnSO_4$. A corresponding decrease in ammonia capacity was observed for the high temperature sample compared to those conditioned at lower temperatures.

MSMO composite

- A composite material was synthesized by combining an ordered mesoporous silica phase, specifically MCM-41 impregnated with copper and benzene-1,3,5-tricarboxylic acid, the organic BTC linker used in the synthesis of a common MOF, to give an ordered mesoporous silica - metal organic (MSMO) composite material. The nitrogen isotherm confirms the formation of the mesoporous composite material. According to TGA results, approximately 12 % organic BTC is loaded onto the MCM-41 and bound to the copper sites dispersed throughout MCM-41. X-ray diffraction results confirm that the composite does not lose its long range MCM-41 order after impregnation with the BTC. It also confirms that small amounts of CuBTC crystals (about 3 wt %) are present in the final sample as an impurity. XPS shows that copper sites that are distributed throughout the MCM-41 matrix are actively bound to BTC.

- The presence of both copper sites and intact BTC results in an ammonia capacity that is higher than the base ordered mesoporous silica (5.2 mol/kg compared to 2.0 mol/kg) due to the functionality provided by the metal organic phase.

The composite has four types of active sites available for ammonia adsorption. These are: (1) the base silica phase provides inherent ammonia capacity, (2) the addition of hydroxyl groups to the MCM-41 during hydrothermal conditioning enhance ammonia capacity, (3) the copper sites distributed throughout the silica matrix increase NH_3 capacity, and (4) carboxylic acid groups from the BTC linker provide coordination sites for ammonia.

- After hydrothermal conditioning, the novel composite material maintains its high ammonia capacity, whereas the corresponding metal organic framework sample degrades, resulting in a large decrease in ammonia capacity. XPS and XRD show that the BTC present in the composite material remains intact and that the MCM-41 structure is maintained after conditioning.

Carbon silica composites for SO_2 and NH_3 adsorption

- A series of carbon silica composites with MCM-41 as the silica phase and carbonized furfuryl alcohol or sucrose as the carbon phase have been synthesized using different carbonization temperatures. The parent silica phase has a large capacity for ammonia and minimal affinity for the acidic gas sulfur dioxide. Impregnation of MCM-41 with furfuryl alcohol to form the CSC maintains the ammonia capacity and enhances the sulfur dioxide capacity of the adsorbent. MCM-41 impregnation with carbonized sucrose results in an increase in both the sulfur dioxide and ammonia capacities compared to the unimpregnated MCM-41.

- The CSC-FA carbonized at 600 °C has the highest surface area, followed by the samples carbonized at 500 and 300 °C. Carbonization of the furfuryl alcohol polymer is a rate process, consequently the sample heated to 300 °C is not fully carbonized, and the sample carbonized at 600 °C has the most well-developed pore structure.

- A low temperature procedure has been developed to impregnate MCM-41 with sucrose. The low temperature carbonization procedure uses equal parts ethanol and water in a high pressure vessel to produce a carbonized CSC material at 200 °C. The amount of carbon loaded into the MCM-41 was found to scale with the reaction time. Nitrogen isotherms show that the carbon phase is microporous.

- Metal sites have been successfully incorporated into the CSC adsorbents. The metal site impregnations in both phases of CSC-FA do not enhance the ammonia or sulfur dioxide capacities compared to the parent CSC-FA material. Similarly, the metal sites impregnated into the carbon phase of the CSC-sucrose do not enhance the sulfur dioxide capacities compared to the parent. It is possible that the metal salt impregnates block the pores of the carbon phases, as evidenced by the decrease in surface area for all metal impregnated samples. Since both furfuryl alcohol and sucrose must be carbonized at elevated temperatures, it is also possible that the active metal sites decompose via oxide formation during the carbonization process and are unavailable for chemisorption in the final product.

- Despite the lack of capacity enhancement provided by the metal salt impregnations, the presence of the carbon phases in the carbon silica composites successfully enhances the toxic light gas capacity compared to the parent silica phase. Metal impregnation into CSC materials composed of a carbon phase developed with a much lower temperature requirement could enhance the activity of the active metal sites by minimizing decomposition during synthesis.

Bifunctional organoalkoxysilane-grafted silica composites for SO_2 and NH_3 adsorption

- Composite materials have been synthesized using silane chemistry to graft organoalkoxysilanes with unique functional groups onto MCM-41. By exploit-

ing the chemistry of the functional groups, the biphasic materials exhibit high single pass capacities for sulfur dioxide, an acidic gas, and ammonia, a basic gas. Organoalkoxysilane molecules containing carbonyl groups provide additional ammonia capacity, and molecules containing amine groups provide sulfur dioxide capacity.

- The arrangement of functional groups on the organoalkoxysilanes result in different ammonia and sulfur dioxide capacities for the grafted samples. A shielding effect appears to occur when both carbonyl and amine functional groups are present on the same grafted molecule. The amine functional group enhances the sulfur dioxide capacity by forming charge-transfer complexes with SO_2. The carbonyl groups enhance the capacity for ammonia by hydrogen bonding.

- Grafting two molecule types onto MCM-41 is one way to tailor the adsorbent for the removal of both gases. APTES-isocyanate-MCM-41 has a high sulfur dioxide capacity, which is comparable to that of APTES-MCM-41. Although not as high as isocyanate-MCM-41, the ammonia capacity of this sample is still very high. Grafting different amounts of molecules containing single functional groups onto MCM-41 provides the ability to tailor the resulting acidic and basic gas capacity for this bifunctional adsorbent material.

Bifunctional organoalkoxysilane-grafted zirconium hydroxide composite for SO_2 and NH_3 adsorption

- A $Zr(OH)_4$ substrate with an established high chemisorption capacity for sulfur dioxide was grafted with an organoalkoxysilane molecule containing a carbonyl group (methacryloxypropyl-trimethoxysilane) to enhance the ammonia capacity of the composite material. This composite was found to have a lower sulfur dioxide capacity compared to the ungrafted parent material. However, the grafting greatly boosts the ammonia capacity compared to the ungrafted parent.

- A novel technique using diffuse reflectance infrared fourier transform spectroscopy in conjunction with a gas reaction chamber was used to monitor changes in the composite with time while the sample was exposed to ammonia and sulfur dioxide. This robust analytical technique was found to be useful in identifying the chemical bonding throughout the course of a chemisorption reaction.

- Based on the FTIR analyses, ammonia was found to interact via hydrogen bonding with the hydroxyl groups on the zirconium hydroxide and the carbonyl groups on the grafted organoalkoxysilane molecule. The sulfur dioxide molecules remain intact during chemisorption with the material and do not react quickly to form sulfite species.

- The bonds between the grafted and ungrafted zirconium hydroxide materials and sulfur dioxide are strong enough to remain intact during a helium purge through the FTIR reaction chamber. Consequently, sulfur dioxide is strongly adsorbed to the materials.

There are opportunities for portions of this work to be extended. My recommendations for future work include the following:

- Applications of the DRIFTS technique in conjunction with the powder reaction chamber can be applied to the MSMO material. This technique could be used to better monitor the changes in bonding while flowing humid air across the MSMO material.

- Formation of carbon silica composites using a carbon phase developed with a much lower reaction temperature could maintain the activity of the impregnated metal salts for ammonia and sulfur dioxide. Consequently, other carbon phases should be investigated to identify a phase that fits the low carbonization temperature requirements.

- Amine functional groups on organoalkoxysilane molecules were found to chemisorb sulfur dioxide. The carbonyl groups on the organoalkoxysilane molecules have been found to promote hydrogen bonding of large amounts of ammonia on the substrate. The strength of hydrogen bonding does not compare to the chemisorption strength of sulfur dioxide on amines. Consequently, organoalkoxysilane molecules containing other functional groups should be investigated to enhance the ammonia retention on $Zr(OH)_4$ and MCM-41 grafted composites.